Département de Chimie
Faculté des Sciences
Université Libre de Bruxelles

Natural and model membranes: structure and interaction with bio-active molecules via neutron reflection

Alexis de Ghellinck

Thèse présentée en vue de l'obtention du grade de
Docteur en Sciences
Décembre 2013

À la mémoire de Chantal, ma marraine

Remerciements

Je voudrais remercier le professeur Michele Sferrazza pour m'avoir accueilli au sein du Laboratoire de Physique Expérimentale des Interfaces et pour m'avoir donné la possibilité de faire une thèse à l'Institut Laue-Langevin à Grenoble ainsi que le professeur Claudine Buess-Hermann pour avoir été mon co-superviseur.

Je souhaiterais également chaleureusement remercier Giovanna Fragneto pour avoir été mon superviseur à l'Institut Laue-Langevin. Ses connaissances scientifiques, son enthousiasme, sa sympathie et sa disponibilité ont fait que cette thèse a été une expérience extrêmement positive et inoubliable.

I would like to thank Hanna Wacklin for her support, help and advices on the "yeast project" throughout these whole three years.

J'aimerais aussi remercier Juliette Jouhet, Éric Maréchal et Maryse Block pour leur aide indispensable sur l'extraction et l'analyse des lipides. Je remercie aussi Laurence, Céline, Melissa ainsi que les autres membres du service pour avoir contribué à cette chouette ambiance au laboratoire.

I wish to thank Beate Kloesgen and Shen Chen for their fruitful collaboration on the resveratrol project and their help during the corresponding experiments.

I also would like to thank Laura Cantù and Sandro Sonnino for inviting me at the Università di Milano for five weeks. Many thanks too to Valeria, Elenia, Simona and Ricardo.

I also thank all the colleagues at the ILL, those already gone as well as those still there. You contributed to make these three years wonderful. Among PhD students and post-docs: Colin, Ida, Martin, Irene, Francesco, Federica, Christine, Ramona, Ingo, Eva, Pierre, Diane, Giacomo, Ernesto, Johnny, Andrew, Peggy, Charlotte, Eron, Anton, Markus and many others. A special thank to the two post-docs in my office, Manu and Yuri, for the interesting scientific and not-that-scientific discussions and for bringing such a good atmosphere in and outside the office. I also thank all the scientists and technicians I met during these three years. Je voudrais aussi

remercier toutes les personnes que j'ai rencontrées à Grenoble en dehors de l'ILL : Bjorn, Dominik, Cécile, Bogdan, Peppe e Laura, Davide e Sheeba, Cédric et Clair, Daniel et Rebecca, Gaëtan et bien d'autres...

Je souhaite aussi remercier toute ma famille pour leur soutien et leur présence inconditionnels. Finalement, merci aussi Louloute pour avoir partagé ces trois années avec moi, ton soutien a été indispensable dans la réalisation de cette thèse.

Summary

In this thesis, the structure of natural and model membranes and their interactions with bio-active molecules were investigated by means of neutron reflectometry.

Natural lipids were extracted from the yeast *Pichia pastoris* grown in hydrogenated and deuterated media. The analysis showed that the relative amounts of the main phospholipids do not change when yeast cells are grown in deuterated medium. However, deuterated yeast cells contain mainly C18:1 fatty acid while the unsaturation degree is higher in hydrogenated yeast. Lowering the growth temperature allows increasing the content of polyunsaturated fatty acid of deuterated yeast. A qualitative analysis of ceramide and sphingolipids was performed and a protocol for the separation of phosphatidylcholine and phosphatidylethanolamine fractions was established.

The lipids extracted from the hydrogenated and deuterated yeasts were used to form supported planar bilayer on silicon substrates. The structure of reconstituted yeast lipid bilayers was investigated by neutron reflectometry. The bilayer composed of deuterated polar lipids has a thickness similar to bilayers made of synthetic C18:1 phosphocholines. In presence of sterols, the roughness values at both tail and headgroup interfaces increase. The bilayer composed of hydrogenated polar lipids is much thinner than the deuterated one. This can be explained by the presence of polyunsaturated fatty acids which tends to make the membrane thinner. In presence of sterols, the thickness of the hydrogenated bilayer increases.

The interaction of these bilayers with the antifungal drug amphotericin B (AmB) was investigated. AmB is known to interact strongly with ergosterol-containing membranes and less strongly with cholesterol-containing membranes. AmB formed a diluted layer on the top of all the investigated lipid bilayers which could not be rinsed away. When sterols were present in the deuterated bilayer, the scattering length density of the tail region was lowered, indicating that AmB inserted in the membrane. When sterols were

present in the hydrogenated bilayer, the main effect was the decrease of the overall bilayer thickness which is also consistent with its insertion.

The structure of plant lipid bilayers and their interactions with synthetic intermediates was also investigated by means on neutron reflection. Ternary mixtures of plant lipids were deposited on silicon substrates and quaternary mixtures were deposited on sapphire. The ternary mixture lipid bilayer has a thickness of 38 $\pm$ 1 Å, which is in agreement with values found in literature. The thickness of the bilayer made of the quaternary mixture is 28 Å. This low thickness compared to values found in literature could be due to a substrate effect. When diacylglycerol (DAG) is present in the bilayers, the surface pressure - area profile shows that it increases the mean molecular area at a surface pressure of 37 mN/m. Moreover, the presence of DAG makes the water layer, located between the lipid bilayer and the substrate, thicker in the case of the ternary mixture and thinner in the case of the quaternary mixture. This is due to electrostatic interactions between the negatively charged lipids and the positively charged sapphire substrate and negatively charged silicon substrate. The interaction of phosphatidic acid (PA) with plant bilayers was also investigated with the aim to detect a possible flip-flop of this molecule. However, the presence of PA made the supported bilayers unstable over time and no flip-flop was detected.

In the last chapter, the location of a small molecule, resveratrol, in model bilayers composed of synthetic C16:0 phosphocholines was studied by neutron reflectivity. When resveratrol is adsorbed from the subphase, the outer headgroup thickness values increase. This increase is due to a reorganization of the headgroup dipole upon the incubation of resveratrol in the bilayer. When resveratrol is incorporated in the lipid solution before the bilayer deposition, the lipid bilayer is symmetrical and the roughness at headgroup - tail interface is increased. These findings suggest that resveratrol is located at the boundary between the hydrophobic and hydrophilic parts of the membrane.

Contents

Chapter 1

Introduction

1.1 Cell membranes

The first function of biological membranes is to define space in different compartments in the cells of living organisms. Each living cell is delimited by the plasma membrane acting as a barrier and controlling the interaction between the cell and its surrounding medium. This statement is true for every cell, from the primitive prokaryotes which do not contain a nucleus to larger eukaryotes which include animal, plant and fungal cells.

The plasma membrane does not only have a protective function against the environment. Some membrane proteins also provide an anchor for the extracellular environment which gives to the cell its shape. Other proteins offer a way across the membrane for certain molecules, fundamental for cell nutrition and signalling.

Beside the plasma membrane, there are also numerous biological membranes inside the cell organizing space into different organelles. These organelles are also vital for the maintaining and functioning of the cell. For example, on can cite the chloroplast in plant cells, where photosynthesis takes place; the mitochondria, responsible of the production of the fuel adenosine triphoshate; or the lysosome capable of degrading macromolecules. Each organelle membrane contains an unique set of proteins vital for its function.

1.1.1 Lipid composition of biological membranes

The molecular composition of a membrane is very complex, reflecting its various functions, as depicted in figure 1.1. The main constituents are lipids and proteins. The ratio of protein and lipids can vary a lot, depending on the cell function (see table 1.1 for a few examples).

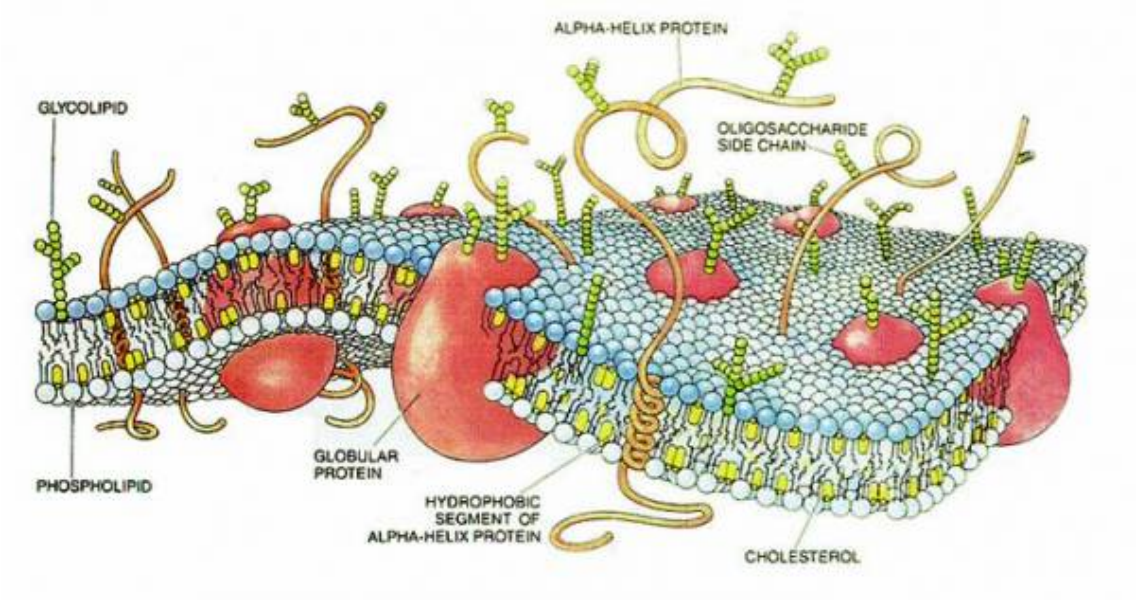

Figure 1.1: Sketch of cross section of a cell membrane [1]

Lipids are amphiphilic molecules with a hydrophilic headgroup exposed to the external part of the membrane and hydrophobic chains. They are assembled as a bilayer in the membrane.

The most common lipids found in animal membranes are glycerophospholipids, or phospholipids. Phospholipids are lipids containing two hydrophobic aliphatic chains connected to a hydrophilic headgroup by a glycerol. They contain a phosphate function in the headgroup part which makes the natural lipids either negatively charged or zwitterionic. Their amphiphilic structure gives them the ability to self-assemble in fluid bilayers. The core of this bilayer, being hydrophobic, is a two dimensional solvent in which membrane proteins and complex assemblies can move freely. Figure 1.2 shows the structure of the main phospholipids found

in animal cells. One can see that there is the hydrophilic headgroup containing the glycerol connector, the phosphate function and different possible headgroups. The two aliphatic chains are connected to the glycerol through an ester bond. The chemical structure of these chains can vary in function of the chain length (number of carbons) and unsaturation.

Some examples of the chains are drawn in figure 1.2. As for the nomenclature Ci:j refers to chains with a number i of carbon atoms in the chain and a number j of unsaturations. There are two nomenclatures to locate the double bound on the aliphatic chain [2]. In the Δ configuration, the number corresponds to distance of the unsaturation to the carboxyl carbon number. Shorthand ($n-$ or ω), the nomenclature used in the common language, refers to the distance from the terminal methyl group.

Other kind of lipids are also essential for the functioning and maintaining of the cell. Cholesterol and its derivatives are members of the steroids family. Cholesterol is synthesized by the cell to maintain an appropriate membrane fluidity [3]. Due to its activity with Low Density Liprotein (LPL) complexes responsible of cardiovascular diseases [4, 5], cholesterol is tremendously studied in biological as well as biophysical studies.

Sphingolipids are another class of lipids. Unlike glycerolipids which contain a glycerol to connect the hydrophobic chains to the hydrophilic headgroups, the connector is a sphingosine linked to a hydrocarbon chain and a hydrophilic headgoup. Sphingomyelin is a sphingolipid possessing a choline as headgroup. This lipid is able to form sheath which surrounds and isolate nerve cell axones. Moreover, sphingomyelin, as well as cholesterol, are a major constituent of lipid rafts which are microdomains implicated in manifold processes as signal transduction, endocytosis and cholesterol trafficking [6–8].

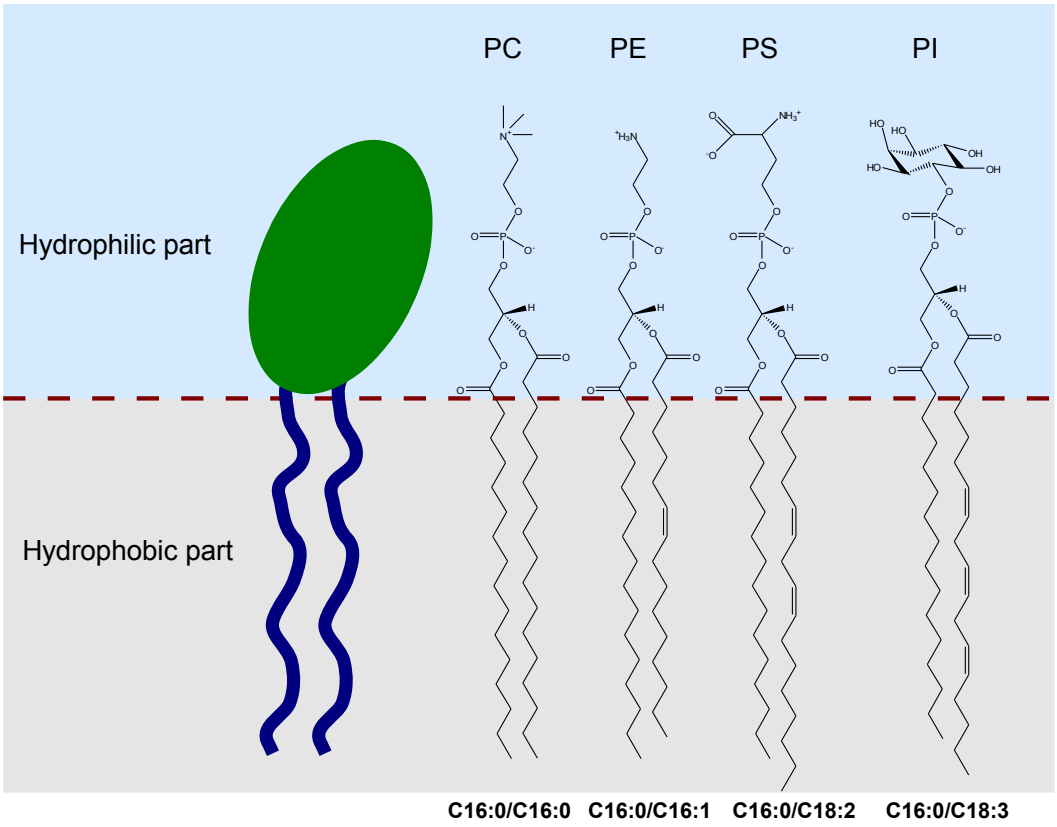

Figure 1.2: Left: schematic representation of a phospholipid composed of a hydrophilic headgroups and two hydrophobic tails. Right: chemical structure of the main phospholipids present in animals and yeast. The headgroups and tails differ. PC: phosphatidylcholine, PE: phosphatidylethanolamine, PS: phosphatidylserine, PI: phosphatidylinositol.

Table 1.1: Weight percent of proteins, lipids and carbohydrates in membranes. [9]

	Percentage by weight		
Membrane	Protein	Lipid	Carbohydrate
Human erythrocyte	49	43	8
Mouse liver	44	52	4
Chloroplast spinach lamella	70	30	0
Halobacterium purple membrane	75	25	0
Mitochondrial inner membrane	76	24	0
Myelin	18	79	3

1.2 Physical properties of lipid systems

1.2.1 Lipid polymorphism

Lipids, due to their amphiphilic nature, can display numerous liquid crystalline phases in water depending on lipid concentration and temperature [3]. Some lyotrophic phases (i.e. phases formed upon the addition of solvent) are shown in figure 1.3. The most common lipid phase found in nature is the lamellar, L phase (L_α for lamellar fluid phase) which consists of a lamellar array having long range order when mixed with water. It includes a lipid layer with a thickness d_L alternated with a water layer having a thickness d_W. A schematic drawing of lamellar phase is shown in figure 1.3.

In certain thermodynamic conditions, other phases can sometimes be more favorable like, for instance, the inverse hexagonal H_{II} phase (figure 1.3). This phase corresponds to two-dimensional arrays of cylinder hexagonally arranged in which the hydrophobic chain are oriented outside the cylinders. If lipids are in excess compared to water, the normal hexagonal H_I phase can be formed where the lipid tails are oriented inside the cylinders. In living organisms, the hexagonal phase can occur during a local phase transition during particular processes such as a tight junction between cells.

In particular cases, even more "exotic" phases can take place such as

the inverse bicontinuous cubic phases Ia3d and Pn3m (figure 1.3).

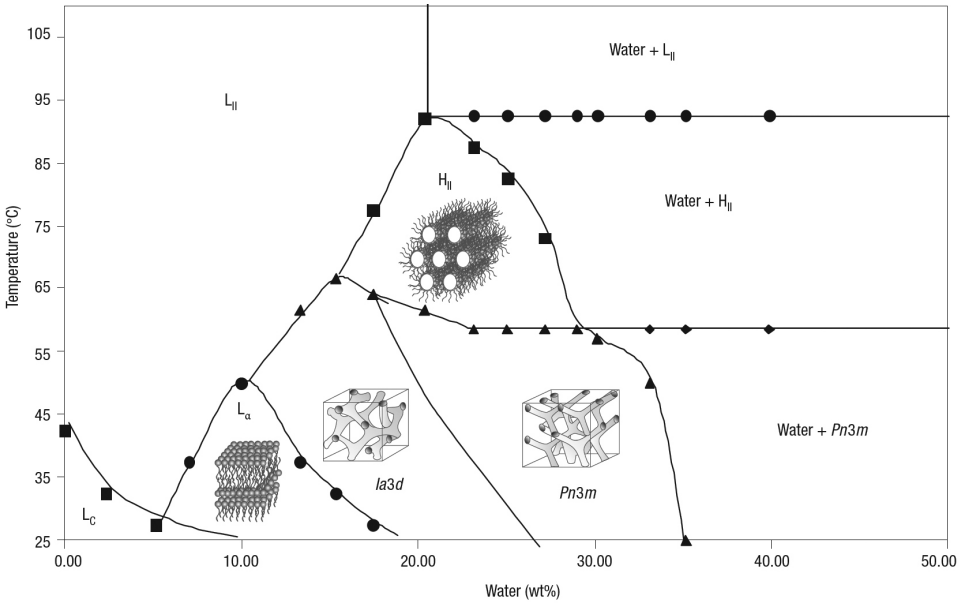

Figure 1.3: Phase diagram of monolinolein-water system, illustrating the structures of the mesophase encountered. L_c is the liquid crystalline phase; L_α is the lamellar fluid phase; H_{II}. is the inverse hexagonal phase and Ia3d and Pn3m are the double gyroid and double diamond bicontinuous reversed cubib phases, respectively. From [10]

These phases result from the optimization of intra- and inter-molecular interactions under some geometric packing constraints. Since the lamellar phase is predominantly encountered in nature because it is the most adapted phase to achieve the role of the cell membrane, this thesis deals only with lipids forming lamellar phases.

1.2.2 Membrane fluidity

The fluidity of the membrane is essential for the maintaining of the cell. At sufficiently low temperature, the bilayer in the L phase is effectively still and aliphatic tails are packed closely to each other in order to maximize the van deer Waals interactions. In this phase, called L_β phase, the chains are parallel to the layer normal. There is another gel phase, called $L_{\beta'}$

Table 1.2: Chain melting (gel to fluid) phase transition temperature (in °C) of some common diacyl chain of phosphatidylcholine (PC) in water as function of hydrocarbon chain length (from [11]).

Chains	T_m (°C)
C14:0/C14:0	23.5
C15:0/C15:0	33.5
C16:0/C16:0	41.5
C18:0/C18:0	55.5
C16:0/18:1Δ^9	-3
C18:1Δ^9/C18:1Δ^9	-18
C16:0/C18:2$\Delta^{9,12}$	-20

phase, where chains are tilted with respect to the layer normal. The tilt occurs when the headgroup area does not match the packing of the tail projected area and allows mismatch to be accommodated.

Upon heating, the bilayer undergoes a gel to fluid phase transition. In the fluid phase, or L_α phase, lipids are free to move in the plane of the bilayer and this results in an increase of the interfacial area per molecule and a decrease of the bilayer thickness. The phase transition temperature depends on various parameters such as lipid composition, salt concentration, pH and unsaturation degree of the chains. The phase transition temperature for unsaturated lipids is lower because of the free volume imposed by the double bond which avoids a close packing and causes a decrease of the van der Wall interaction. Table 1.2 shows the chain melting (gel to fluid) phase transition temperature of some common diacyl chain of phosphatidylcholine in water as a function of hydrocarbon chain length. In general, the phase transition temperature decreases when chains are shorter and more unsaturated. The presence of some molecules such as sterols, as well as deuterated molecules, also influence the membrane fluidity.

1.3 Importance of deuteration in biophysical studies on membranes

Labelling lipids by selectively replacing hydrogen by deuterium is often used for techniques such as Fourier transform infrared spectroscopy [12], NMR [13] or neutron scattering [14–16]. In the neutron field, the very high difference in scattering cross-section between hydrogen and deuterium makes it possible to design specific systems in order to highlight the parts of interest in a particular study. However, it has been shown that perdeuteration, i.e.replacing all the hydrogen atoms by deuterium atoms, can slightly modify physical properties of lipids such as melting phase temperature [17].

However, very few kinds of deuterated phospholipids are commercially available. It is very challenging to get lipids that are both perdeuterated and unsaturated. The main drawback of using fully saturated phospholipids is that they might not be biologically relevant because they are fluid only at relatively high temperature (see table 1.2).

There are two approaches to access perdeuterated phospholipids. The first one is by the chemical synthesis and the second one is by producing them by living cells able to grow in a fully deuterated environment.

1.4 Neutron diffraction for the elucidation of membrane structure

Historically, X-ray diffraction was the first method used to resolve biological structure at an atomic level. The best known example is the experiment performed by Watson and Crick in 1953 which resulted in the discovery of the double helix structure of DNA [18] and laid the foundation of molecular genetics.

X-ray diffraction has been widely used for structural biology; in particular diffraction from single crystals of proteins. Measurements from myoglobin provided the first protein crystal structure resolved by means of X-ray diffraction in 1961 [19]. However this technique has a fundamental

limitation imposed by crystal growth.

The first articles describing the use of neutron diffraction on biological systems are mainly found in the early 1970s [20]. The large difference in scattering cross section between hydrogen and deuterium makes neutrons scattering particularly interesting for studies of biological structures such as membranes. Moreover, neutrons do not disturb soft biological matter, can resolve the structure at an Å-scale and have a strong penetration power. In addition to membranes, there are numerous studies using neutrons to elucidate protein structures [21–24] and dynamics [25–28] as well as ribosomes [29, 30] and viruses [31].

1.4.1 Early studies using neutron scattering on membranes

Some seminal works carried out on natural or model membranes are presented in this section. Pioneering experiments on the structure of membranes involved the use of neutron diffraction from stacks of membranes. In the review that Schoenborn wrote in 1976 [32], the first experiments exploiting neutron diffraction from membranes are related to the structural elucidation of myelin by comparing results from X-ray diffraction [33, 34]. In this study, neutrons were used to validate the structure suggested by Caspar & al [35]. The scattering length density profile obtained from neutron experiments was consistent with the proposed myelin structure on the basis of X-ray experiments and yielded better values for the water content in the membrane.

Another early work is the study of the structure of phosphatidylcholine bilayers investigated by neutron diffraction from a stack of membranes [36]. This is the first neutron experiment carried out on artificial membranes composed of dipalmitoyl phosphatidylcholine (DPPC), i.e. a phospholipid containing two chains of 16 carbons and no insaturations and a phosphatidylcholine headgroup. To resolve the structure of stacks of DPPC, the H_2O - D_2O exchange was achieved at low relative humidity. This exchange technique allowed resolving the scattering length density profile of a stack and deducing the thickness of the water layer separating the lipid strips.

The last example of early neutron scattering experiments on membrane is the work on retinal photoreceptor membrane carried out by Yeager [37]. The system consists of periodically stacked lipid discs containing proteins which make a system particularly well suited for neutron scattering experiments. The scattering length density profiles suggested that some proteins are located inside the membrane on the external disc side and extends into the cytoplasmic space. Therefore, small angle neutron scattering from rhodopsin in solution was used to resolve the shape of the proteins and a satisfying model was found. The data were improved by using a magnetic orientation of isolated disc membranes [38].

Purple membrane

Purple membrane is, as in the example explained above, another retina-containing membrane extracted from *Halobacterium cutirubrum* cells. It was first identified by Stoeckenius and Kunau in 1968 [39]. The membrane contains one type of protein, bacteriorhodopsin, packed in a P3 lattice in a lipid matrix and containing extensive α-helical regions [40, 41]. Observations from combined electron microscopy and electron diffraction showed that the bacteriorhodopsin contained up to 7 α-helices lying more or less perpendicular to the membrane plane [42]. The ratio of protein to lipid mass is about 3.

Neutron diffraction on purple membrane led to the finding that the membrane stacks are laterally arranged in a hexagonal lattice. The difference Fourier maps obtained from the scattering from stacks in H_2O and D_2O were used to find the areas of hydration and allowed the number of exchangeable hydrogen in the lipid and protein areas to be determined [43].

1.4.2 Neutron reflectometry for membrane studies

More recently, model membranes composed of a few and well-defined molecules have been used in membrane biophysics, including the neutron field. Neutron reflectometry is a very powerful technique for membrane research and the field has grown constantly during the last decade [44].

Specular reflection gives only composition profiles along the z-axis, i.e. the axis parallel to the surface normal. There is the possibility to use off-specular scattering from the interface in order to probe in-plane structure but this technique will not be discussed in this thesis. Due to the ability to change the isotopic constitution of the subphase (also called contrast), it is possible to match in or match out some parts of the membrane. For instance, it is possible to measure the interaction of a hydrogenated drug with perdeuterated lipid, i.e. lipid in which all the hydrogen atoms have been replaced by deuterium, in D_2O. Consequently, the scattering length density of the lipid bilayer will match that of the subphase, and the reflection will mainly come from the hydrogenated material.

Single supported membranes

This system is the simplest to be studied by neutron reflectometry. It consists of a single lipid bilayer deposited on a solid substrate and reflection occurs at the solid-liquid interface. The main advantage of this system is the fact that it is very easy to prepare and very high lipid coverage is reasonably achievable. There are mainly two ways to prepare such planar supported bilayer: either by Langmuir Blodgett and Langmuir Schaefer (LB - LS) deposition [45] or by the vesicle fusion method [45, 46], both will be described in the following chapter. Let us just mention the existence of another possibility to prepare bilayer onto a solid planar substrate. There is the method developed by Tiberg *et al.* where a lipid bilayer is gradually formed by using micelles containing lipids and non-ionic dodecyl maltoside surfactant [47].

One of the main applications of neutron reflection from supported lipid bilayer is their interaction with proteins. The key interest resides in the ability of peptides to penetrate the structure of bilayer or induce structural changes. For example, Chenal *et al.* investigated the insertion of the toxin T-domain in lipid bilayer by specular neutron reflectometry and solid-state NMR spectroscopy at different pH [16]. By using LB - LS deposition, they used three kinds of model membranes composed a mixture of DPPC and DPPA. The first sample was fully hydrogenated, the second

one fully deuterated and the third one was asymmetric: the inner leaflet was fully deuterated and the outer leaflet fully deuterated. Thanks to the selective deuteration, they determined the progress of the T-domain penetration within the model membrane as a function of the acidification of the subphase.

Another work on lipid bilayer - peptide interactions investigated by neutron reflectometry is the localization of the enzyme phospholipase A_2 (PLA2) [15] and the lipid degradation induced by this enzyme [48]. Phospholipases A_2 are responsible for the lipid degradation and release of fatty acids from the second carbon group of glycerol. The authors used partially deuterated d31-POPC to follow the distribution of the lyso-lipid and fatty acid in *Naja mossambica mossambica* hydrolysis. The saturated chain of d31-POPC is fully deuterated while the unsaturated chain is fully hydrogenated. They observed that the scattering length density of the chain region decreases upon the action of the phospholipase. Since only the saturated chain of POPC was perdeuterated, the decrease in scattering length density implies that there is a significant asymmetry in the distribution of the hydrolysis products. Therefore, they found that the lyso-lipid leaves the membrane while the number of PLA2 molecules bound to the interface increases with increasing fatty acid content.

Neutron reflection from supported membranes is also good for the investigation of gene delivery vehicles. Callow *et al.* investigated the interaction of lipid-DNA complexes or lipoplexes with model membrane in order to study the transfection of cells by DNA for the purposes of gene therapy [49]. Vesicles made of neutral and cationic lipids have been shown to be more efficient than fully cationic vesicles for the DNA transfer. They investigated the role of these neutral or "helper" lipids such as DOPE or cholesterol. The authors exposed perdeuterated supported bilayer composed of DMPC : DPPS (9:1) to different fully hydrogenated lipoplexes.

Neutron reflection is also an appropriate tool to study the lipid mixing between two leaflets. By preparing asymetric membrane by means of LB - LS methods in which one leaflet was fully deuterated and the other was fully hydrogenated, Gerelli *et al.* investigated the mixing of DMPC within model membranes through the gel to fluid phase transition [14].

The intrinsic features of neutron being scattered differently according to the isotopic composition made this technique unique for such investigation.

1.5 Summary and goals of the thesis

The examples listed above show that, at the early stage of the use of neutron scattering experiments, researchers were more inclined to use samples immediately extracted from living organisms to elucidate their structure or dynamics. Nowadays, instrumental improvement is such that sample quality is the "bottle-neck" of structure elucidation.

The examples from recent papers cited above show that the possibility to match in or out some parts of the membrane by using selective deuteration has given rise to the use of model lipid bilayers because the isotopic content can be precisely controlled. It explains the recurrent use of model membrane composed of usually fully deuterated DMPC (C14:0/C14:0 PC) and DPPC (C16:0/c16:0), or partially deuterated POPC, i.e. C16:0/C18:1 PC. Indeed, it is very difficult and expensive to commercially obtain unsaturated and deuterated lipids. However we have seen that unsaturation is responsible for the lowering of the gel-fluid phase transition temperature and therefore plays an important role for the membrane fluidity.

In this repect, using organisms capable of growing in a fully deuterated environment could be a promising methods to access such perdeuterated material since these organisms produce them naturally. After describing the experimental methods used in this thesis, a chapter is dedicated to the description and results of the lipid production by the methylotropic yeast *Pichia pastoris*. Yeast was chosen as production engine since its natural phospholipid composition is close to the human one, i.e. mainly PC and PE. The headgroup and tail composition as function of the isotopic medium is presented as well as the influence of the growth medium temperature. In addition, a protocol used to purify PC and PE and a preliminary analysis of sphingolipids are also described.

The third chapter deals with the interaction of an antifungal drug, amphotericin B, with reconstituted supported bilayers measured by neutron

reflectometry. Different membranes were reconstituted on a solid substrate, therefore the structural characterization of every bilayer is performed, which allows finding the influence of lipid composition on the bilayer structure. Since the material used refers to that described in the previous chapter, the two chapters are closely related.

Another chapter is about the interaction of plant lipid precursors with reconstituted thylakoid membranes on silicon and sapphire substrates. The first part deals with the localization of the precursor diacylglycerol (DAG), obtained in deuterated form from the yeast *Pichia pastoris*. The second part is the study of the flip flop of deuterated phosphatidic acid (PA), also obained from deuterated yeast, in the reconstituted chloroplast membrane.

The last chapter is devoted to the interaction of a small molecule, resveratrol, which is present in some fruits and has beneficial properties on human health. This molecule is responsible of the "French paradox", i.e. an inverse correlation between wine consumption and low rate of coronary heart disease. To have a precise localization of this molecule within the membrane, it was decided to use model lipids selectively deuterated at the chain or headgroup regions. The joint analysis of the two isotopically different bilayer has made the localization of resveratrol possible. In addition, the effect of cholesterol on the resveratrol penetration is also investigated.

In conclusion, the goal of this thesis is to employ the properties of complex lipid systems extracted from living organisms in order to mimic in the most relevant way the conditions encountered in the native cell membrane and to probe the interaction of molecules with model and native lipid bilayers. We investigated the structure of supported lipid bilayers extracted from yeast and plant cells and their interactions with different molecules by neutron reflectivity. This approach is more robust from a biological point of view than using model membrane which can sometimes be too simplistic to ideally mimic cell membranes. However, difficulties can arise from the sample preparation, lipids extraction and lipid bilayer deposition.

In parallel to these complicated systems, we investigated the interac-

tion of simpler membranes, composed of selectively deuterated DPPC, with resveratrol. The partial deuteration allowed a better localization of resveratrol within the membrane. This shows that model membranes can be essential because obtaining such lipids from living organism can be very challenging.

Chapter 2

Experimental techniques, materials and methods

2.1 Neutron reflectometry

2.1.1 Introduction

In this work, the main experimental technique used for the investigation of the structure of lipid bilayers in native form as well as after the incubation of various drugs was neutron reflectometry. Its ability to resolve structure at the Å-scale and the possibility to contrast match some parts of the system makes it the appropriate tool for structural studies on membrane research.

Neutrons are scattered in matter by nuclei, unlike X-rays which are scattered by the electron cloud, and the difference in scattering cross section for hydrogen and deuterium is very high. Consequently, neutron techniques are very useful for studying structural properties of highly protonated materials such as biological compounds because it is possible to substitute the hydrogen atoms of the compound by deuterium in order to highlight it within a fully hydrogenated surrounding medium.

Neutron reflectometry allows getting structural properties such as thickness, solvent penetration or roughness of adsorbed layers at interfaces. It is particularly suited for structural studies of lipid bilayers because neu-

tron wavelengths are on the Å-scale, neutrons have a strong penetration power and do not destroy soft biomaterials.

2.1.2 Theoretical principles

Neutron-Matter Interactions

The two main interactions of neutrons with matter are the strong interaction with nuclei and the magnetic interaction with magnetic moments [50]. In this work, only the strong interaction with nuclei will be considered. The Schrödinger equation of an elastically scattered neutron can be written as

$$\frac{\hbar^2}{2m}\nabla^2\psi(\mathbf{r}) + V(\mathbf{r})\psi(r) = E\psi(\mathbf{r}) \tag{2.1}$$

where m is the neutron mass, $\psi(\mathbf{r})$ is the neutron wave function, $E(\mathbf{r})$ is the energy and $V(\mathbf{r})$ is the potential describing the surrounding medium of the neutron. For specular reflection, i.e. when the angles of incidence and reflection are equal, only the change of momentum normal to the surface has to be taken into account. Therefore, the Schrödinger equation of a neutron scattered in one dimension can be written as

$$[\frac{\hbar^2}{2m}\frac{d^2}{dz^2} + E - V(z)]\psi(z) = 0 \tag{2.2}$$

The local wavevector normal to the surface is defined by

$$k_z(z) = \frac{2m[E - V(z)]^{1/2}}{\hbar} \tag{2.3}$$

Then, equation 2.2 can be rewritten as

$$[d^2/dz^2 + k_z^2]\psi(z) = 0 \tag{2.4}$$

Since the nuclear size is much smaller (10^{-15} m) than the thermal neutron wavelength (10^{-10} m), the potential can be considered as point-like and isotropic. Therefore, within the Born approximation, this potential can be described as a Fermi "pseudopotential" as

$$V_F(z) = \frac{2\pi b\hbar^2}{m}\delta(z) \tag{2.5}$$

where b is the scattering length of the nuclei and z is the position of the neutron. The optical potential V_0 is the local average of the pseudo-potential and is estimated by averaging the scattering length density of the material. Consequently,

$$V_0(z) = \frac{2\pi\hbar^2\rho}{m} \tag{2.6}$$

where

$$\rho = \sum_i n_i b_i \tag{2.7}$$

ρ is the averaged scattering length density, b_i is the scattering length and n_i is the molecular volume of the nuclei i.

Neutron optical indices

When a wave propagating in a medium encounters another medium with a different refractive index at a certain angle, the incident radiation undergoes a reflection. The refractive index n of a material can be described as

$$n = 1 - \delta_N + i\beta \tag{2.8}$$

The imaginary part arises only when the material is absorbing. In case of neutrons, the imaginary part is most of the time insignificant (i.e. $\beta \simeq 0$). The second term is given by [51, 52]

$$\delta_N = \frac{\lambda^2}{2\pi}\rho \tag{2.9}$$

where λ is the wavelength of the incident beam.

The value of δ_N for a wide range of materials is generally in the order of magnitude of 10^{-6}. Therefore, the refractive index is usually slightly smaller than 1.

Reflection arises when the refractive indices of the two media are different (see figure 2.1). The ratio between the two refractive indices determines angle of reflection according to the Snell's law

$$n_1 cos(\theta_1) = n_2 cos(\theta_2) \tag{2.10}$$

where θ_1 and θ_2 are the angles of incidence and refraction, respectively (figure 2.1).

If $n_1 > n_2$, then $\theta_2 < \theta_1$ and an incident angle exists below which the wave is totally reflected.

The wavevector or momentum transfer in vacuum along the z direction is

$$k_{z,0} = (2\pi/\lambda) sin\theta \tag{2.11}$$

where λ is the wavelength of the radiation and θ is the angle between the incoming beam and the interface. In a medium i, the momentum transfer is modified in the following way

$$k_{z,i} = \sqrt{k_{z,0}^2 - 4\pi\rho_i} \tag{2.12}$$

where ρ_i is the scattering length density of the medium.

The refractive index can also be written as

$$n^2 = \frac{k_{z,i}^2}{k_{z,0}^2} = 1 - \frac{4\pi\rho_i}{k_{z,0}^2} = 1 - \frac{\lambda^2\rho_i}{\pi} \tag{2.13}$$

Since ρ_i is much smaller than 1, for neutron wavelengths < 60 Å

$$n \approx 1 - \frac{\lambda^2\rho_i}{2\pi} \tag{2.14}$$

Neutron reflection from an interface

The solutions of equation 2.4 above and below the surface are

$$\psi(z) = \left\{ \begin{array}{l} e^{ik_{1\perp}z} + re^{-ik_{1\perp}z} \\ te^{ik_{2\perp}z} \end{array} \right\} \tag{2.15}$$

where r and t are the reflection and transmission coefficients, respectively. To satisfy the conditions of continuity, $\psi(0)$ and $|\frac{d\psi(z)}{dz}|_{z=0}$ must be equal at both sides of the interface. Therefore,

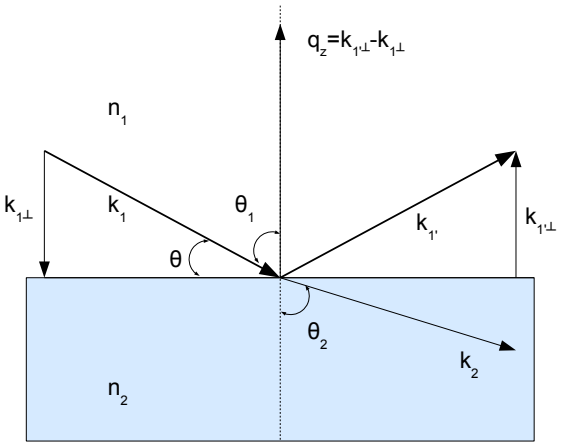

Figure 2.1: Reflection and refraction of a plane wave coming from the medium n_1 to the medium n_2.

$$\begin{aligned} 1 + r &= t \\ k_{1\perp}(1 - r) &= k_{2\perp}t \end{aligned} \tag{2.16}$$

This leads immediately to the Fresnel coefficients known in optics

$$\begin{aligned} r &= \frac{k_{1\perp} - k_{2\perp}}{k_{1\perp} + k_{2\perp}} \\ t &= \frac{2k_{1\perp}}{k_{1\perp} + k_{2\perp}} \end{aligned} \tag{2.17}$$

In reflectometry, the wave vector $q_z = k_{1\perp} - k_{1'\perp} = \frac{4\pi}{\lambda} sin(\theta)$ is conventionally used (see figure 2.1). What is measured is the intensity, i.e. the squared amplitude of the Fresnel coefficient as

$$R_F = r^2 = \left[\frac{q - (q^2 - q_c^2)^{1/2}}{q + (q^2 - q_c^2)^{1/2}} \right] \tag{2.18}$$

where q_c is the wave vector value at the critical angle. Figure 2.2 shows the calculated reflectivity from an air - silicon interface. The critical angle q_c is also depicted in this graph.

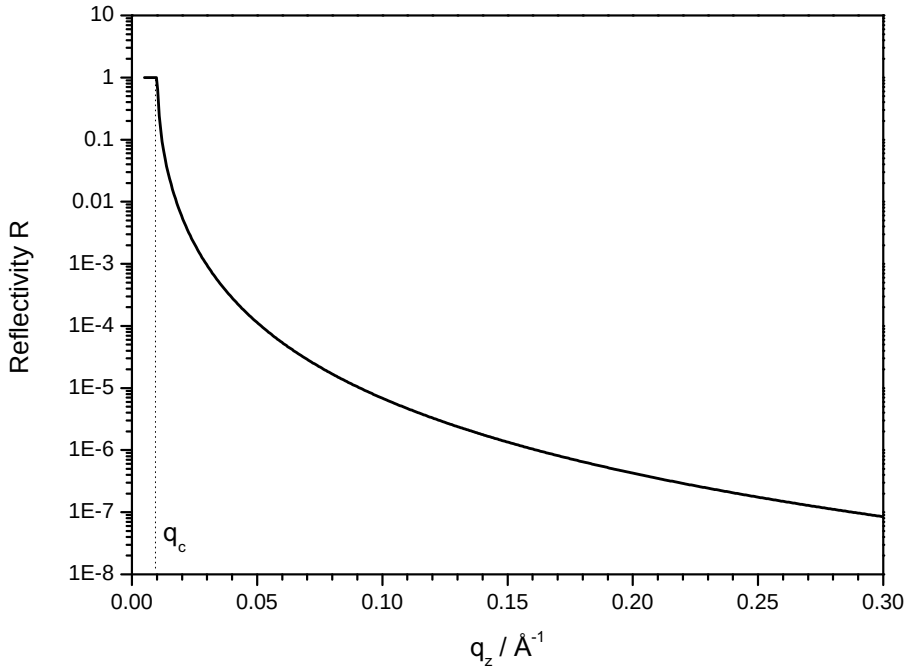

Figure 2.2: Calculated reflectivity from air - silicon interface. The critical edge q_c below which the reflectivity is total is in this case 0.00913 Å^{-1}.

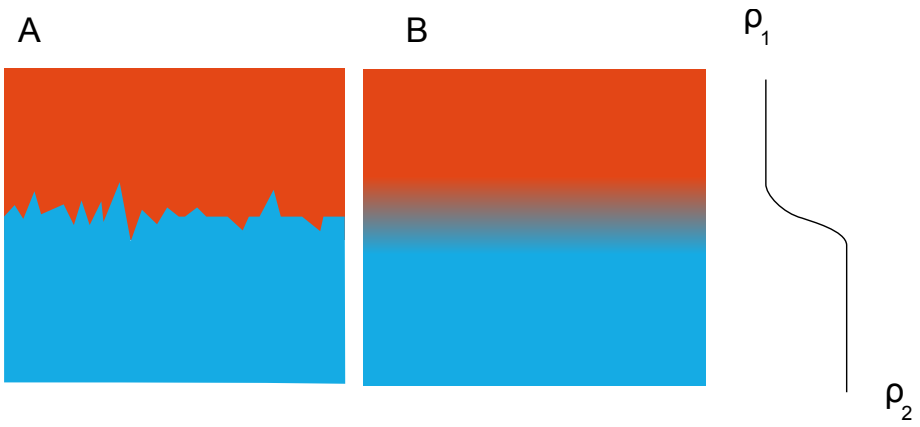

Figure 2.3: Schematic representation of A) roughness and B) interpenetration of two adjacent media ρ_1 and ρ_2.

Roughness

The interface between two media is never infinitely sharp. There might be either roughness or interdiffusion. The figure 2.3 depicts the roughness and interdiffusion between two adjacent media ρ_1 and ρ_2. The mathematical treatment is the same for both phenomena. The approach is to convolute the sharp density profile with a Gaussian smoothing function as

$$G(z) = \frac{1}{(2\pi)^{1/2}\sigma} e^{-z^2/2\sigma^2} \tag{2.19}$$

where σ is the standard deviation of the Gaussian function, which is proportional to the roughness. By convoluting this function with the Fresnel reflectivity, we obtain

$$R(q) = R_F(q) e^{(-4q^2\sigma^2)} \tag{2.20}$$

One can note here that the roughness has a damping effect on the reflectivity curves. The higher the standard deviation of the Gaussian function, i.e. the extent of the roughness, the lower the reflectivity, as shown in figure 2.4.

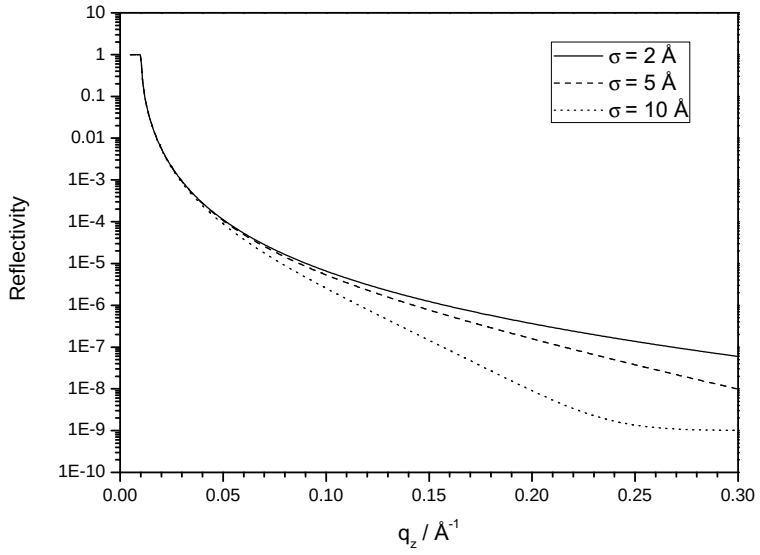

Figure 2.4: Calculated reflectivity at the air - silicon interface with a roughnesses of 2, 5 and 10 Å.

Neutron reflection from a homogeneous slab

In the case of a slab located between two semi-infinite media (see figure 2.5), the reflection arises from different contributions. The figure 2.5 depicts the different ways transmission and reflection coefficients that the initial wave can follow. The total reflection coefficient can be written as the series

$$\begin{aligned} r_{slab} &= r_{12} + t_{12}r_{23}t_{21}e^{2i\beta} + t_{12}t_{21}r_{21}r_{23}^2e^{4i\beta} + t_{12}t_{21}r_{21}^2r_{23}^3e^{6i\beta} + ... \\ &= r_{12} + t_{12}r_{23}t_{21}e^{2i\beta}[1 + r_{12}r_{23}e^{2i\beta} + r_{12}^2r_{23}^2e^{4i\beta} + ...] \\ &= r_{12} + t_{12}r_{23}t_{21}e^{2i\beta}\sum_{m=0}^{\infty}(r_{12}r_{23}e^{2i\beta})^m \end{aligned} \tag{2.21}$$

where β is the phase difference of a wave that has travelled once through the layer. It is expressed as

$$\beta = \frac{2\pi sin\theta_2}{\lambda}\Delta_1 \tag{2.22}$$

where Δ_1 is the thickness of the slab. This geometric series can be summed to give

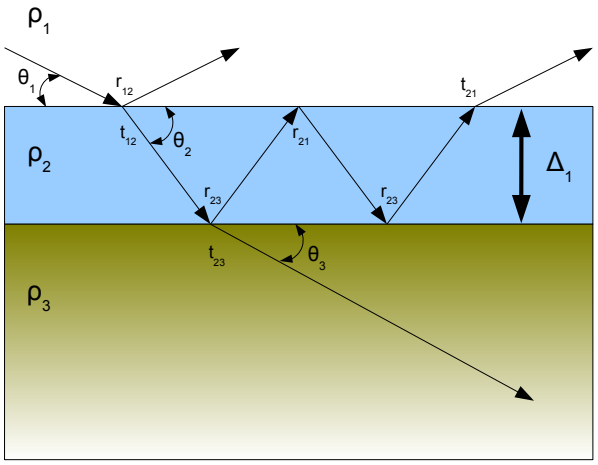

Figure 2.5: Reflection and refraction of a plane wave coming from the medium n_1 to the medium n_1.

$$r_{slab} = r_{12} + t_{12}r_{23}t_{21}e^{2i\beta}\frac{1}{1 - r_{12}r_{23}e^{2i\beta}} \tag{2.23}$$

Knowing that

$$r_{12} = r_{21}$$

and

$$r_{12}^2 + t_{12}t_{21} = \frac{(k_{1\perp} - k_{2\perp})^2}{(k_{1\perp} + k_{2\perp})^2} + \frac{2k_{1\perp}2k_{2\perp}}{(k_{1\perp} + k_{2\perp})^2} = \frac{(k_{1\perp} + k_{2\perp})^2}{k_{1\perp} + k_{2\perp})^2} = 1$$

one can rewrite the equation 2.23 as

$$r_{slab} = \frac{r_{12} + r_{23}e^{2i\beta}}{1 + r_{12}r_{23}e^{2i\beta}} \tag{2.24}$$

The measured reflectivity is given by the squared modulus of the total reflection coefficient

$$R = |r_{slab}|^2 = \frac{r_{12}^2 + r_{23}^2 + 2r_{12}r_{23}cos(2\beta)}{1 + (r_{12}r_{23})^2 + 2r_{12}r_{23}cos(2\beta)} \tag{2.25}$$

Neutron reflection from a stratified interface: the optical matrix method

When the reflection arises from a stack of layers having a different thickness and scattering length density, a convenient way to compute it is to resort to the optical matrix method. Let us assume that the system is composed of i layers between two semi-infinite media n_0 and n_{i+1}. The incoming beam is first transmitted and reflected at the n_0, n_1 interface. The transmitted beam encounters the n_1, n_2. This scenario is repeated until the beam encounters the last interface n_i, n_{i-1}. A characteristic matrix can be calculated for each layer:

$$c_i = \begin{bmatrix} e^{\beta_i} & r_{i,i+1}e^{\beta_i} \\ r_{i,i+1}e^{-\beta_i} & e^{-\beta_i} \end{bmatrix} \tag{2.26}$$

where $r_{i,i+1}$ is the modified Fresnel coefficient convoluted with the Gaussian smearing function in order to take into account the roughness of the layer.

A resultant matrix is calculated as

$$M = \prod_{i=0}^{n} c_i \tag{2.27}$$

The reflectivity is calculated as

$$R = \mid \frac{M_{10}}{M_{00}} \mid^2 \tag{2.28}$$

2.1.3 Instruments and data analysis

The reflectivity is measured in function of the wavevector q_z. Since q_z depends on the wavelength and the angle between the incoming beam and the interface, the reflectivity can be measured by varying the wavelength at a constant angle or vice versa. The monochromatic mode consists in varying the incident angle by keeping the wavelength constant, while the time of flight (TOF) mode consists in varying the incoming wavelength and keeping the incident angle constant. In this work, all the neutron reflectivity experiment are carried out with the TOF mode.

Neutron speed v can be related to the wavelength λ through de Broglie relation

$$v = \frac{h}{m\lambda} \tag{2.29}$$

where h is the Planck constant and m is the neutron mass. The wavelength can be obtained by measuring the time t taken by the neutron to travel the distance L from the source to the detector

$$\lambda = \frac{ht}{mL} \tag{2.30}$$

In practice, the neutron beam comes from a set of choppers made of a highly adsorbing-neutron material which selects the boundary of a wavelength distribution of 2 Åto 20 Å. The reflectivity is measured at each λ, resulting in the reflectivity curve $R(q_z)$.

The reflectivity is measured over a q_z range of 0 to 0.3 $Å^{-1}$ for the instruments used in this study. Above this range, the background is too high because of the incoherent scattering contribution from the liquid subphase and background from the substrate. Since the wavelength distribution is too narrow to span the whole q_z range, the reflectivity is measured at two different incident angles and merged.

The resolution depends on the angular divergence of the beam ($\Delta\theta$) and wavelength spread ($\Delta\lambda$):

$$\left(\frac{\delta q_z}{q_z}\right)^2 = \left(\frac{\delta\theta}{\theta}\right)^2 + \left(\frac{\delta\lambda}{\lambda}\right)^2 \tag{2.31}$$

D17 and FIGARO characteristics

D17 is a neutron reflectometer with horizontal scattering geometry (vertical surfaces) designed to be as flexible as possible in resolution and modes of operation. FIGARO is a high flux, flexible resolution, time-of-flight reflectometer with a vertical scattering plane. Therefore it is optimized for the study of horizontal surfaces such as free liquids.

All the experiments in this thesis were performed in TOF mode with a useful range of about 2-20 Å (depending on the setup). A pair of choppers

is used to pulse the incoming beam whose phase separation defines the pulse time width. The beam is collimated by two slits which are separated by 3.5 m for D17 and 2.065 m for FIGARO. Both D17 and FIGARO detectors consist of tubular aluminium monoblock filled with ^{3}He gas and are two-dimensional (250 X 500 mm^2 for D17 and 500 x 250 mm^2 for Figaro) and can achieve a resolution of 1.2 x 7.6 mm^2 for D17 and FIGARO (pixel width x tube height). The D17 detector can be translated from 1.0 to 3.1 m from the sample position and rotated up to 50° from the direct beam axis and the Figaro detector can be translated from 1.0 to 2.8 m from the sample position.

For each instrumental setup it is necessary to measure the beam passing straight through the solid substrate (i.e. silicon or sapphire), called transmission, in order to normalize the absolute reflectivity.

The principle of background subtraction is the following: the area of the reflected peak x is chosen and its integration gives the number of counts n_x. Repeating the same procedure with a larger area y, still centered on the reflected peak, gives a number of count n_y. The difference in number of count $n_y - n_x$ divided by the difference in area $y - x$ gives the background counts per area around the reflected peak.

Similar sample environment is used on the two instruments. For solid-liquid measurements, the blocks are clamped in sample holder as shown in figure 2.6. One inlet and one outlet connected to a pump allows flushing the different subphases. Moreover, the holder is connected to a bath-thermostat in order to control the temperature.

Data analysis

As it is written above, the intensity, i.e. the squared modulus of the total reflection coefficient, is measured. That means, like all the scattering technique, that the phase information is lost. Consequently it is not possible to extract the structural parameters directly from the experimental reflectivity curves. A model has first to be established and the parameters of this model must be varied until the reflectivity curve calculated from the model matches the experimental data. However, there is generally more

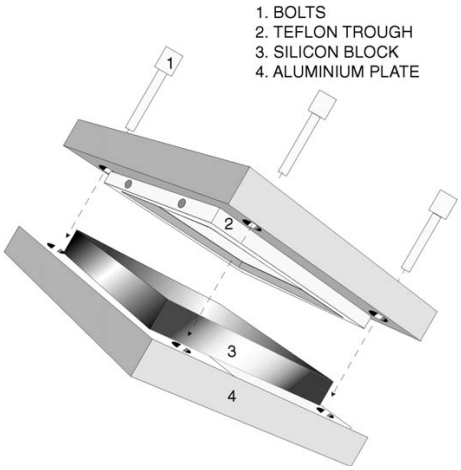

Figure 2.6: The sample holder used to mount the silicon block (from [53]).

than one unique solution. One has to be very careful when finding a solution and to ensure that there are no other plausible answers.

The optical model for a single lipid bilayer is composed of a stack of layers (see figure 2.7). The lipid bilayer itself is decomposed in three layers, one corresponding to the outer headgroup region, one corresponding to the tail region and one corresponding to the inner headgroup region. In case of a symmetric bilayer, we can constraint the model by imposing the same thickness, scattering length density and solvent fraction for both headgroup regions as a first approximation. Besides these layers, a water layer separating the lipid bilayer from the substrate can be included in this optical model as well as the two semi-infinite media which are the subphase and the substrate (either silicon or sapphire).

It can happen that the lipid bilayer is not fully deposited onto the substrate. Therefore, there might be some "holes" laterally distributed within the plane of the bilayer. Moreover, the hydrophilic headgroups are surrounded by an intrinsic hydration shell. One has to take into account the contribution of the water for the calculation of the scattering length density of each layer. The total scattering length density of a layer ρ including the contribution of the materials and water is

$$\rho = (1 - \phi_s)\rho_m + \phi_s\rho_s$$

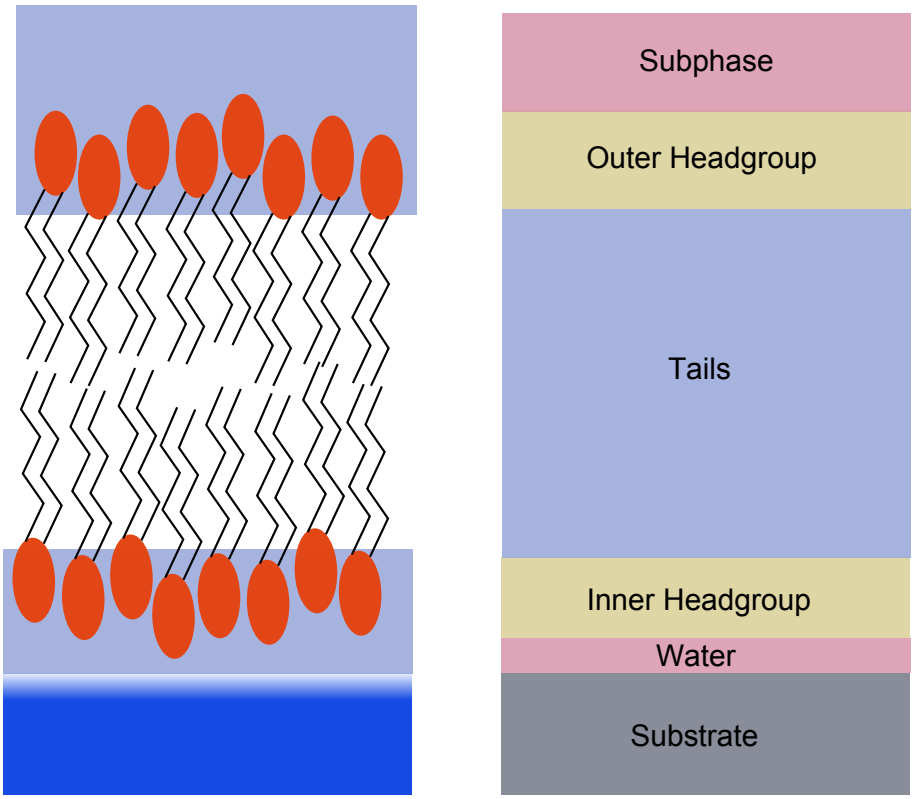

Figure 2.7: Left: scheme of a planar lipid bilayer deposited on a substrate. Right: neutron optical model used to fit the bilayer.

where ρ_m is the scattering length density of the dry material, ρ_s and ϕ_s are the scattering length density and the volume fraction of the solvent, respectively.

If the model contains too many parameters, it might happen that some of them will be either fully correlated or fully anti-correlated. The contrast variation technique is used to reduce this problem. By measuring the reflectivity from the same lipid bilayer in different contrasts, i.e. subphases composed of a mixture of light and heavy water, more constraints are added to the model to eliminate some alternative fits and decorrelate some parameters. The reflectivity curves from the same bilayer measured in different contrasts were fitted simultaneously.

All the analysis was done by using the Motofit software [54]. The reflectivity was calculated from the model by the optical matrix method described above. The fitting procedure was done by minimizing χ^2, which reflects the difference between the model and experimental data as

$$\chi^2 = \frac{1}{N} \sum_N \frac{(R_{meas} - R_{calc})^2}{\sigma^2} \tag{2.32}$$

where N is the total of number of points measured, (in this case the number of points in the reflectivity curve), σ is the variance, R_{meas} and R_{calc} are the calculated and measured values. The algorithm used to minimize χ^2 is the genetic optimisation.

2.2 Materials

All water used for experiments was ultra pure (18.2 MΩ.cm at 25°C). All D_2O for experiments was provided by the ILL and had a purity > 99.9 %. Phospholipids and cholesterol were purchased from Avanti Polar Lipids (Lancaster, AL) and were used without any further purification.

Sodium chloride (purity > 99.5 %), calcium chloride dihydrate (purity > 99.0 %), amphotericin B (from *Streptomyces sp.*, purity 80%), chloroform (purity > 99.8 %), methanol (purity > 99.9 %), ethanol (purity > 99.8 %), acetone (purity > 99.8 %), dimethylsulfoxide (DMSO) (purity > 99.9 %), n-hexane (purity > 97.0 %), isopropanol (purity > 99.9 %), acetic acid (purity

> 99.5 %), sulfuric acid (purity: 95 - 98 %) and hydrogen peroxide in solution (> 30%) were purchased from Sigma-Aldrich (St Quentin Fallavier, France) and were used without any further purification.

P. pastoris GS115A strain was purchased from Invitrogen (Carlsbad, CA). Peptone was purchased from Oxoid (Hampshire, En), hydrogenated glycerol (pur. > 99.5%) from Euromedex (Souffleweyersheim, F) and deuterated glycerol from Euriso-Top (CEA-Saclay Gif sur Yvettes, F). All the salt compounds used for yeast growth were purchased from Sigma-Aldrich (St Quentin Fallavier, France).

Trans-resveratrol in powder form was purchased from ABCR GmbH and Co (Germany). Silicon and sapphire blocks were purchased from Synchrotronix (France) and polished to the face (111) to a roughness < 3 Å.

Thylakoids lipids were extracted from spinach *Spinacia oleracea* purchased from a local market.

2.3 Lipid bilayer deposition

Neutron reflectometry requires the use of planar lipid bilayers. There are different ways to deposit lipid bilayer onto a substrate, the most used ones are the vesicle fusion method and the Langmuir-Blodgett and Langmuir-Schaefer (LB-LS) deposition [45].

The Langmuir-Blodgett and Langmuir-Schaefer techniques are used for the deposition of amphiphile layers on a substrate. The bilayer is deposited onto the solid substrate from a lipid monolayer spread at the air-water interface. The advantage of this technique is that we can control the packing at which lipids are deposited. Moreover, it is possible to deposit asymmetric lipid bilayers.

The vesicle fusion method involves suspending unilamellar lipid vesicles in pure water or in salt solution. When brought in contact with a planar substrate, the vesicles will spontaneously fuse and disrupt to form a planar supported lipid bilayer on the surface. An appropriate technique to survey this phenomenon is the Quartz Crystal Microbalance with Dissipation monitoring (QCM-D) since it can measure the mass adsorbed onto the surface and also the visco-elastic properties of the adsorbed material.

It is therefore possible to figure out if the soft and flexible adsorbed vesicles have disrupted to form a more rigid bilayer. The advantage of this technique lies in the fact that since the process is carried out *in situ*, it is possible therefore to characterize the solid substrate before the formation of the planar supported bilayer.

2.3.1 Substrate cleaning

Since neutron reflectometry is a technique very sensitive to material at the interface, it is very important to be careful to ensure the solid substrate is perfectly cleaned. Powder-free gloves were worn at all times whenever the substrates were used and at no time was the polished face touched.

Silicon and sapphire blocks were first cleaned by a mild Piranha solution (10% of hydrogen peroxide, 40 % sulfuric acid, 50 % water) for 15 minutes at 85°C if they were in contact with a bivalent salt solution such as calcium chloride during a previous experiment. Blocks were then cleaned in chloroform, acetone and ethanol for 10 minutes per solvent by repeated sonication. Immediately before the deposition the silicon surface was treated by UV/ozone radiation for 30 minutes in order to make the surface hydrophilic [55].

2.3.2 Langmuir-Blodgett deposition

The Langmuir trough, named after the work performed by Irving Langmuir in 1917 [56], allows investigating the surface pressure behaviour of insoluble monolayers at the air-water interface. This technique has been used for polymer films as well as biological systems as for example lipid monolayers interacting with proteins or drugs. The technique allows also depositing asymmetric layers onto a substrate by the Langmuir-Blodgett and Langmuir-Schaefer methods [45]. This deposition technique is particularly useful for the investigation of processes which require asymmetric lipid bilayer preparation, such as flip-flop [14].

Surface pressure - Area isotherm

Molecules within a material always have a degree of attraction towards each other. This attraction is called cohesion and depends on the properties of the material. The interface between two media, e.g the interface between air and water, is a particular region where molecules experience a lack of cohesion since they are not isotropically distributed. This region is more unstable in terms of thermodynamics and the surface is always the smallest possible. The surface tension γ of the interface separating two media is defined as the variation of the Gibbs free energy as a function of the area of the interface and is given by

$$\gamma = \left(\frac{\partial G}{\partial A}\right)_{T,P,n} \tag{2.33}$$

where G is the Gibbs free energy of the system, A is the area of the interface and T, P and n are the temperature, pressure and composition of the system. It is noticeable here that the higher the surface tension, more energy is required to increase the area of the interface. Therefore interfaces with a high surface tension have the tendency to be stiffer, while interfaces with low surface tension are softer.

An amphiphile is a molecule capable of modifying the surface tension of an interface thanks to its structure composed of hydrophilic and hydrophobic parts. An amphiphile lying at the air water interface will decrease its surface tension. The surface pressure Π of a monolayer is the difference between the modified surface tension and the initial surface tension of the air water interface as

$$\Pi = \gamma_0 - \gamma \tag{2.34}$$

where γ_0 and γ are the surface tensions in absence and in presence of the monolayer, respectively.

The surface pressure of a monolayer acts like a lateral osmotic pressure. When the monolayer is laterally compressed, the surface tension becomes higher. The graph 2.8 depicts the isotherm of a dipalmitoyl phosphatidylcholine (DPPC) at room temperature. At very low amphiphile

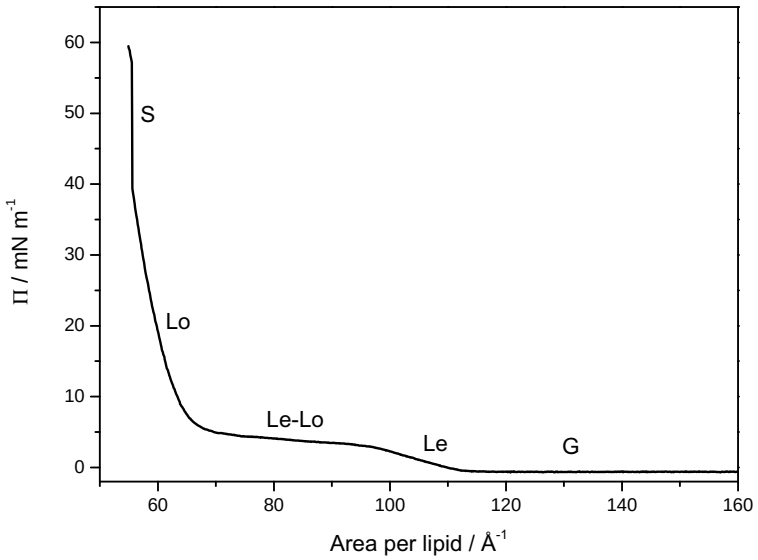

Figure 2.8: Surface pressure - Area isotherm of a DPPC monolayer at room temperature.

surface density, the surface pressure is zero, meaning that the monolayer does not affect the interfacial tension. The state of the monolayer is a gas phase (G) in two dimensions where the molecules are too far from each other to create an attractive interaction and thus increase the surface pressure. Under compression, the monolayer undergoes a phase transition and enters in the so-called liquid-expanded phase (Le). Upon a further compression, a plateau can occur which can correspond to the liquid expanded liquid ordered transition phase. In the liquid ordered phase (Lo), the curve becomes much steeper. The last step is the solid state phase in which the curve is the steepest (S).

Instrumentation

The Langmuir trough consists of one trough and two mobile barriers made of teflon, one pressure sensor made of paper and one dipper used to transfer the monolayer to a substrate. The Wilhelmy balance is a filter plate slightly immersed in water connected to a scale whose dimensions are shown in figure 2.9. The scale measures the three forces applied to the

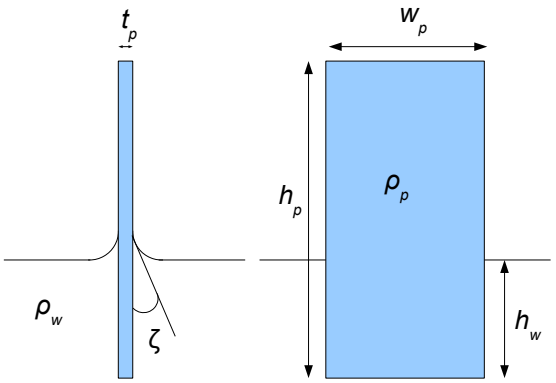

Figure 2.9: Scheme of the partially immersed paper plane used to measure the surface pressure.

plate. These forces come from the weight of the paper, the surface tension of the water and the buoyancy force.

The overall force felt by the sensor is:

$$F = \rho_p t_p w_p h_p - \rho_w t_p w_p h_w + 2(w_p + t_p)\gamma cos\zeta \tag{2.35}$$

where ρ_p and ρ_w are the mass density of the plate and the water, w_p, t_p, h_p are the width, thickness and height of the plate, h_w is the height of the sensor immersed in water, γ is the surface tension and ζ is the angle formed by the meniscus (see graph 2.9. The first term is simply the plate weight, the second term is the buoyancy and the third term comes from the surface tension.

Assuming that the level of water does not change and the paper plate is slightly immersed such as $cos\zeta \approx 1$ and $w_p >> t_p$, one can measure the surface pressure as

$$\Pi = \frac{\Delta F}{2w_p} \tag{2.36}$$

The trough models used in this work are Langmuir trough Nima 611 of an area of 300x200 mm^2 and composed of one mobile barrier and Langmuir trough 1212D an area of 680x200 mm^2 and composed of two mobile

barriers. The paper plates were Whatman CHR1 chromatography paper of wet perimeter 20.6 mm.

Langmuir-Blodgett and Langmuir-Schaefer (LB - LS) deposition

The Langmuir trough is also used for building up multilayers on a solid substrate. This can be done by alternatively dipping up and down the substrate perpendicularly oriented to the air-water interface.

First, the teflon through is cleaned by rubbing with dust-free paper soaked in chloroform. After, the trough is filled with ultra-pure water and emptied three times. Finally, the trough is filled with degassed ultra pure water. A compression is performed while checking the surface pressure. If the surface pressure increases, it indicates the presence of amphiphiles, meaning that the interface is contaminated.

If the surface is clean, the lipid monolayer can be spread at the air water interface. To do so, lipids are dissolved in chloroform and are very carefully spread at the interface by means of an Hamilton syringe. After a waiting time of 15 minutes in order to let chloroform evaporate, the barriers are compressed at a speed of 15 cm^2 per minute.

Once the desired surface pressure is reached, the Langmuir-Blodgett deposition or LB deposition can take place in order to deposit the first leaflet. By lifting the substrate up at a speed of 4 mm per minute, the lipid monolayer is transferred onto it as shown in figure 2.10.

Once the first leaflet is deposited on the substrate, the Langmuir-Schaefer or LS deposition can take place. This method is used to deposit the last leaflet of the lipid bilayer. The solid substrate is this time oriented parallel to the air water interface as shown in figure 2.10. It is very important to ensure that the block is perfectly parallel to the water surface, otherwise an edge of the block touching first the water will create a wave which could perturb the deposition. Once the deposition is done, the active surface block, i.e. the surface where the bilayer is deposited on, has to be kept immersed in the subphase and must be manipulated carefully in order to avoid bringing it in contact with air, which would damage the bilayer.

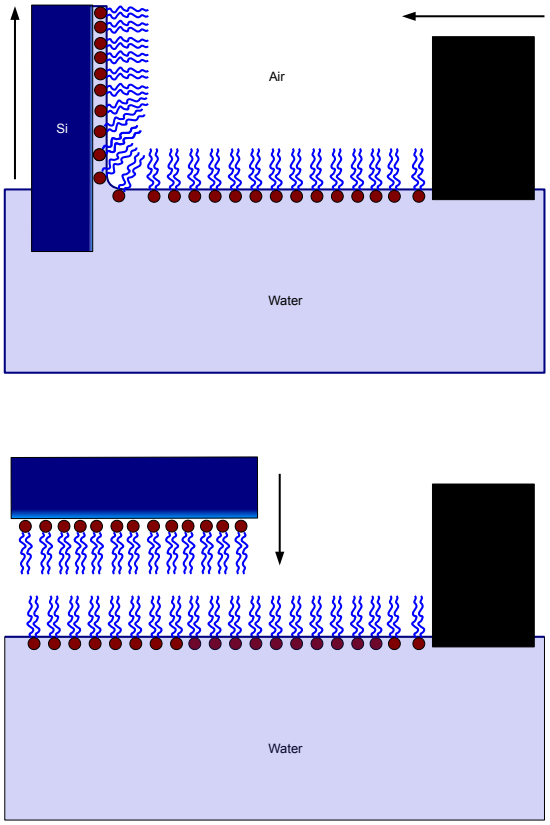

Figure 2.10: Scheme of Langmuir-Blodgett (up) and Langmuir-Schaefer (down) depositions onto a silicon substrate.

2.3.3 Vesicle fusion method

The vesicle fusion method was first mentioned in 1985 [45, 46]. This method is much more convenient from a practical point of view than the LB-LS deposition because it requires much less handling and the bilayer is formed *in situ*, allowing the characterization of the substrate. On the other hand, it is not possible to form floating bilayesr (i.e. a bilayer deposited over a supported bilayer) or asymmetric membranes. Before a neutron reflectivity experiment, Quartz Crystal Microbalance with Dissipation Monitoring (QCM-D) is an appropriate tool to find the condition to form a supported bilayer onto the substrate. This technique is very sensitive to mass ad-

sorption. It has the ability to measure the visco-elastic properties of the adsorbed layer, making the distinction between a supported bilayer and a vesicular layer possible.

Quartz crystal microbalance with dissipation monitoring: principles

Quartz Crystal Microbalance is a very versatile technique used to measure film thickness or mass during deposition onto a solid substrate made of a vibrating piezoelectric material. It has been used to study various interactions such as diffusion, adsorption and diffusion of gas within solid substrates under ultra high vacuum conditions. More recently, this technique has also been used to investigate visco-elastic properties of soft films at the solid liquid interface by measuring the energy dissipation associated with the fluidity of the film.

The technique consists of measuring the change in frequency of a vibrating piezoelectric material -generally made of quartz- arising from the adsorption of a compound onto it. Due to its piezoelectric properties, the quartz crystal can undergo three modes of deformation: transverse (shear), torsional (twist) and longitudinal. The technique used in this work only relies on the shear mode. Quartz is sandwiched between two gold electrodes and is subject to an alternating electric field passing through it at a resonant frequency.

The quartz oscillates in the fundamental shear mode at approximatively 35°from the crystalline axis. The vibrational motion results in the formation of a transverse acoustic wave which propagates within the crystal. The standing acoustic wavelength is exactly twice the thickness of the crystal and the crystal surfaces are the anti-nodes of the acoustic wave. When a thin film is deposited onto one side of the crystal and assuming that the velocity of the acoustic wave in the film material is the same as in the crystal, the change in frequency can be related to the film mass by the Sauerbrey equation

$$\Delta f = \frac{-2f_0^2}{A(\mu_q \rho_q)^{1/2}} \Delta m \tag{2.37}$$

where Δf is the frequency change, f_0 is the initial frequency, A is the

area of the quartz surface, μ_q and ρ_q are the shear modulus and the density of the quartz and Δm is the change of mass arising from the film deposition.

To get information on visco-elastic properties of the adsorbed film, another parameter called the Quality factor Q is required. The factor Q is the reciprocal of the dissipation factor, D, as

$$Q = \frac{1}{D} = \frac{E_{diss}}{2\pi E_{stored}} \tag{2.38}$$

where E_{diss} and E_{stored} are the dissipated and the stored energies during the deposition process, respectively.

The amplitude after shutting off the frequency generator decreases exponentially as

$$A(t) = A_0 e^{-t/\tau} sin(\omega t + \phi) \tag{2.39}$$

where $A(t)$ is the amplitude of the motion at the moment t, A_0 is the initial amplitude, τ is the decay time constant, ω is the angular frequency at resonance and ϕ is the phase. By fitting the amplitude decay behaviour after shutting off the electric field with this equation, τ can be estimated and D can be obtained thanks to the relation

$$D = \frac{2}{\omega\tau} \tag{2.40}$$

The QCM-D used for this thesis is the model E4 purchased from Q-Sense. The sensors used consist of a disk of quartz which contains gold-coating on both sides serving as electrodes to apply the voltage. A silicon surface is grafted on the active surface. The resonance frequency is 4.95 MHz±+ 50 kHz, the electrode is 40 μm thick, the diameter of the active surface is 14 mm and the surface roughness of the electrode is less than 3nm (RMS).

Unilamellar vesicle preparation

Lipids were previously stocked in chloroform : methanol solution (2:1) and kept in the freezer at -20°C. 0.5 mL of this lipid solution were transferred to a glass vial previously cleaned with abundant rinsing of water,

ethanol, acetone and a mixture of chloroform : methanol 2:1. The lipid solution was dried by a stream of nitrogen for 30 minutes until the formation of a thin lipid film around the glass wall and then suspended in a salt solution. After vigorous shaking, vesicles in suspension were tip-sonicated for 30 minutes by pulse of 5 seconds at frequency of 55 Hz in order to render them unilamellar.

Formation of a DPPC bilayer by vesicle fusion

Figure 2.11 shows the QCM-D measurement of DPPC vesicles adsorbed and fused onto a silicon substrate. In the first step (A) a decrease in frequency Δf of about -55 Hz is observed. This frequency shift is bigger than one expected for the deposition of a single planar supported bilayer. Moreover, the change in dissipation factor indicates that a much softer materiel than a single bilayer is being deposited. The changes in frequency and dissipation factor ΔD correspond to the whole vesicles adsorption. These vesicles contain water trapped inside, making the layer formed on the substrate heavier and softer than a lipid bilayer. During the step B, one can see that the frequency and dissipation shift pass by a minimum and a maximum, respectively. This corresponds to the rupture of the vesicle and release of the trapped water which makes the adsorbed layer lighter and more rigid. The system ends in the phase C, where the supported lipid bilayer is fully deposited and covered as reflecctd by a constant frequency and dissipation shift. The temperature of the vesicle solution has to be higher than the gel to fluid phase transition temperature because lipid vesicles have to be in the fluid phase to form a planar supported bilayer onto the substrate. In this case, the temperature of the solution was set to 45 °C, which is higher than the phase transition of DPPC.

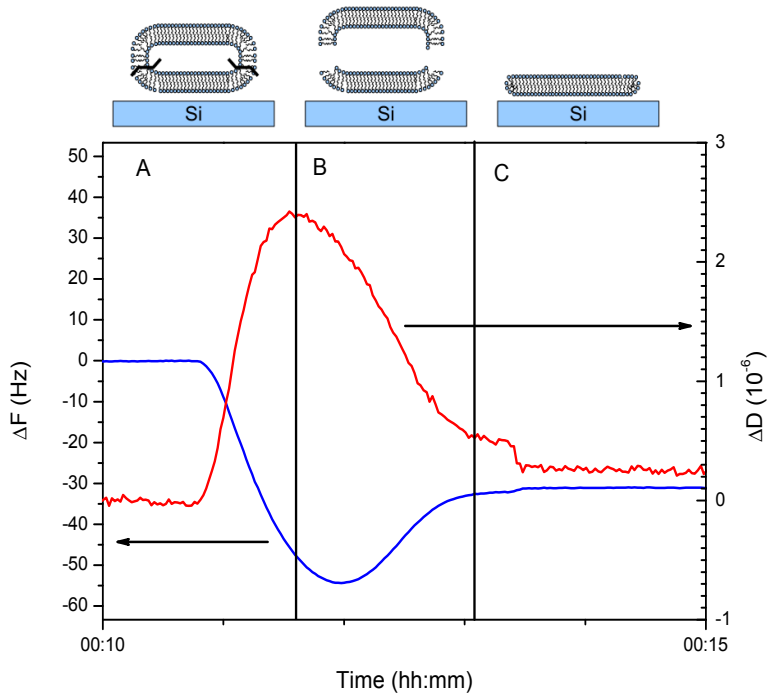

Figure 2.11: QCM-D frequency and dissipation data (ninth overtone) recorded during DPPC vesicle adsorption at 45°C for DPPC in NaCl 100 mM.

Chapter 3

Production and analysis of *Pichia pastoris* lipids

3.1 Introduction

Probing molecules using perdeuteration is an efficient method for the investigation of the structure and dynamics of biological systems by means of NMR, infrared spectroscopy or neutron scattering. The striking differences in scattering the cross sections of hydrogen- and deuterium-containing compounds makes neutron scattering a powerful tool in biophysical research in general and in membrane research in particular [20].

The development of protein deuteration facilities has greatly contributed to the current boosting of these activities. With respects to structural biology, neutron [57] and X-ray scattering techniques complement crystallographic studies that require high quality crystals of macromolecules. For example, small angle neutron and X-ray scattering are widely used for the study of biomolecules and their assemblies in solution, including those difficult to crystallize. In parallel, neutron and X-ray reflectometry are increasingly used to characterize planar surfaces including model lipid membranes [58, 59].

Bilayers made of synthetic lipids have been widely investigated to understand properties like phase behaviour, water permeability and changes induced by membrane proteins [60–62]. While these studies are useful to

understand important aspects of cell membrane behaviour, they also give clues to the complexity of real systems and the difficulty of relating model constructs to the actual behaviour of membranes.

Analysis of the membrane composition is a pre-requisite for using isotopically labelled membranes, as analysis requires the use of chemically identical preparations. Separation of lipids into the constituent lipid classes further allows the effects of lipid composition on membrane properties and response to proteins, peptides and pharmaceuticals to be investigated.

Commercially available deuterated lipids consist of either fully saturated or mono-unsaturated phospholipids. While synthetic routes to obtain unsaturated chains are not trivial, it is possible to obtain naturally produced perdeuterated unsaturated lipids by extracting them from living organisms as long as these organisms are capable to grow in a deuterated medium allowing the biosynthesis and efficient use of deuterated organic building blocks.

The methylotrophic yeast *Pichia pastoris* has been widely used as an expression system to produce biological compounds [63, 64]. Its ability to grow in a fully deuterated medium has made it an ideal system for the synthesis of perdeuterated macro molecules that are very difficult to synthesize chemically [65–67]. Few studies report the role of deuterated environment on *P. pastoris* lipid biosynthesis [66–68], compared to available data on hydrogenated lipid metabolism and composition [69–71].

The detailed pathways of fatty acid biosynthesis (including elongation and desaturation) and lipid regulation have however been investigated in the model yeast *Saccharomyces cerevisiae* [72–74].

With the aim to use naturally deuterated membranes for biophysical studies, it is important to check that lipids produced by *P. pastoris* cells in deuterated environment are identical to those produced in hydrogenated one. This work provides analytical information that shall be essential to comprehend possible differences in results on the structure or dynamics of hydrogenated and deuterated membranes.

In the first part of this chapter, the protocols used to quantify glycerphospholipid and to separate polar from apolar lipids are described. The quantitative analysis of the main glycerophospholipids in deuterated and

hydrogenated yeast at different growth temperature is reported. A protocol used to separate d-PC and d-PE by means of flash chromatography was also elaborated in order to be able to use them for future neutron scattering experiments. A qualitative analysis of sphingolipids and more in general ceramides is provided in the third section. Even if the analysis was done qualitatively, it is obvious that the amount of sphingolipids is very low compared to that of glycerophospholipids since the intensity of the spots corresponding to sphingolipids are much weaker. Eventually, the headgroup composition and fatty acid distribution as function of the isotopic and thermal changes of the growth culture are discussed.

3.2 Sample preparation

3.2.1 Strain culture conditions

Pichia pastoris GS115 HSA (Invitrogen) cells were grown at 30°C in 10ml of BMGY medium 10 g/l yeast extract, 20 g/l peptone, 5.96g/l KH_2PO_4, 1.07g/l K_2HPO_4, 13,4 g/l yeast nitrogen base with ammonium sulfate without amino acids, 4 mg/l biotin, 10 g/l glycerol) in a 100 ml Erlenmeyer flask (Corning) using vent caps for continuous gas exchange with shaking at 250 rpm. After about 4 days 1 ml of this preculture was diluted into 100 ml of minimum medium ((38.1 g/l H_3PO_4, 0.93 g/l $MgSO_4$, 4.13 g/l KOH, 20 g/l glycerol, 0.4 mg/l biotin, 40 mg/l histidine, 26 mg/l cupric sulphate pentahydrate, 0.35 mg/l sodium iodide, 13 mg/l manganese sulphate monohydrate, 0.87 mg/l sodium molybdate dehydrate, 0.09 mg/l boric acid, 2.17 mg/l cobalt chloride, 87 mg/l zinc chloride, 0.28 g/l ferrous sulphate heptahydrate, 87 mg/l biotin, 40 mg/l sulphuric acid; the pH was a adjusted to 6.0 using NH_4OH) and incubated at 30°C for 2-3 days with shaking at 250 rpm.

The composition of PTM1 was the following: cupric sulphate pentahydrate 6 g/l, sodium iodide 0.08 g/l, manganese sulphate monohydrate 3.0 g/l, sodium molybdate dehydrate 0.2g/l, boric acid 0.02 g/l, cobalt chloride 0.5 g/l, zinc chloride 20.0 g/l, ferrous sulphate heptahydrate 65.0 g/l, biotin 0.2 g/l, sulphuric acid, 5 ml/l. For the adaptation of perdeuter-

ated *Pichia pastoris*, 1ml of the culture in minimum medium was diluted into 100ml of perdeuterated BSM and incubated at 30°C for 5-6 days. The deuterated medium was prepared in the following way: 1l liter of hydrogenated BSM without glycerol is flash evaporated , the powder resuspended in 250ml of 99.85% D_2O (Euriso-top) and flash evaporated again. This process was repeated twice to get rid of traces of hydrogens. Finally the powder was resuspended in 1l D_2O (purity >99.9%, from the Institut Laue-Langevin, France) containing 20g d8-glycerol (Euriso-top). The deuterated culture was diluted again in d-minimal medium and grown for 2-3 days and used as inoculum for the final deuterated culture. 1ml of each H- or D-pre-culture was taken to inoculate 150 ml of H-BSM and deuteraded BSM and incubated at 18°C or 30°C. The initial OD was about 0.3 for all the cultures.

P. pastoris cells were harvested by centrifugation in the early exponential phase, at an optical density at 600 nm (OD_{600}) of 20 for the analysis of phospholipids. They were harvested in the late exponential phase ($OD_{600} \geq 80$) for the analysis of sphingolipids and for the neutron reflectometry experiments presented in the next chapter.

3.2.2 Protocol for lipids extraction and phospholipids analysis

Lipids were extracted from freshly harvested *P. pastoris* cells, according to a modified Folch method. The modification consists of boiing freeze-dried cells in ethanol for five minutes as prior step in order to denaturate endogemic enzymes like phospholipases capable of damaging glycerolipids. The rest of the extraction followed the Folch procedure [75].

Lipids were separated by two dimensional thin layer chromatography (2D-TLC) using 20 cm x 20 cm glass plates coated with silica (silica gel 60, Merck). The first chromatographic direction was achieved in chloroform - methanol - water (65:25:4, v/v), then the TLC plate was dried thoroughly under a stream of argon, and the second chromatographic direction was performed in chloroform : acetone : methanol : acetic acid : water (50:20:10:10:5, v/v). Lipids were visualized under ultraviolet (UV) light

after staining with 8-anilino-1-naphthalenesulfonic acid, 2% in methanol, and identified by comparison with standards. A typical TLC plate is shown in figure 3.1, where we can clearly see the main spots associated to phosphatidylcholine (PC), posphatidylethanolamine (PE), phosphatidylserine (PS), phosphatidylinositol (PI), phosphatidylglycerol (PG) and cardiolipin (CL).

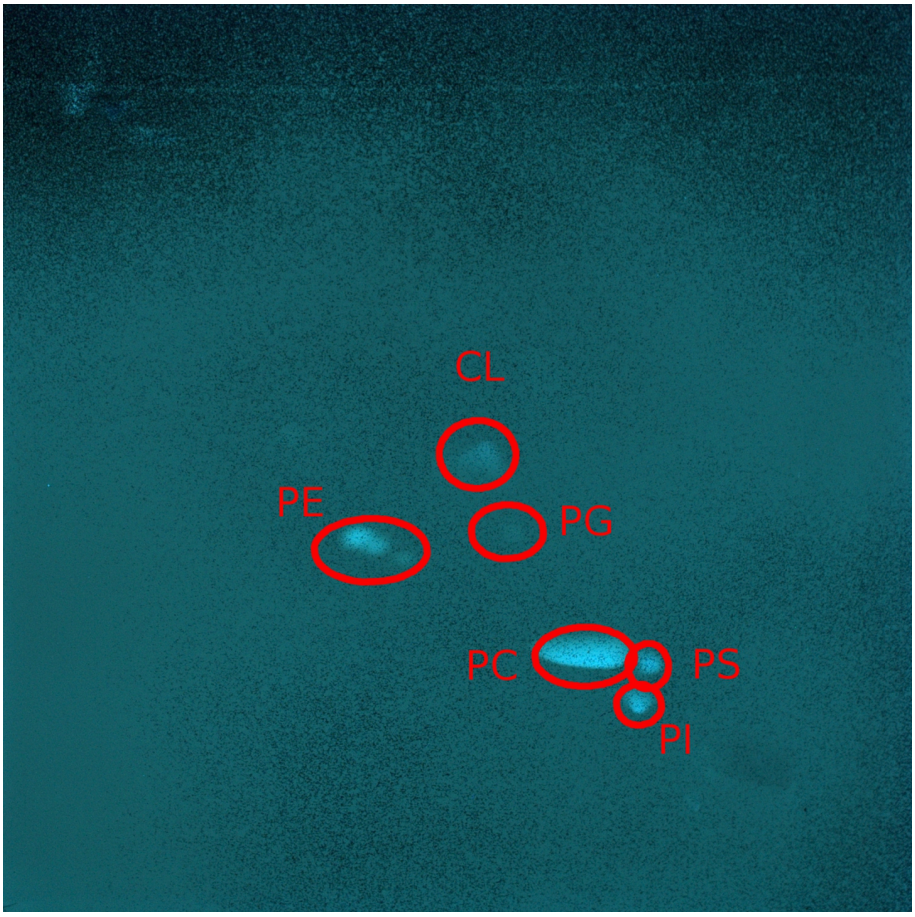

Figure 3.1: 2D TLC used to separate glycerophospholipids. Sovent used: chloroform:methanol:water (65:25:4, v/v) for the first direction, chloroform:acetone:methanol:acetic acid:water (50:20:10:10:5, v/v) for the second direction. Lipids were visualized under ultraviolet (UV) light after staining with 8-anilino-1-naphthalenesulfonic acid.

Lipid spots were scrapped of the TLC plates separately and known

amounts of a C21:0 control fatty acid (a linear chain of 21 carbons with 0 double bond) were added to each lipid spot. The acyls esterified on the extracted natural glycerolipids and the control C21:0 fatty acids were methylated by a methanolysis procedure by incubation with 2.5% H_2SO_4 in pure methanol (3 mL total volume) during 1 h at 100°C in a sealed glass vial. The reaction was stopped by addition of 3 ml of water and 3 ml of hexane. Following the formation of a biphasic system, the upper phase was collected, dried under a stream of argon, resuspended in pure hexane and then analyzed by gas chromatography (Perkin Elmer) on a BPX70 (SGE) column. Fatty acid methyl esters (FAMEs) retention times were compared with those of hydrogenated standards FAMEs (Sigma) and deuterated FAMEs. Standard deuterated C16:0 and C18:0 FAMEs were obtained by methanolysis respectively of 1,2-dipalmitoyl(d62)-sn-glycero-3-phosphocholine and 1,2-distearoyl(d70)-sn-glycero-3-phosphocholine (Avanti).

3.2.3 Separation of lipids batch in polar and apolar fraction

The separation of the total lipid extract into apolar and polar fractions is important for the biophysical investigation of the interaction of amphotericin B with different reconstituted membranes described in the following chapter. The procedure is described here since the current chapter deals with all the biological extraction protocols.

The total extract (dried mass of about 1g) is separated a first time by a flash chromatography. 500 mg of silica (mesh size of 0.04-0.063 mm, Roth, France) are used for a separation. The first eluent used is composed of chloroform - acetic acid (100:1, v/v). 20 mL of the eluent are passed through the column to obtain the lipid called "apolar fraction". This fraction contains mainly the triglycerides, free fatty acids and sterols. 20 mL of the second eluent, composed of methanol only, are passed through the column. It elutes the called "polar fraction" which contains mostly glycerophospholipid and sphingolipids.

Two TLC's are carried out to ensure there is no cross contamination between the two fractions.

The first one is used to visualize the content of apolar lipids in the fractions. The eluent used for the TLC is a mixture of hexane - diethylether - acetic acid (70:30:1 v/v/v). The reagent used to visualize the spots is iodine vapor. The front ratios of the apolar fraction spots are 0.92, 0.85, 0.61, 0.31 and 0.23. The second TLC is used to evaluate the amount of phosholipid content. The eluant is a mixture of chloroform - methanol - water (65:25:4 v/v/v). The front ratio of apolar fraction spot is 0.86. The front ratios of the polar fraction spots are 0.56, 0.44, 0.21 and 0.17. The spots were visualized with phosphomolybdic acid.

The apolar fraction is then purified by means of normal phase HPLC (250 X 8 mm, Eurospher 100 Å Si, Knauer, France). The eluant used is a mixture of hexane - isopropanol (100:1, v/v) and is passed through the column at a flow rate of 2 mL min^{-1}. The compounds are analysed by means of a UV detector at a wavelength of 206 nm. The sterols come out of the column from the 30th minute. This procedure is based on the protocol elaborated by Hamilton et al.[76]. A typical chromatogram is shown in figure 3.2 where we can see the first peaks appearing between 3 and 15 minutes. These peaks correspond to the most apolar lipids such as triglycerides or free fatty acids. The peak, coming out at around 30 minutes (circled in figure 3.2) corresponds to the eluted sterols. A TLC in hexane - diethylether - acetic acid (70:30:1) is performed with the sterol fraction in presence of an ergosterol standard to verify that their front ratios match.

3.3 Results

3.3.1 Quantitative glycerophospholipid analysis

Growth curves

Figure 3.3 shows the growth curves of yeast cells at 18°C and 30°C in hydrogenated (H) and deuterated (D) media (top and bottom graph, respectively). In H medium, the cells starts to grow immediately at 30°C, whereas at 18°C there is a there is latency time before the cells start growing. This latency time is called lag phase. It lasts two days when hydro-

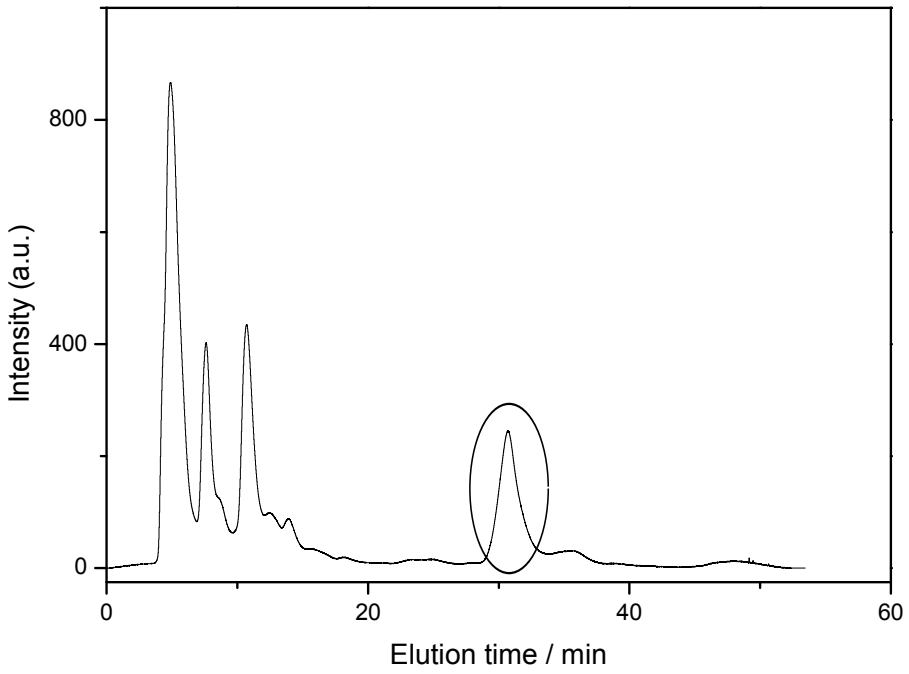

Figure 3.2: Chromatogram used for the purification of sterol. The detector used is a UV absorber at 206 nm. The sterol peak is circled for clarity.

genated cells are grown at 18°C. In D medium, the lag phase lasts two days at 30°C and 5 days at 18°C. In every case, the cell growth is not limited by deuteration and by temperature since the growth rate is similar. For comparisons, cells are collected at an optical density at 600 nm (OD_{600}) of 20, corresponding to the beginning of the exponential phase.

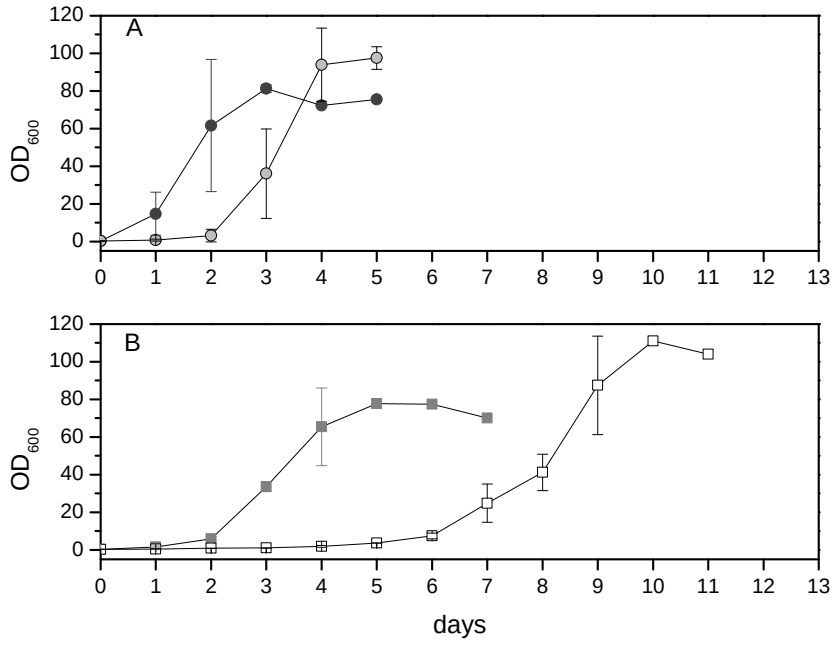

Figure 3.3: (A) Growth of *Pichia pastoris* cells in a hydrogenated medium at 30°C (dark grey circle) and 18°C (light grey circle). (B) Growth of P. pastoris cells in a deuterated medium at 30°C (grey square) and 18°C (white square).

Influence of deuterated environment on phospholipid class and total fatty acid distribution

the phospholipid composition of *P. pastoris* cells grown in hydrogenated medium with glycerol as a carbon source is consistent with previous reports [71]. The most commonly found head-group classes were present, namely PC, phosphatidylcholine; PE, phosphatidylethanolamine; PI, phosphatidylinositol; PS, phosphatidylserine; PG, phosphatidylglycerol; CL,

cardiolipin. No significant change in phospholipid class composition was observed when cells were grown in deuterated environment (3.4, left). It can be concluded that the various lipid class metabolic pathways were not significantly affected by the isotopic conditions of the growth medium.

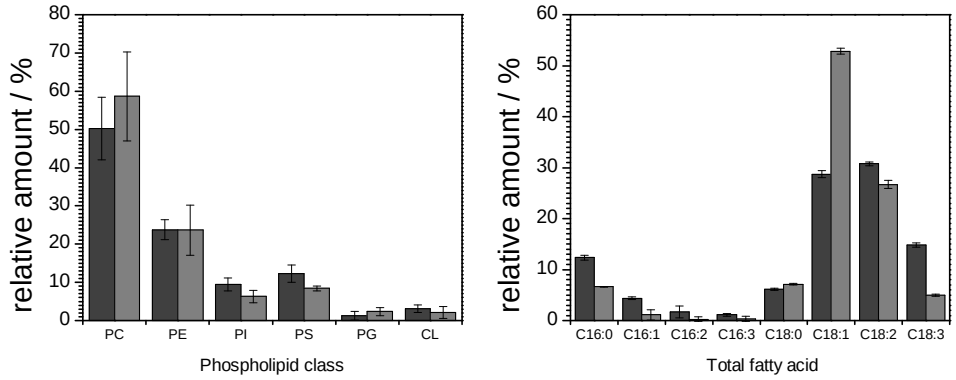

Figure 3.4: Phospholipid composition (left) and total fatty acid distribution (right) of Pichia pastoris cells grown in a hydrogenated medium (dark grey) and in a deuterated environment (grey) at 30°C. Error bars represent standard deviations (n=3).

It is noticeable that the deuterated growth medium has an influence on the acyl carbon chains, in terms of lengths and unsaturation levels (figure 3.4, right). The most obvious feature is the remarkable increase of C18:1 chains. The ratio of C16/C18 fatty acids is also affected whether cells are grown in a hydrogenated or deuterated environment. This ratio is 0.24 ± 0.01 in H-lipids and 0.11 ± 0.02 in D lipids (see table 3.1). The deuterated environment might influence the activity level of the fatty acid synthase of type I (FAS I) and the thioesterase(s) that can release C16- or C18-acyls. Although it is difficult to assess whether the effect is due to a decrease of the corresponding gene expressions, to a folding default of the enzymes, or to an alteration of the enzymatic activities in presence of deuterated substrates, it is reasonable to propose that the enzyme specificity for their substrates might be sensitive to the presence of deuterium in place of hydrogen. The ratio of unsaturated/saturated fatty acids (UFA/SFA) is 4.42

Table 3.1: Table 1. Ratio (upper part) of C16/C18 fatty acids and (lower part) of unsaturated/saturated fatty acid (UFA/SFA) when *Pichia pastoris* cells were grown in hydrogenated (H) and deuterated (D) media at 18 and 30°C.

	Total	PC	PE	PI	PS
C16/C18					
H 30°C	0.24 ± 0.01	0.23 ± 0.01	0.27 ± 0.01	0.53 ± 0.02	0.67 ± 0.02
H 18°C	0.14 ± 0.03	0.12 ± 0.01	0.20 ± 0.03	0.43 ± 0.08	0.52 ± 0.02
D 30°C	0.11 ± 0.02	0.05 ± 0.01	0.18 ± 0.02	0.38 ± 0.03	0.53 ± 0.03
D 18°C	0.18 ± 0.02	0.09 ± 0.01	0.27 ± 0.02	0.48 ± 0.03	0.65 ± 0.02
UFA/SFA					
H 30°C	4.42 ± 0.20	6.34 ± 0.20	3.60 ± 0.10	1.52 ± 0.10	1.32 ± 0.03
H 18°C	5.70 ± 0.22	25.89 ± 4.86	5.14 ± 0.87	1.92 ± 0.45	1.52 ± 0.05
D 30°C	6.28 ± 0.13	17.16 ± 1.23	5.56 ± 0.17	2.08 ± 0.32	1.69 ± 0.08
D 18°C	6.19 ± 0.02	15.39 ± 1.41	4.14 ± 0.21	2.17 ± 0.18	1.88 ± 0.03

± 0.20 in a hydrogenated medium and 6.28 ± 0.28 in a deuterated medium (table 3.1). This change mainly reflects the enhanced production of C18:1 in deuterated cells (see figure 3.4). It is worth noting that the production of deuterated C18:3 is highly inhibited in deuterated medium while that of C18:2 stays constant.

Influence of temperature on total fatty acid production

It has been observed that yeasts can regulate the fatty acid distribution to maintain membrane fluidity by increasing the production of polyunsaturated fatty acids (PUFA) if the temperature is lowered during cultivation [77]. To improve deuterated PUFA production, we investigated this physiological response by decreasing the growth temperature to 18°C instead of 30°C.

In hydrogenated conditions, the proportion of polyunsaturated fatty acids increased concomitantly with the C18/C16 ratio. This result is consistent with previous studies [77].

Deuterated yeast cells also increased their production of polyunsatu-

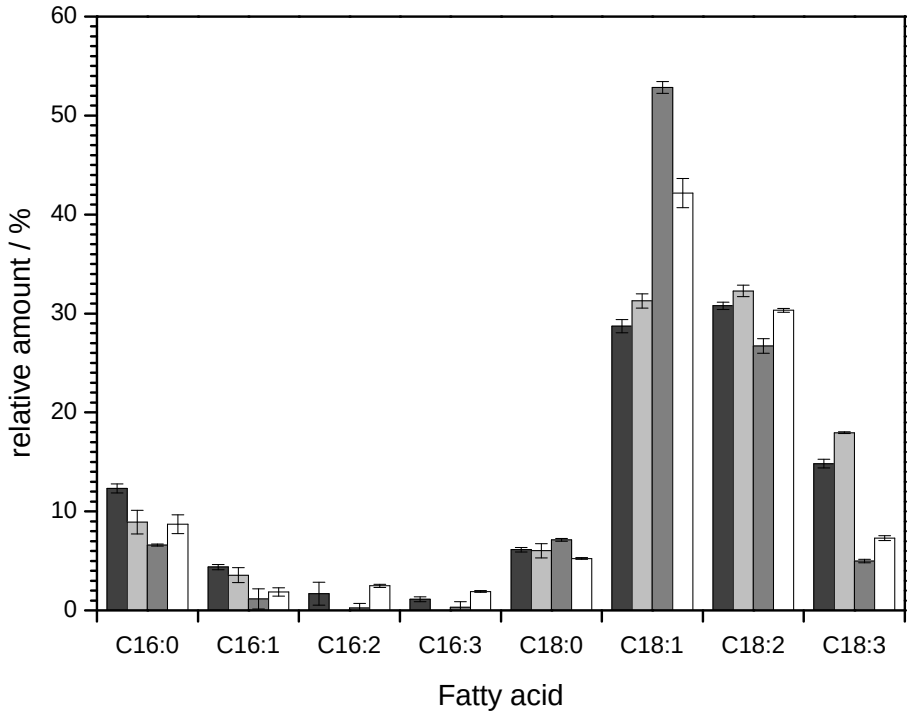

Figure 3.5: Total fatty acid distribution in Pichia pastoris cells grown in hydrogenated environment at 30°C (dark grey) and 18°C (light grey) and in deuterated environment at 30°C (grey) and 18°C (white). Error bars represent standard deviations from three independent measurements.

rated fatty acid when grown at 18°C, though less than the corresponding hydrogenated control (figure 3.5). The proportion of deuterated C18:1 decreased from 53 % at 30°C to 43 % at 18°C, while the proportion of deuterated fatty acid C18:2 increased from 27 % to 30 % and fatty acid C18:3 from 5 % to 7 %. The production of C18:1, C18:2 and C18:3 all increased in hydrogenated yeast when lowering growth temperature.

The ratio C16/C18 of deuterated yeast extracts at 30°C was 0.11 ± 0.02 while it was 0.18 ± 0.02 at 18°C. Surprisingly, this change was opposite in the hydrogenated batch, from 0.24 ± 0.01 at 30°C to 0.14 ± 0.02 at 18°C (table 3.1).

Fatty acid analysis of the different classes of phospholipids

Some general patterns found in the global composition of acyls esterified to all glycerolipids (here called total fatty acids) are also present in individual phospholipid fatty acid distributions.

- At 30°C in deuterated conditions, C18:1 is always the main fatty acid in all lipid classes.
- Deuterated C18:3 synthesis is always inhibited in comparison to C18:3 generated in a hydrogenated medium.
- Lowering the temperature enhances the production of deuterated polyunsaturated fatty acids (PUFA), but not enough to reach the same amount of PUFA in hydrogenated yeast.
- The C16/C18 ratio of deuterated fatty acids increases while the C16/C18 ratio of hydrogenated fatty acids decreases by lowering the growth culture temperature (see table 3.1).

If we examine more carefully the fatty acid distribution in each class of phospholipids, we can highlight more subtle differences that might reflect some specific effects on enzymatic activities when using deuterated substrates (figure 3.6).

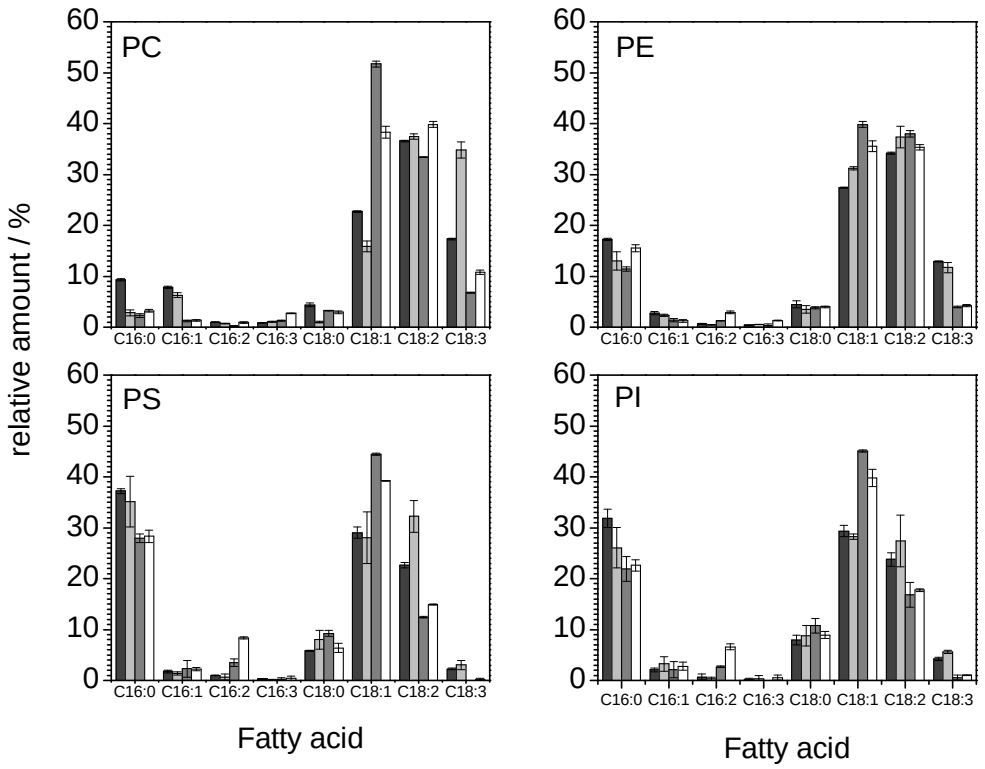

Figure 3.6: Total fatty acid distribution in Pichia pastoris cells grown in a hydrogenated environment at 30°C (dark grey) and 18°C (light grey) and in a deuterated environment at 30°C (grey) and 18°C (white). Error bars represent standard deviations (n=3).

In PC, the ratio of hydrogenated C16/C18 decreases when the growth medium is cooled down, whereas the opposite trend is observed in deuterated cells. The UFA/SFA ratio of hydrogenated PC is much higher than that of deuterated PC at 30°C (table 3.1). When the growth medium is cooled down from 30°C to 18°C, the UFA/SFA ratio in hydrogenated media dramatically increases from 6.34 ± 0.20 at 30°C to 25.89 ± 4.86 at 18°C. This very high ratio comes from the fact that, in PC, almost neither hydrogenated C16:0 nor C18:0 are present at 18°C. In deuterated PC, the growth temperature does not affect the ratio UFA/SFA.

PE exhibits less variation in function of the isotopic or thermal conditions compared to the other phospholipids. When lowering growth temperature, the C16/C18 ratio decreases in hydrogenated cells and increases in deuterated cells and the UFA/SFA ratio increases in hydrogenated cells and decreases in deuterated cells. However, these differences are minor and the C16/C18 and SFA/UFA ratios are roughly identical at distinct growth temperatures and in different isotopic conditions. The most remarkable feature is the inhibition of the synthesis of C18:3 in the deuterated culture, which is a common feature observed in all other phospholipids.

PS and PI have a very similar fatty acid distribution. In deuterated yeast, the amounts of C16:0 and C18:2 are reduced and C18:3 almost completely vanished. However, the production of C16:2 is triggered by lowering growth temperature.

PC and PE purification

The separation of phospholipids was done by flash column chromatography. The column had a diameter of 4 mm and a length of 15 cm. It was filled with silica gel (about 24 mg) with a mesh dimension of 0.040-0.063 mm. The column was then poured with a solvent mixture constituted of chloroform-methanol-isopropanol-water (55:10:20:3). This solvent mixture was the first eluent used to separate phospholipids. A nitrogen flow was applied at the beginning of the column in order to "push" the eluent through the column. The column was well equilibrated once the silica gel

Table 3.2: Mass of the different collected fractions eluted by flash column chromatography.

Specie	Fractions	Mass (mg)	Mass ratio (%)
Freeze dried deuterated yeast cell	-	600	100
d-PE	9-19	1.1	0.2
Unkown	35-59	1.3	0.2
d-PC	70-100	2.8	0.5
Unknown	103-130	1.1	0.2

was transparent.

All the organic fractions were collected and pooled together. From about 600 mg of freeze-dried deuterated yeast cells, 10.4 mg of lipids from all the organic fractions were extracted. This fraction was mixed with about 20 mg of silica gel in acetone and dried again. This was done to have the lipid in powder form instead of a thin film on the glass flask, making it easier to insert the lipids into the column. The powder shaped lipids and 83 mL of eluent were inserted in the column.

Lipids were eluted at a flow rate of approximatively 500 μL/minute. A fraction collector was connected to the exit of the column. The fractions contained around 0.5 mL of eluent. After the 70th fraction, the eluent was replaced by 83 mL of a mix of chloroform-methanol-isopropanol-water (55:15:12:3) until the 150th fraction (figure 3.7).

A first component came out in the 4th to the 7th fractions, but it did not seem to belong to the lipid extract. It could be related to a component previously extracted and present in the collector tubing.

However, PE was obviously eluted from the 9th to the 19th fractions (see figure 3.7). Another component appeared from fractions 35 to 59, although it is difficult to see it on the scanned TLC. PC was collected from fractions 70 to 100 and two last spots eluted at the same time, from fractions 103 to 130 with a R_F lower than the one of PC which are likely to correspond to PS and PI since they are the third and fourth main glycerolipid components. The masses of all the fractions and all the mass ratios are listed in table 3.2.

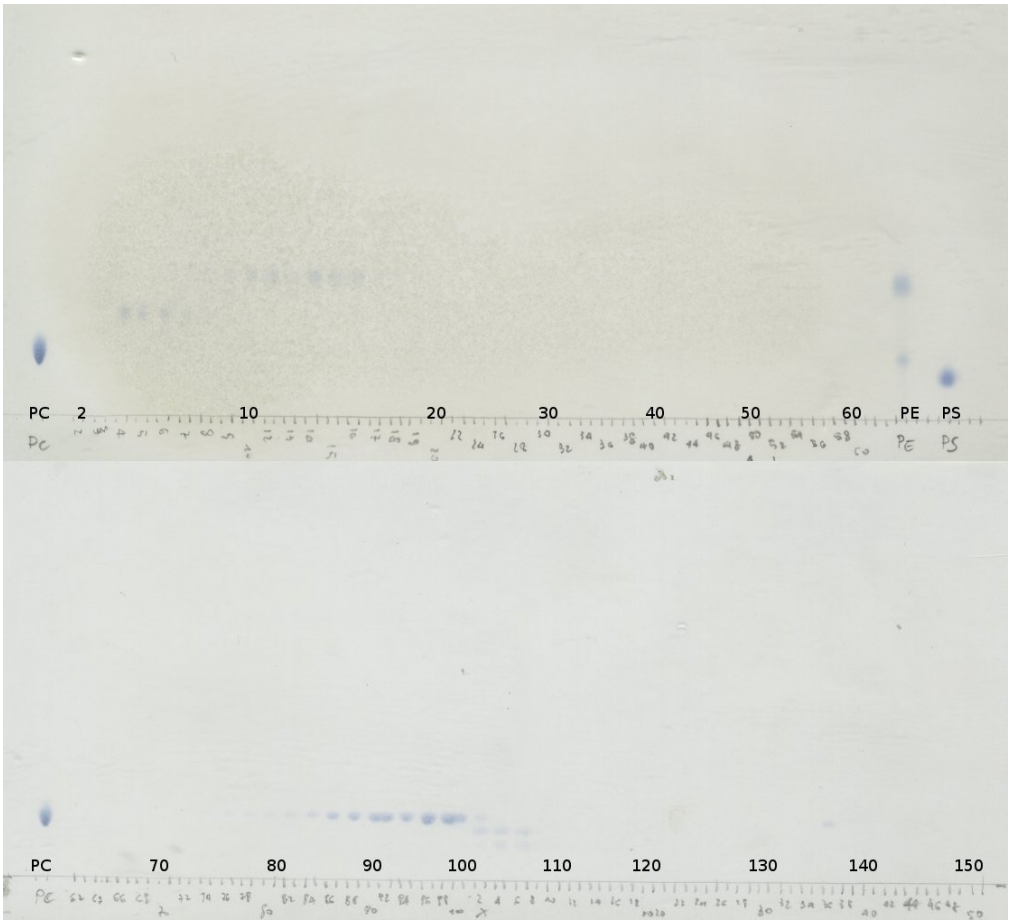

Figure 3.7: TLC analysis of the collected fractions from the flash column separation. Eluent used: chloroform-methanol-$CaCl_2$ 0.2 % (60:35:8) (up) and chloroform-methanol-isopropanol-water (55:15:12:3) (down). Phosphorous reagent is used for spots detection.

3.3.2 Qualitative sphingolipid analysis

Before alkaline methanolysis

A thin layer chromatography (TLC) test was carried out in presence of sphingomyelin as standard and it is obvious that this compound is absent in the lipid extract because there are no spots matching the standard spot, as shown in figure 3.8. The big visible spots can be attributed to the glycerophospholipids quantified in the previous section.

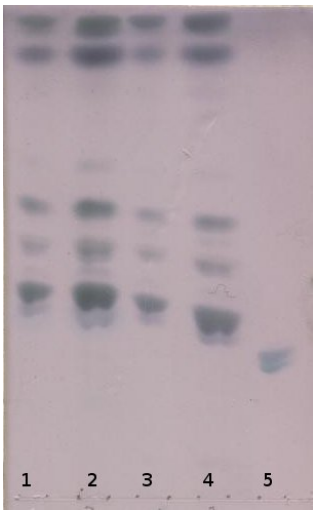

Figure 3.8: Normal phase TLC with hydrogenated and deuterated yeast lipid extracts. Lane attribution: 1 and 2: hydrogenated yeast lipid extract (1 and 3 μL, respectively), 3 and 4: deuterated yeast lipid extract (1 and 3 μL, respectively), 5: sphingomyelin standard. Eluent used: chloroform-methanol-$CaCl_2$ 0.2 % (60:35:8). Sulfuric acid was sprayed to detect the spots.

After alkaline methanolysis

According to the TLC shown in figure 3.8, the big spots revealed the glycerophospholipids which overwhelm the sphingolipids, making their detection very challenging. This is why the lipid batches had to undergo an alkaline methanolysis. Since sphingolipids do not contain ester bounds, they are not affected by the methanolysis.

To do so, 100 μL from H and D batch were taken to be methanolysed. The solution was dried and suspended in 100 μL of chloroform. After vortexing and sonication, 100 μL of 0.6 N NaOH in methanol was added to the solution. The solution was heated to 37°C for 3 hours then left at room temperature overnight. Then 120 μL of HCl in methanol were added to the solution to stop the reaction. By adding 180 μL of methanol, 700 μL of chloform and 170 μL of water, a biphasic system was formed. The system was vortexed, mixed for 10 minutes then centrifugated at 12000 rpm for 10 minutes. The lower phase contained the sphingolipids.

Before analysing the sphingolipid composition, one had to be sure that all the glycerolipids were methanolysed. Therefore the system was analysed by TLC with the same solvents system as shown in figure 3.8. It is clear that the the big spots supposedly corresponding to glycerophospholipids disappeared (see figure 3.9), meaning that the methanolysis was successful eliminating glycerolipids.

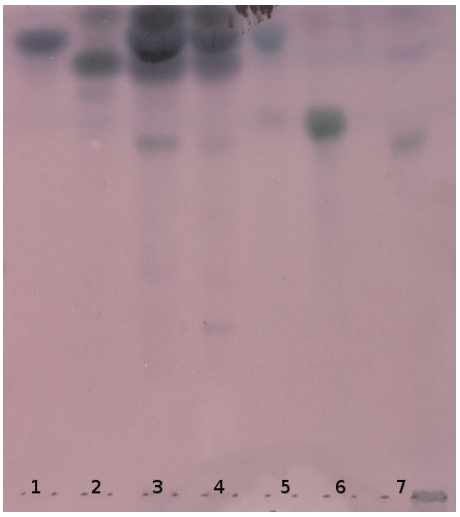

Figure 3.9: Analysis of the lipid composition in the aqueous phase following the methanolysis. Lanes attribution: 1: ergosterol, 2: oleic acid standard, 3: hydrogenated yeast, 4: deuterated yeast, 5: ceramide C18 standard, 6: glucosylceramide standard, 7: galactosylceramide standard. Eluents used: chloroform-methanol-$CaCl_2$ 0.2 % (60:35:8). Anisaldehyde was used as reagent.

Glycosphingolipids analysis

The methanolysed batches were then suspended in 50 μL of chloroform-methanol 2:1. A TLC was run in chloroform-methanol-water (110:40:6) in order to detect the presence of various glycosphinglipids (see figure 3.10). According to this TLC, it seems that both yeast extracts contained ceramide and galactosylceramide. To have a better discrimination between glucosylceramide and galactosylceramide, another TLC was run. Before sptting on the lipids, the plate was sprayed by a solution of sodium tetraborosilicate (12g in 100 mL H_2O mixed in methanol (1:3 v/v)) and heated at 100°C for one hour. After having inseminated lipids, the solvents used as eluent were chloroform-methanol-NH_3 2N (70:30:3). Aniline was used as reagent. The identification of the glycosphingolipid is not obvious, the spot is between the two standards of galactosylceramide and glucosylceramide (figure 3.11).

According to Ternes & al. [78], *Pichia pastoris* cells synthesize a slightly modified glucosylceramide, which contains an alpha-hydroxyl group on the fatty acid chain (see figure 3.12). This modification changes the polarity of this sphingolipid, which explains the shift in front ratio with respect to the glucosylceramide standards. However, some references [78, 79], also mention the presence of inositol phosphoceramides in *Pichia pastoris* cells, but we did not investigate this compound in the methanolysed batches.

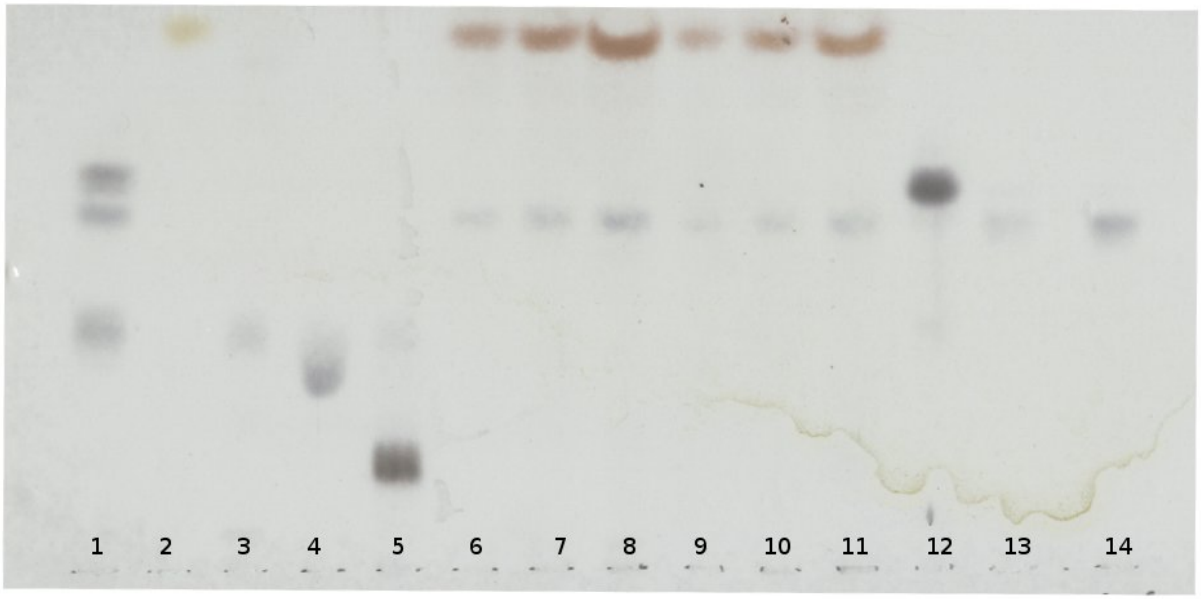

Figure 3.10: Normal phase TLC with hydrogenated and deuterated yeast. Lanes attribution: 1: mix of glycolipids, 2: ceramide, 3: lactosylceramide, 4: sulfatide, 5: trisosylceramide, 6, 7, 8: hydrogenated yeast (3, 5 and 10 μL, respectively), 9, 10, 11: deuterated yeast (3, 5 and 10 μL, respectively), 12: glucosylceramide, 13: galactosylceramide, 14: galactosylceramide (from a different batch). Eluent used: chloroform-methanol-water (110:40:6). Aniline was used as reagent.

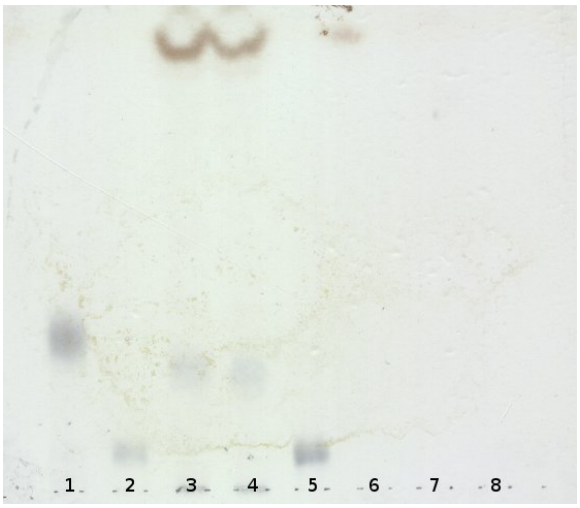

Figure 3.11: Sphingolipid analysis on a plate priorly treated by tetraborosilicate. Lanes attribution: 1: glucosylceramide, 2: galactosylceramide, 3: hydrogenated yeast lipids, 4: deuterated yeast lipids, 5: sulfatide, 6: ergosterol, 7: palmitic acid 8: oleci acid. Eluent used: chloroform-methanol-NH_3 2N (70:30:3). Anilin was used as reagent.

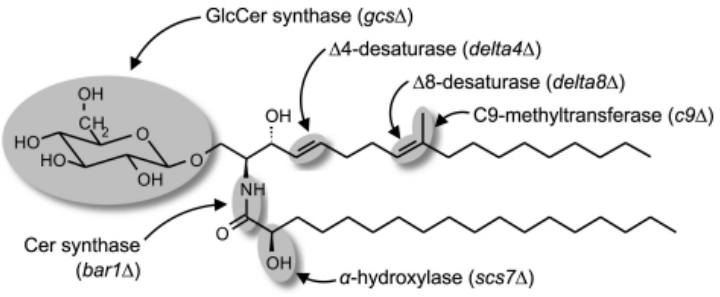

Figure 3.12: Structure of the glucosylceramide found in yeast [78].

Ceramide analysis

To detect ceramides, the methanolysed batches were applied on TLC and eluted by a solvent mixture composed of hexane-chloroforom-acetone-acetic acid (20:70:20:4). This solvent mixture is appropriate for ceramide separation as a function of the fatty acid chain length. Figure 3.13 shows the profile of different ceramides with various chain length used as standards and H and D yeast methanolized lipid extracts. Standards showed that the big spots located on the top of the plate were not ceramides. By reacting with anysaldehyde, ceramides form a compound which has a colour different from sphingolipids. Unfortunately, the big spots spread along the path, which makes the lower spot colour more challenging to determine. To resolve this problem, 2 dimension TLC's were done (see figure 3.14 and 3.15). The first run elutes only the yeast extract. Afterwards, the standards are added on one side of the plate before the second run. This method allows a better visualization of the colour of the spots corresponding to ceramides. Although they did not elute as the standards, the colour of these spots is the same as that of ceramide standards.

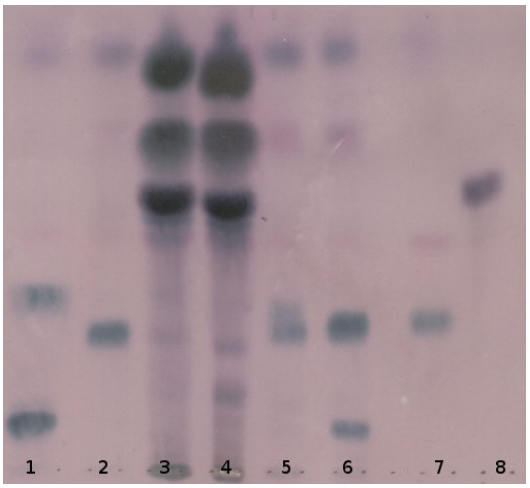

Figure 3.13: Ceramide analysis by TLC. Lanes attribution: 1: ceramide C2 and C24 standards, 2: ceramide C10 and C22 standards, 3: hydrogenated yeast, 4: deuterated yeast, 5: ceramide C12 and C18 standards, 6: ceramide C14 standards, 7: ceramide C16 standards, 8: ergosterol standard. Eluent used: hexane-chloroform-acetone-acetic acid (20:70:20:4). Anisaldehyde was used as reagent.

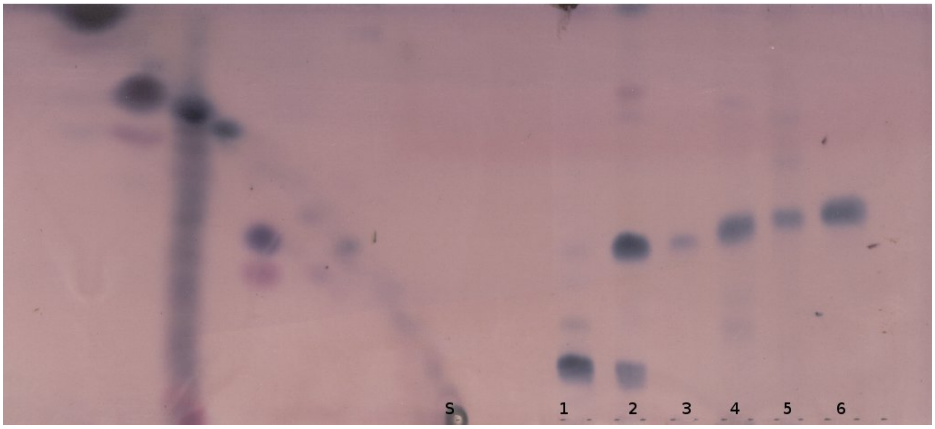

Figure 3.14: Detection of ceramides in hydrogenated yeast by 2D-TLC. Lanes attribution: S: hydrogenated yeast 1: ceramide C2 standard, 2: ceramide C14 standard, 3: ceramide C16, 4: ceramide C18 standard, 5: ceramide C22 standard, 6: ceramide C24 standard. Eluents used:first direction: hexane-chloroform-acetone-acetic acid (20:70:20:4), second direction: chloroform-isopropanol (9:1). Anisaldehyde was used as reagent.

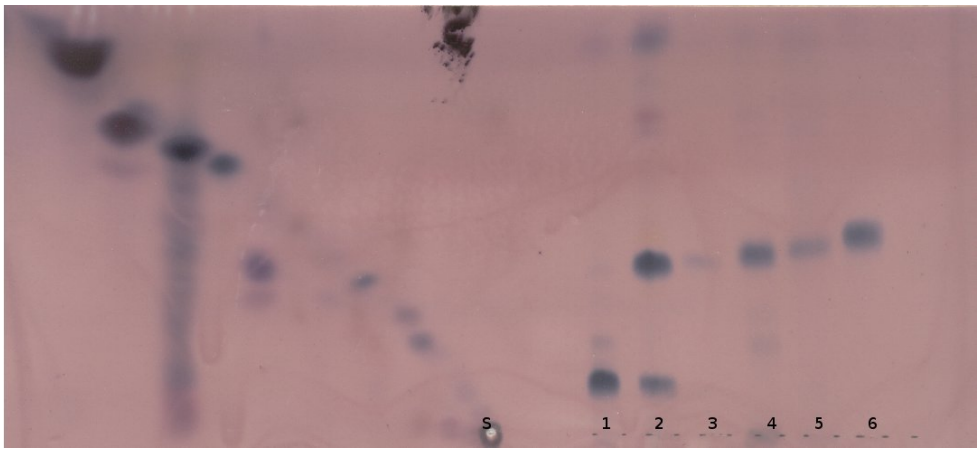

Figure 3.15: Detection of ceramides in deuterated yeast by 2D-TLC. Lanes attribution: S: deuterated yeast 1: ceramide C2 standard, 2: ceramide C14 standard, 3: ceramide C16 standard, 4: ceramide C18 standard, 5: ceramide C22 standard, 6: ceramide C24 standard. Eluents used:first direction: hexane-chloroform-acetone-acetic acid (20:70:20:4), second direction: chloroform-isopropanol (9:1). Anisaldehyde was used as reagent.

3.4 Discussion

3.4.1 Desaturation of fatty acid in yeast

In yeasts, lipids are mainly composed of C16 and C18 fatty acids that are usually produced through *de novo* synthesis, even though yeasts can assimilate exogenous fatty acids when supplied in the growth medium [80]. Acyl-CoA is the first substrate for unsaturation at the level of carbon alpha-9 via the action of a Δ9-desaturase. Δ12- and Δ15- desaturase enzymes catalyze the addition of a second and third double bond on the fatty acid chains when esterified to a glycerolipid. Evidence of the presence of these ubiquitous desaturases in yeasts have been provided [81].

In *Saccharomyces cerevisiae*, lipids are mainly composed of C18:1 and C16:0 [73]. However it is not the case in all yeast species. In *P. pastoris*, it has been shown that the relative amount of polyunsaturated fatty acids is much higher [70, 71]. This pattern was also found in the present work. In comparison, Pichia pastoris cells in deuterated environment produce

mainly C18:1 at the expense of polyunsaturated fatty acid.

In *Saccharomyces cerevisiae* the UFA/SFA ratio is in a steady state and is determined by the competition of the enzymes Ole1p and Sctp1p on the C16:0 acyl-CoA subsrate. Ole1p catalyzes the introduction of the first double bond in the aliphatic chain. Besides, Sctp1p can shield the acyl-CoA substrate to prevent the desaturation triggered by Ole1p. The isotopic substitution may have an effect on the mutual balance of this set of enzymes [82].

Adding a double bond in a fatty-acyl substrate is a very demanding process which involves two electrons and the cleavage of two C-H bond (98 kCal/mol). This reaction consumes molecular oxygen. In nature, there are two clearly identified kinds of $\Delta 9$ desaturase enzymes which introduce the first double bond, in cis or Z conformation, at the alpha-9 carbon. The first one is a plant-specific soluble desaturase and the second one is an integral membrane desaturase found in animals and fungi [73]. The latter is located in the endoplasmic reticulum. The catalytic center of this enzyme is composed of a di-iron site which forms ligands with three characteristics histidine motifs.

When the desaturase enzyme is in a resting mode, the iron atoms are in the oxidation state Fe^{III}-Fe^{III}. When O_2 is bound, the di-iron moiety forms a peroxydo bridge Fe^{III}-O-O-Fe^{III}. Then the O-O bound is cleaved which leads to the formation of Fe^{IV}-$2O_2$, a diamond shaped "Q" intermediate as shown in the figure 3.16. The reduction potential of this complex is high enough to extract two protons and two electrons to the fatty acyl chain [73].

The Kinetic Isotopic Effect (KIE) consists in replacing a CH_2 by a CD_2 unit in different positions in the fatty acid chain and measuring the kinetics of the desaturation process. It has been shown that when deuterium substitutes hydrogen bound to carbon in position 9, the constant rate of the desaturation reaction is reduced by a factor of 7, whereas deuterium substitution on carbon 10 does not affect the desaturation rate [83, 84].

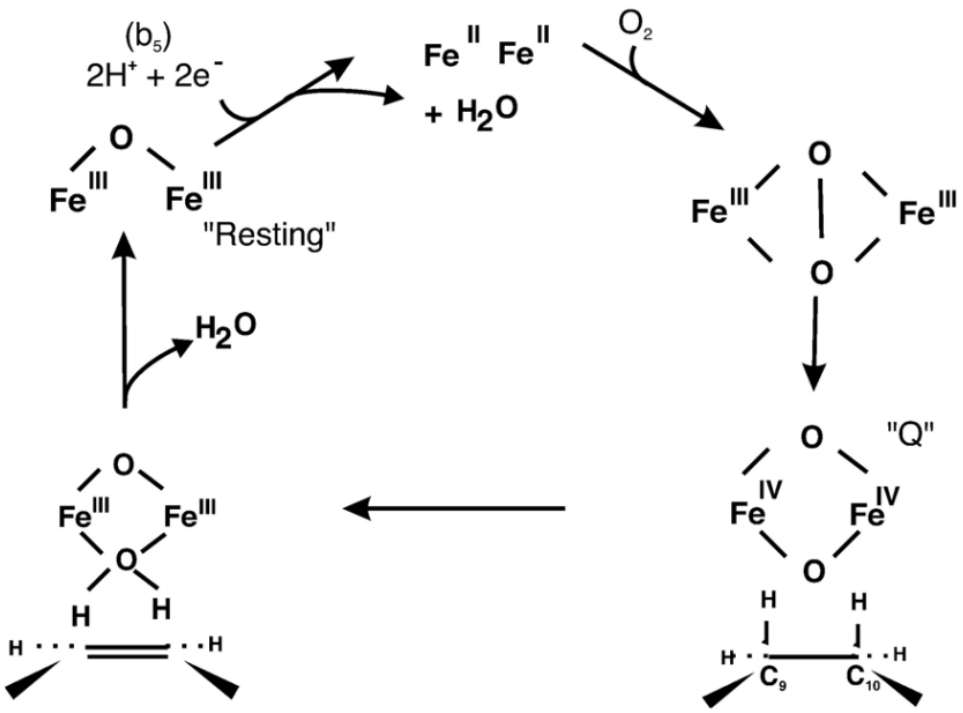

Figure 3.16: Proposed mechanism for diiron-oxo mediated fatty acid desaturation by Martin & al [73]

.

This experiment was performed to show that the desaturation occurs in two steps. It also means that the presence of deuterium in a particular location can highly slow down the desaturation reaction.

The KIE is consistent with all experiments reported here in vivo, and provides clues to comprehend why the amounts of C18:2 and C18:3 in deuterated fatty acid were so low. If deuterated substitution in carbon slows down the introduction of one double bond, one can expect that it has the same effect for the addition of supplementary double bonds. Therefore the action of the Δ12- and Δ15-desaturase enzymes might be slowed down because of the fully deuterated chains, consequently C18:1 is accumulating in the fatty acid pool.

Decreasing culture medium temperature slows down the growth rate of yeast cells and stimulates fatty acid desaturation, compensating partially the reduced activity rate of Δ12 and Δ15 enzymes. Nevertheless this effect is not strong enough to produce as much PUFA as in the hydrogenated species.

3.4.2 Glycerophospholipid metabolism and regulation

The major phospholipids in yeast are PC, PE, PI, PS, PG and CL [74]. In *de novo* biosynthetic pathways, phosphatidic acid (PA) is the precursor of all phospholipids. It can be converted in CDP-DAG, an intermediate for the production of PI, CL and PS. In this route, PE is made from PS via the action of decarboxylases. PE then undergoes three successive methylations to generate PC. Alternatively, PA can be dephosphorylated into diacylglycerol (DAG) that can react with choline-CDP and phosphoethanolamine-CDP to produce PC and PE [74, 85, 86]. The two pathways are depicted in figure 3.17. Both pathways are functional in wild type yeast cells even in the absence of choline or ethanolamine in the growth medium [87].

The similar dependence in fatty acid composition in PI and PS as a function of different growth temperatures or isotopic medium is explained by the fact that they are produced through the same pathway. However, the fatty acids patterns in PC and PE are different. This suggests that there might be a regulation of phospholipids happening downstream fatty acid

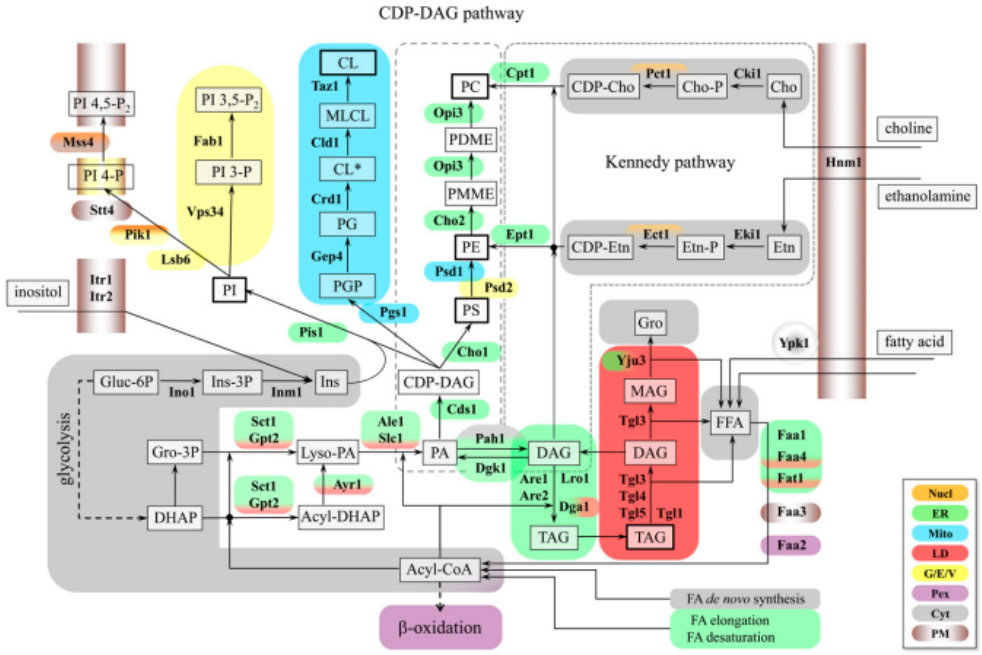

Figure 3.17: Pathways for the production of glycerophospholipid in yeast. From Henry & al. [74]

neo-synthesis at still uncharacterized levels of glycerolipid metabolism.

3.5 Conclusions

The aim of this work was to find a way to produce naturally relevant deuterated lipids difficult to obtain from the synthetic molecular species commonly used for biophysical studies. The ability of the yeast species *Pichia pastoris* to grow in fully deuterated environment has been widely used as expression system to produce fully deuterated proteins [67]. Therefore we used this system to produce deuterated unsaturated glycerolipids that are not commercially available. The results highlighs that the deuterated growth medium does not affect *P. pastoris* phospholipid class general homeostasis.

However, the fatty acid composition in each class of lipids is different to that observed in the cells growing in a hydrogenated medium. An accumulation of C18:1 fatty acid is strikingly triggered in deuterated lipids. Lowering temperature decreases this effect but the amount of PUFA does not reach the level obtained in hydrogenated yeast.

Based on the *in vivo* analyses and on previously published *in vitro* characterization of desaturases, this works suggest that *Pichia pastoris* is a model of choice as a cell factory for deuterated glycerolipids and that the production of deuterated PUFA might be improved by lowering the growth temperature and by the expression of heterologous genetic sequences coding desaturase enzymes, as reported in hydrogenated *P. pastoris*, being less sensitive to a deuterated substrate [88, 89].

A protocol was also found to separate deuterated PC and deuterated PE from the other phospholipids. Both are important because they are the most investigated lipids in biophysics. However this separation was made by means of a flash chromatography which eluted the lipids as a function of the headgroup. Therefore, the purified deuterated PC and deuterated PE still contains a different unsaturation degree and the process must be continued further in the future up to the purification of the molecular species. To do so, reversed-phase chromatography is needed in order to separate the different PC species as a function of their fatty acid

composition.

The sphingolipids analysis showed that, as expected, sphingomyelin is absent in yeast. The two main sphingolipids in yeast are glucosylceramide and inositolphosphoceramide [78]. The former could be identified in both hydrogenated and deuterated yeast even though further analysis needs to be done to ensure that it is not another compound. The latter was not identified in here. The ceramide analysis showed that there are still numerous compounds but in a very low quantities which are present and not yet identified.

Chapter 4

Interaction of amphotericin B with yeast membranes

4.1 Introduction

Amphotericin B (AmB) is a polyene macrolide molecule which has been used as antibiotic for more than 50 years [90, 91]. Its structure is shown in figure 4.1 where the hydrophobic and hydrophilic parts are clearly visible [92]. It is used mainly against fungal infection because of its ability to interact preferentially with ergosterol over cholesterol. Methyl ester AmB has also other interesting curative properties such as an anti-HIV activity [93]. However, 60 years of intense medical use has evidenced side effects relative to the drug [94, 95]. The first model developed to describe the mode of action against fungal infection is the aqueous pore formed by the AmB-sterol complexes that can make a membrane permeable to K^+ leading to cell death [96–99]. The initial model involves a complex made of 6 AmB and 6 sterol molecules bound by hydrophobic interaction [97] as depicted in the space filling model in figure 4.2. The sterol molecules fill the gap at the outer side of the ring created by AmB molecules. Therefore, the inside is hydrophilic and the diameter of the channel is 8 Å, large enough to allow the ions and small molecules such as glucose to cross the membrane. By comparing the length of AmB and of a phospholipid molecule, two complexes are needed to form a pore which spans the entire

membrane.

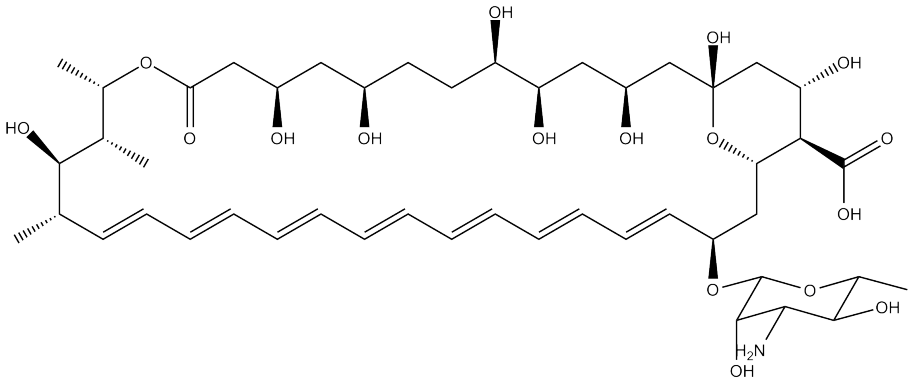

Figure 4.1: Structure of amphotericin B.

Bolard & al. [100] showed that the insertion mechanism of AmB within the membrane is different whether the membrane contains ergosterol or cholesterol. By measuring the K^+ leakage they observed that AmB should self-assemble in solution before being able to form pores through cholesterol-containing membrane, whereas it is responsible for the K^+ leakage in ergosterol-containing membranes even as a monomer.

The ion-conducting pore model was challenged by other observations stating that the K^+ leakage induced by AmB interaction does not lead necessarily to the cell death; therefore K^+ leakage and lethal effect are dissociated [101–104]. Cohen suggested a model in which non aqueous channel are first formed at low AmB concentration and makes the membrane permeable to small ions. Only after a critical AmB concentration the non aqueous channel interact with cholesterol or ergosterol to form an ionic channel that causes the cell death [105, 106] as shown in figure 4.3. However, more recent studies showed that AmB induces channels even in sterol free membranes which could mean that sterols might have no direct effect on the pore formation but rather an indirect effect since their presence changes the structure of the membrane [107–110]. Moreover, it has been showed that the sterol concentration also affects the interaction with AmB in planar lipid bilayers and monolayers [111, 112].

More recently, numerous biophysical studies have been carried out on model membranes composed of phosphatidylcholine (PC) in presence of

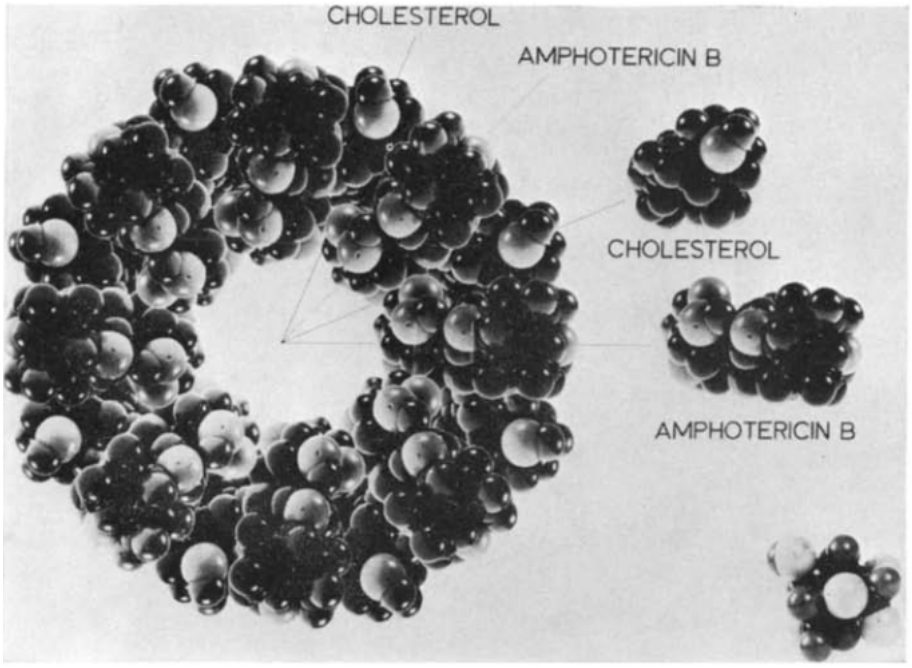

Figure 4.2: Space-filling model suggested of the AmB-cholesterol complex forming a pore, from de Kruijff & al. [97].

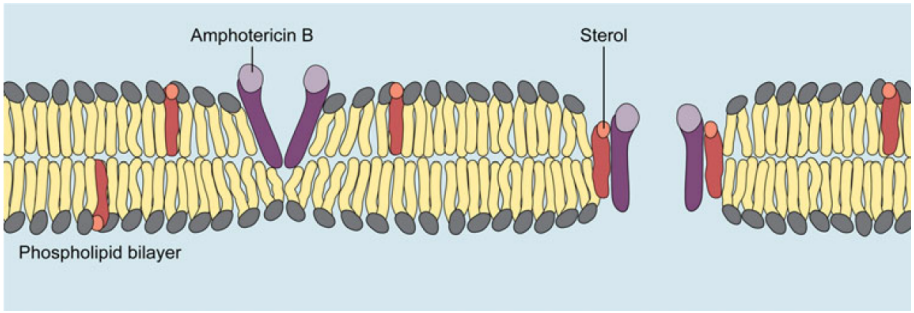

Figure 4.3: Sketch of the non aqueous and aqueous channel made by the presence of AmB in sterol-containing membrane, by Cohen [106]

cholesterol or ergosterol, and new insights on the AmB interaction with lipid bilayers at a molecular level are obtained. A study performed on egg yolk PC showed on the basis of IR spectroscopy, that AmB first interacts with the headgroups before its insertion in the hydrophobic core of the bilayer [113]. Another study, also on egg yolk PC using ^{1}H NMR, showed that AmB bound preferentially to the headgroups [114]. This suggests that AmB first binds with the headgroup inducing a conformational change in the lipid packing which facilitates its insertion within the membrane. Milhaud & al. proposed on the basis of combined AFM, circular dichroism and differential scanning calorimetry measurements that the mechanism of AmB insertion is made by a "digging" process from aggregated AmB located at the top of a DLPC bilayer [115]. A small angle neutron scattering study on POPC and cholesterol- or ergosterol-containing vesicles showed that the preference of AmB for ergosterol-containing membranes over cholesterol-containing membranes does not arise from structural differences induced by the two sterols but more likely for kinetic and enthalpic reasons [116].

All these biophysical methods are very powerful thanks to their ability to give information on the interaction at a molecular scale. However, they are generally carried out on model membranes even though the complex lipid composition of natural membranes can play an important role. In the present work, the interaction of AmB with different yeast lipid extracts in the form of planar supported bilayers is investigated by neutron reflectometry. Neutron reflectometry is an ideal technique for such studies because it can give information on the depth profile at the Å-scale resolution. Moreover, the possibility to change the scattering length density of the subphase can greatly enhance the resolution of the technique and allow highlighting the different parts of the system under study. The yeast cells were grown in hydrogenated and deuterated environment in order to have a strong scattering length density contrast with the hydrogenated AmB.

4.2 Bilayer characterization

4.2.1 Substrate characterization

Before injecting vesicles, the substrates were measured in two contrasts, H_2O and D_2O, in order to characterize the structural parameters of the silica layer (thickness and roughness). These parameters were then fixed during the fit of the following studied lipid bilayers. Typical neutron reflectivity curves arising from a silicon substrate in D_2O (grey diamond) and H_2O (black square) are shown in figure 4.4 as an example. The fits obtained with a simple box model that includes the roughness are also showed in figure 4.4 as lines.

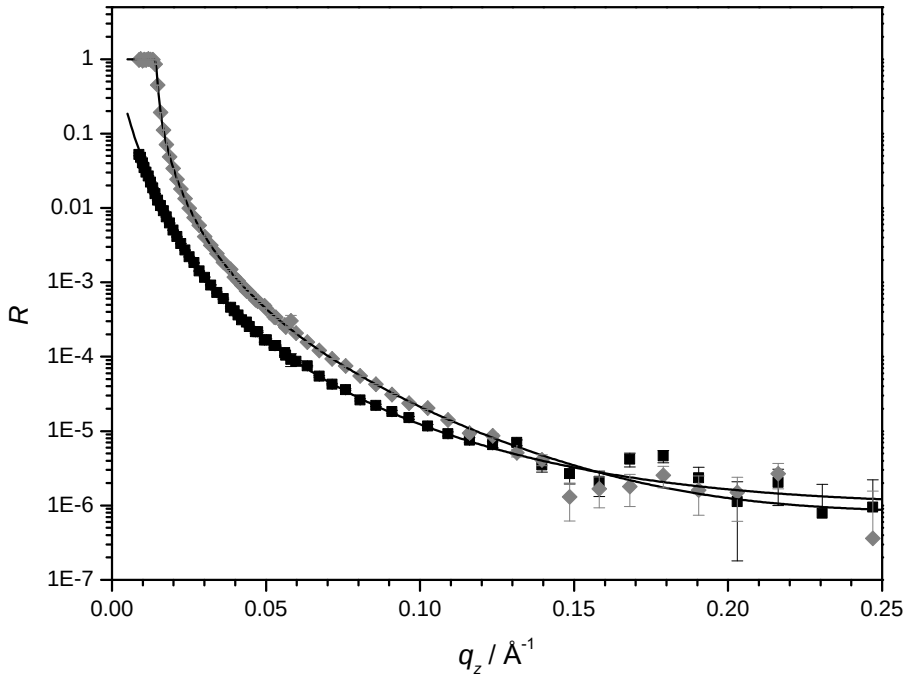

Figure 4.4: Example of neutron reflectivity curves from a bare silicon substrate in H_2O (black square) and D_2O (grey diamond) and their corresponding fits (black solid line). The fits revealed a SiO_2 thickness of 10 $\pm$ 2 Å and a roughness of 2 $\pm$ 2 Å.

4.2.2 Deposition of lipid bilayers by vesicle fusion method

The planar supported bilayers were prepared from unilamellar vesicles by the vesicle fusion method [117–119]. This technique consists of bringing unilamellar lipid vesicles in contact with a solid substrate. Upon a certain ionic strength and thermal conditions, the vesicles break spontaneously to form a planar lipid bilayer.

The protocol used to form the different fractions hPL, hPL+S, dPL, dPL+S, namely hydrogenated Polar Lipids, hydrogenated Polar Lipids + Sterols, deuterated Polar Lipids and deuterated Polar Lipids + Sterols, is described in the previous chapter.

The lipid extracts from yeast cells were dissolved in a chloroform : methanol solution (2:1 v/v). The solution was dried in a vial by means of a stream of nitrogen until lipids formed a thin film around the glass wall. They were then dispersed in a salt solution (NaCl 100 mM, $CaCl_2$ 20 mM) by repeated sonication pulse at 55 Hz for 30 minutes. The lipid vesicle solutions were kept at 65°C before being injected into the experimental reflectivity cell. The vesicle fusion was previously characterized by means of QCM-D to ensure that the good experimental conditions were met before the neutron reflectometry experiments.

The figure 4.5 shows the QCM-D curves of a unilamellar sonicated vesicle composed of dPL+S. After vesicle injection, there are a high frequency and dissipation shifts occurring for about 30 minutes which denotes the formation of a vesicular layer onto the substrate. After rinsing with salt solution, df and dD do not change dramatically, indicating that the big vesicular layer does not disrupt to form a planar lipid bilayer. Rinsing with pure water creates an osmotic gradient between the medium trapped within the vesicular layer and the subphase inducing vesicle rupture and planar lipid bilayer formation. This behaviour is well described by the abrupt increase of df and decrease of dD. The salt solution is then injected in the chamber to compare the difference in df and dD in the final stage to their values obtained during calibration of the sensor in salt solution before the vesicle injection.

The preliminary QCM-D experiment shows that higher temperature

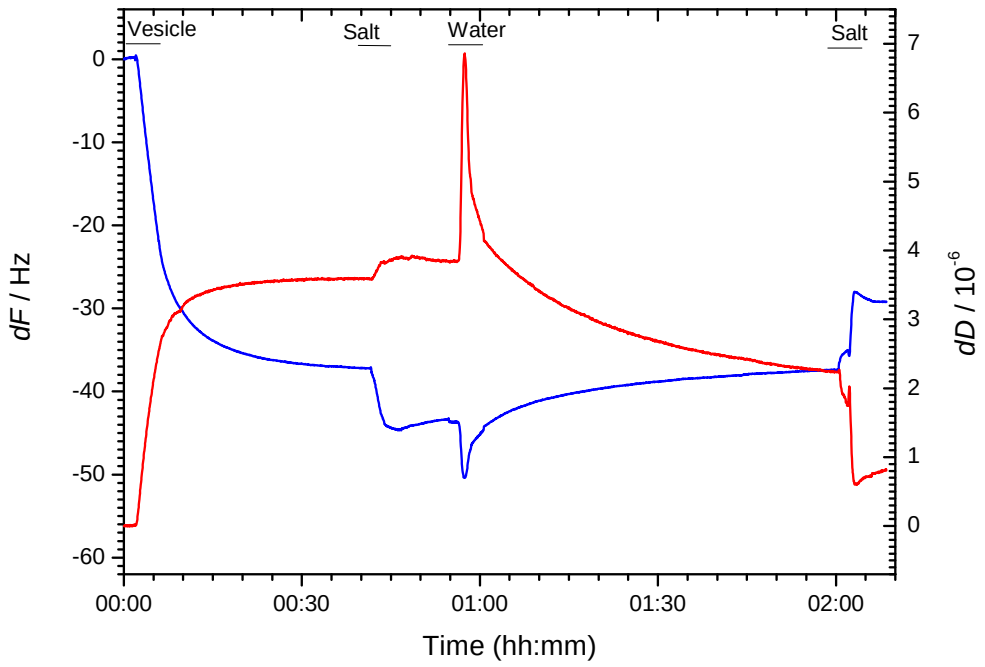

Figure 4.5: QCM-D frequency shift df and and change of dissipation factor (dQ) (ninth overtone) recorded during dPL+S vesicle adsorption at 65°C for dPL+S in NaCl 100 mM and $CaCl_2$ 20 mM at 50 °C. Top lines description: vesicle: vesicle injection. Salt: Salt solution rinsing. Water: Pure water rinsing. Salt: Salt solution rinsing.

and higher ionic strength in the vesicle solution as well as longer time are needed for the vesicle to fuse and rupture to form a planar supported bilayer compared to system composed of pure DPPC (as shown in the second chapter). It is known that the planar lipid bilayer formation from unilamellar vesicles in solution depends on many parameters such as vesicle size, temperature, surface chemistry and osmotic pressure [120]. The presence of negatively charged lipids tends to prevent the lipid bilayer formation. It has been demonstrated that adding calcium ions in the solution helps the vesicle to break [121]. The investigated yeast lipid extracts contain about 30 % of negatively charged lipid and this explains the different behaviour with respect to uncharged model lipid systems.

4.2.3 Lipid bilayer characterization

After the characterization of the silicon substrates, all the bilayers were characterized in at least three contrasts. To fit the reflectivity data, the scattering length density (ρ) of the headgroup region was calculated according to the relative amount of each phospholipid class and to the molecular volume values found in literature for the hydrogenated species. Since PE, PI and PS are able to exchange labile hydrogen or deuterium with the subphase, the headgroup scattering length densities were also calculated according to the used contrast. Table 4.1 shows the chemical formula, the molecular volume and the relative amount of the four main hydrogenated and deuterated phospholipids in light and heavy water. Tables 4.2 and 4.3 show the averaged scattering length densities for hydrogenated and deuterated headgroup in the four contrasts used in this work. The four contrasts are D_2O, H_2O, and mixtures of H_2O and D_2O matched to $4*10^{-6}$Å^{-2} (called CM4) or to the scattering length density of silicon (called CMSi). The final scattering length density was calculated by averaging the scattering length density of each headgroups as a function of their relative amount.

Table 4.1: Chemical formula, molecular volume (V_m) and relative composition of the four main phospholipids headgroups found in yeast in the hydrogenated and deuterated forms. Since some of them contains labile proton or deuterium, the chemical formula might change because of proton exchange.

	Chemical formula		V_m (Å^3)	relative %
	H_2O	D_2O		
h-PC	$C_{10}H_{18}O_8PN$	$C_{10}H_{18}O_8PN$	323 [122]	53.1
h-PE	$C_7H_{12}O_8PN$	$C_7H_9O_8PND_3$	235 [123]	22.2
h-PS	$C_8O_{10}H_{10}PN$	$C_8O_{10}H_8PND_2$	335 [122]	13.5
h-PI	$C_{11}O_{13}H_{16}P$	$C_{11}O_{13}H_{11}PD_5$	372 [124]	11.1
d-PC	$C_{10}D_{18}O_8PN$	$C_{10}D_{18}O_8PN$	323	48.2
d-PE	$C_7D_9O_8PNH_3$	$C_7D_{12}O_8PN$	235	20.1
d-PS	$C_8O_{10}D_8PNH_2$	$C_8O_{10}D_{10}PN$	335	17.6
d-PI	$C_{11}O_{13}D_{11}PH_5$	$C_{11}O_{13}D_{16}P$	372	14.0

Table 4.2: Calculated scattering length density (ρ) in the four used contrasts and averaged scattering length density from the relative composition of each species of the headgroups from the hydrogenated yeast lipid extract. All the values are expressed in 10^{-6} Å^{-2}.

	D_2O	CM4	CMSi	H_2O
h-PC	1.86	1.86	1.86	1.86
h-PE	3.99	3.47	3.11	2.66
h-PS	3.25	3.02	2.85	2.64
h-PI	3.92	3.39	3.00	2.52
Averaged ρ				
	D_2O	CM4	CMSi	H_2O
	2.82	2.60	2.44	2.25

Table 4.3: Calculated scattering length density (ρ) in the four used contrasts and averaged scattering length density from the relative composition of each species of the headgroups from the deuterated yeast lipid extract. All the values are expressed in 10^{-6} Å^{-2}.

	D_2O	CM4	CMSi	H_2O
d-PC	7.66	7.66	7.66	7.66
d-PE	7.98	7.53	7.15	6.65
d-PS	5.74	5.53	5.35	5.12
d-PI	7	6.52	6.13	5.60
Averaged ρ				
	D_2O	CM4	CMSi	H_2O
	7.40	7.22	7.07	6.86

Hydrogenated yeast lipids

Figure 4.6 shows on the left the experimental reflectivity data as well as the fitted curves as lines in four contrasts for the hPL and hPL+S bilayers and corresponding scattering length density profiles on the right. The reflectivity curves in H_2O are similar to the reflectivity curves from the bare substrate measured in H_2O since the bilayers are hydrogenated and their scattering length densities match that of the subphase. In D_2O, the reflectivity profiles from both bilayers present is very different compared the reflectivity measured from the bare substrate in D_2O because there is a strong contrast between the bilayers and the subphase.

The hPL bilayer is thinner than model lipid bilayers composed of DPPC or DOPC, generally used in biophysical studies, with a chain region of 24 $\pm$ 4 Å thick. Furthermore, there is a big difference in the roughness between the inner headgroup and tail regions (3 $\pm$ 2 Å) and between the tail and the outer headgroup regions (6 $\pm$ 2 Å). The inner and outer headgroup regions are as thick as model PC bilayer (7 $\pm$ 2 Å) [122]. The scattering length density of the tail region is -0.43 $\pm$ 0.60 10^{-6} Å^{-2}. The hPL+S bilayer presents a thicker chain region (28 $\pm$ 2 Å) than the chain region of the bilayer in absence of sterol. There is the same difference between the roughness at the inner headgroup and tail boundary (3 $\pm$ 2 Å) and the

Table 4.4: Fitted headgroup and tail parameters of the hPL, hPL+S, dPL and dPL+S bilayers. t = thickness (Å); ρ = scattering length density (10^{-6} Å^{-2}), ϕ (solvent fraction); σ = roughness (Å). The errors correspond the parameters uncertainties.

	hPL	hPL+S	dPL	dPL+S
Inner Headgroup				
t	8 ± 3	7 ± 3	7 ± 2	7 ± 2
σ	3 ± 2	3 ± 3	3 ± 2	6 ± 6
Tail				
t	24 ± 4	28 ± 2	32 ± 3	32 ± 7
ρ	-0.43 $\pm$ 0.60	-0.16 $\pm$ 0.23	6.61 $\pm$ 0.06	6.52 $\pm$ 0.16
ϕ	3 ± 3	3 ± 3	2 ± 2	2 ± 2
σ	8 ± 2	5 ± 1	<5	6 ± 2
Outer Headgroup				
t	8 ± 3	7 ± 3	7 ± 2	7 ± 2
σ	5 ± 2	3 ± 3	3 ± 2	6 ± 1

roughness at the tail outer headgroup boundary (6 ± 2 Å) as observed in the polar lipid region. The scattering length density of the chain slightly increases up to -0.16 $\pm$ 0.24 10^{-6} Å^{-2}.

The structural results of the hPL bilayer shows that the total thickness is lower than the one generally measured with model membranes. The hPL total thickness is of 38 Å with hydrophobic core thickness of 24 ± 2 Å, which is thinner than the thickness of tail region of model membranes from DOPC (29 Å) [125]. This observation is explained by the high unsaturation degree which makes the membrane thinner connected to the the natural double bonds in cis-isomerism. This conformation prevents the tails from being packed due to the steric repulsion.

Another interesting feature is the difference in the roughness value between the two headgroup-tail interfaces, which leads to an asymmetric scattering length density profile (figure 4.6, B). This difference could be related to the fatty acid distribution of this lipid extract. The high roughness value between the outer headgroup (subphase side) and tail regions could

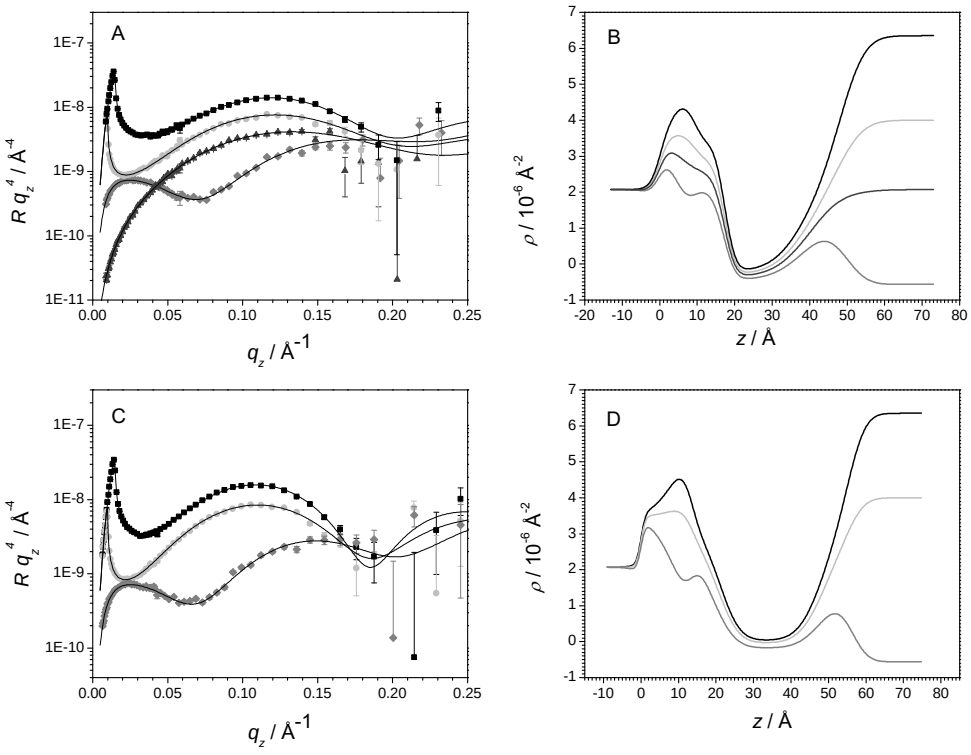

Figure 4.6: Left: Reflectivity curves and corresponding fits from (A) hPL and (C) hPL+S bilayers deposited on a silicon substrate in D_2O (black square), CM4 (light grey circle), CMSi (dark grey triangle) and H_2O (grey diamond). Scattering length density profiles obtained from the fits of (B) hPL and (D) hPL+S in D_2O (black), CM4 (light grey), CMSI (dark grey) and H_2O (grey).$z = 0$ at the Si-SiO_2 interface.

be related to the inhomogeneous fatty acid composition, inducing a length polydispersity of the tails. The roughness between the inner headgroup (substrate side) and tail regions is much lower and is probably connected to the presence of the rigid flat substrate. The scattering length density of the tail region (-0.43 $\pm$ 0.60 10^{-6}Å^{-2}) is quite low low considering that the bilayer is in fluid phase but it is worth stressing that there is a considerable parameter uncertainty. The headgroup thickness is not significantly different to the one found in PC model membrane [122].

The most obvious feature of the hPL+S bilayer is the enhanced hydrophobic tail thickness in comparison to the hPL bilayer (see table 4.4). The main sterol component in *P. pastoris*, and in yeast in general, is ergosterol [70]. It has been shown by simulation that ergosterol has a lateral condensing effect which makes the membrane thicker [126]. It is not possible here to conclude where exactly the sterol molecules lie, only the effect on the tail thickness can be observed. Also in presence of the sterols, the same asymmetry in roughness between the two headgroup-tail interfaces is found because of the broad fatty acid composition. The molecular volume for ergosterol obtained from crystallographic data is 630.3 Å^3 leading to a scattering length density of 0.43 10^{-6} Å^{-2} [127]. The fitted scattering length density of the tail layer is -0.16 $\pm$ 0.23 10^{-6} Å^{-2} which is consistent with the presence of sterol having a positive scattering length density value.

Deuterated yeast lipids

Figure 4.7 shows the reflectivity curves and corresponding fits for dPL and dPL+S bilayers (left) as well as the corresponding scattering length density profiles (right). The neutron reflectivity curves measured in D_2O present no minima or maxima since the scattering length density of the bilayers matches the scattering length density of the subphase. Reflectivity measured in the three other contrast is much more sensitive to the presence of the deuterated bilayers.

It is worth noting that dPL bilayer is thicker than the corresponding hydrogenated one. This is probably due to the abundance of C18:1 chains

in the chain region which presents a thickness of 30 $\pm$ 2 Å. This thickness is the same as found in synthetic DOPC bilayer [125]. One other feature compared to the hydrogenated version is the lower roughness at the two headgroup-tail boundaries, 3 $\pm$ 2 Å and 2 $\pm$ 2 Å, respectively. The scattering length density of the chains is 6.58 10^{-6} $Å^{-2}$ confirming that the bilayer is fully deuterated. The headgroup thickness is 7 $\pm$ 2 Å as in the case of hPL bilayer.

The dPL+S bilayer shows less structural variation with respect to dPL compared to the hydrogenated pair. The chain thickness and scattering length density are similar (6.56 10^{-6} $Å^{-2}$). The headgroup thickness does not present any changes (7 $\pm$ 2 Å). The main difference is the enhanced roughness between headgroups and tails (6 $\pm$ 2 Å).

The hydrophobic chain region of dPL is considerably thicker than that in hPL. This is due to the prominent C18:1 fatty acid content in the chain composition in dPL as compared to hPL in which C18:2 and C18:3 contents are far from being negligible. The measured thickness in the dPL bilayer is 32 $\pm$ 3 Å which is in good agreement with hydrophobic tail thickness of C18:1-C18:1 PC vesicle of 29 Å found in literature [125]. It is noticeable that the roughness between the hydrophobic and hydrophilic parts of the dPL bilayer is much lower compared to the hPL bilayer. Since the chain composition of the deuterated yeast lipid extract is composed of nearly 65% of C18:1 fatty acid, the chain lengths are more homogeneous leading to smoother hydrophobic-hydrophilic interfaces within the lipid bilayer.

The scattering length density of the hydrophobic region indicates that the bilayer is perdeuterated and in fluid phase. The headgroup thickness is the same for the hydrogenated lipid bilayer which is consistent with the fact that the relative amount of phospholipid headgroup species composition is not affected by the deuterated growth medium. Unlike the hydrogenated corresponding bilayers, the dPL+S bilayer is not significantly thicker than dPL one. The scattering length density of the tail region has the same value within errors as well. The main difference is the enhanced roughness at the headgroup tail boundaries (see scattering length density profile in figure 4.7, D). This effect suggests that sterol molecules are located upright in the bilayer since they modify the structural properties at

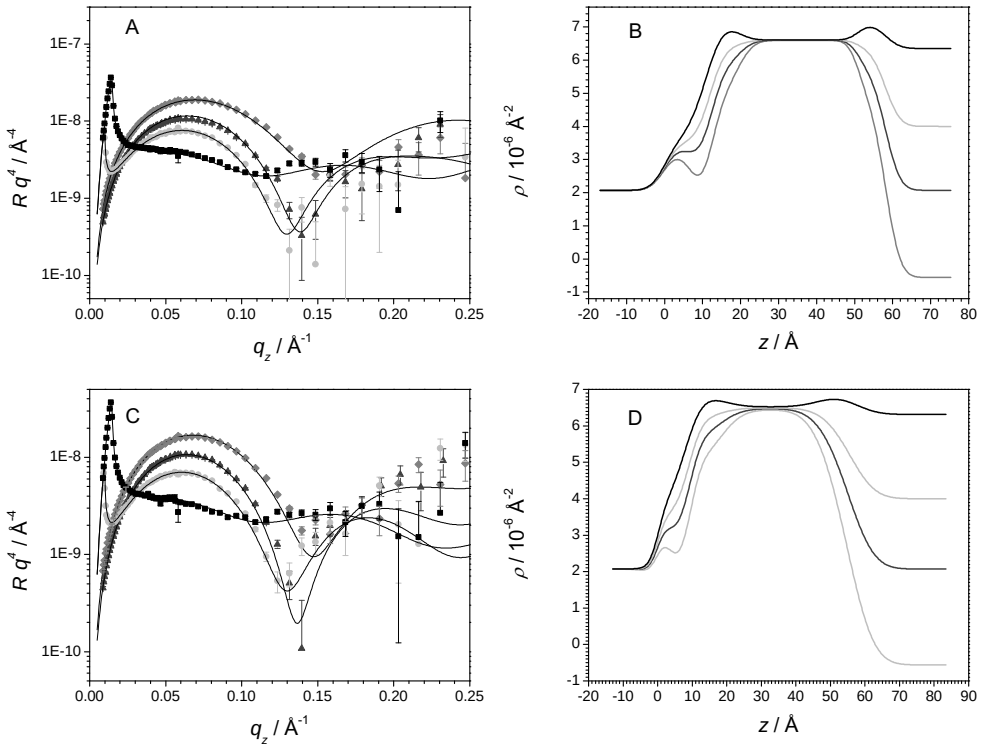

Figure 4.7: Left: Reflectivity curves and corresponding fits from (A) dPL and (C) dPL+S bilayers deposited on a silicon substrate in D_2O (black square), CM4 (light grey circle), CMSi (dark grey triangle) and H_2O (grey diamond). Scattering length density profiles obtained from the fits of (B) dPL and (D) dPL+S in D_2O (black), CM4 (light grey), CMSI (dark grey) and H_2O (grey).$z = 0$ at the Si-SiO_2 interface.

the hydrophilic-hydrophobic interface and do not increase the hydrophobic core thickness.

4.3 Interaction of amphotericin B with lipid bilayers

4.3.1 Hydrogenated yeast lipids

The reflectivity curves in D_2O, CM4 and H_2O from the hydrogenated bilayers before and after AmB incubation are shown in (figure 4.8) for hPL (A) and hPL+S (C). A solution of AmB 10^{-3} M was injected and left one hour in the sample cell to let AmB incubate with the bilayers. The reflectivity curve from hPL bilayer are slightly shifted toward higher q_z values after AmB interaction in D_2O and CM4. In H_2O, the first minimum is shifted to a lower q_z value of 0.05 $Å^{-1}$. The scattering length density profiles obtained from the fits show that the structure of the bilayer is not changed after the interaction with AmB. The profiles also reveal the appearance of a thick and diluted layer on the top of the lipid bilayer.

The effect of the presence of AmB on reflectivity curves from the hPL+S bilayer is more pronounced than that from hPL bilayer (figure 4.8, C). The curves measured in D_2O and CM4 considerably changed towards higher q_z values. The scattering length density profiles obtained from the fits show clearly that there is a change in the structure of the bilayer itself, in addition to the appearance of the layer on the top of it.

When AmB is in contact with the hPL bilayer, the fits show the appearance of a thick (37 Å) and very diluted (solvent fraction of 0.83) layer on the bilayer which cannot be rinsed away, even after thorough rinsing of water, suggesting that this layer is somehow anchored to the lipid bilayer. Another effect is the slight thinning of the outer headgroups (6 Å) while the tail thickness is not significantly affected by AmB.

In the case of the hPL+S layer, the reflectivity curves present a bigger effect induced by the AmB presence (figure 4.8, D). The results from the fits show that there is also a same thick and diluted layer (39 Å thick and

Table 4.5: Chemical formula, molecular volume and scattering length density in different subphase of amphotericin B. V_m = molecular volume (Å^3), ρ = scattering length density (10^{-6}Å^{-2}).

Subphase	Formula	V_m (Å^3)[116]	ρ
H_2O	$C_{47}H_{73}NO_{17}$	973	1.51
4MW	$C_{47}H_{65}NO_{17}D_8$	973	2.36
D_2O	$C_{47}H_{61}NO_{17}D_{12}$	973	2.80

volume fraction of 0.77) on the top of the bilayer which cannot be rinsed away. In addition to this effect, a significant thinning of the whole bilayer (both headgroups + tail) occurs. The scattering length density of AmB was calculated according to the molecular volume found in literature (see table 4.5) [116].

Such scattering length density profile might correspond to what has been already observed by Milhaud & al [115], i.e. a bilayer covered by materials (made of AmB) polydispersed in size. They observed this phenomenon via AFM but the DLPC bilayer was mixed with AmB before being deposited on mica substrate. The adsorbed layer could not be displaced if the tip exerted a pressure lower than 10 nN, which means that the layer was bound to the membrane. The situation is a bit different in this work since this additional layer comes from AmB adsorbed from the subphase. This layer is also bound to the membrane since the system is washed several times with pure water without affecting it.

It is worth noting that the outer headgroup regions gets thinner in hPL bilayer but the thickness and scattering length density of the tail region for both h- and dPL bilayer is not affected by the adsorption of amphotericin B. AmB is probably bound to the headgroup through H bonds as it has been already suggested by Gabrielska & al [114], and electrostatic interactions due to the presence of negatively charged phospholipids (PI, PS, PG). Since the headgroup relative composition is the same for all the investigated bilayers, it is then not surprising that the same effect occurs at the level of the outer headgroup region. Moreover, it has been already shown that when bound to a DPPC monolayer, half of AmB molecules

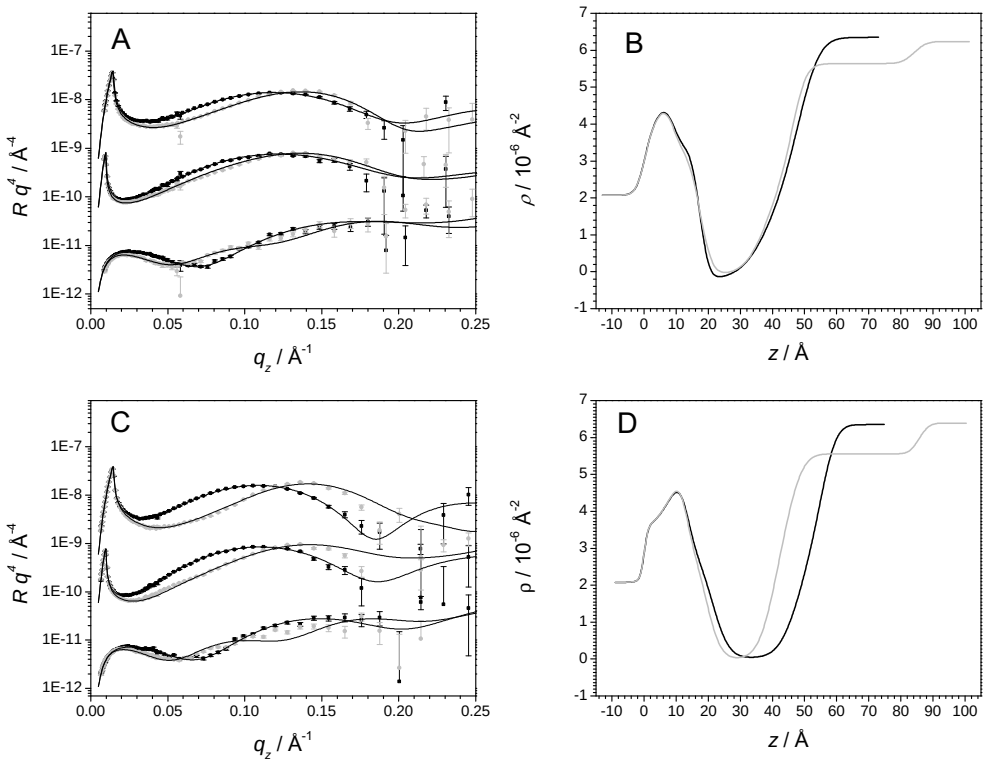

Figure 4.8: Left: Reflectivity curves and corresponding fits from (A) hPL and (C) hPL+S bilayer deposited on a silicon substrate in D_2O, CM4, and H_2O before (black) and after (grey) the incubation of AmB. The curves in CM4 and H_2O are shifted by a factor of 10 and 100 for clarity. Right: Scattering Length Density profiles obtained from the fits of the (B) hPL and (D) hPLS bilayers in D_2O before (black) and after (grey) the incubation of AmB. $z = 0$ at the Si-SiO_2 interface.

stand parallel to the bilayer plane located at the headgroup region [128].

The concentration of the AmB solution used in this work is of 1 mM. Since the concentration threshold for the aggregation is of 10^{-7} M, AmB in solution was probably already in the aggregated form [129]. Theoretical studies on the conformation of self-association of AmB dimers in water showed that the double helix conformation is the most energetically favorable [129]. In this configuration, each cell of the aggregate is composed of two AmB molecules which lie side by side in the same plane. According to this study, the intracell distance is 4.9 Å, the helicoidal angle is of 30° and the nearest neighbor intercell distance is 5.8 Å. If the helix axis is parallel to the bilayer plane, the additional layer of AmB would not have a thickness superior to the length of an AmB molecule, i.e. 25 Å, and the AmB layer should contain much less water since helicoidal arrangement has no finite length. This suggests that the AmB helicoidal axis is rather perpendicular to the bilayer plane. By assuming that the AmB molecules in the thick top layer are in the helicoidal configuration, the layer should contain between 6 and 8 dimer units.

As for PL bilayers, the scattering length density profiles (figure 4.8, B and D) shows that the interaction of AmB with hPL+S bilayer leads also to an additional layer on the lipid bilayer which might correspond to the AmB objects as described above. Besides this effect, another striking consequence of the AmB incubation is the thinning of the whole bilayer. The bilayer thickness after the interaction with the drug is the same as the length of one AmB molecule suggesting that it is inserted perpendicular to the bilayer plane. This is consistent with the formation of pores permeable to ions.

Milhaud & al. observed that the objects on the top of the ergosterol-containing bilayer were hollow-centered [115]. This shape cannot be detected by means of neutron reflectometry, but it is consistent with the scattering length density profile of the bilayers after the interaction with AmB. They proposed a digging mechanism which was initiated from these big objects embedded within the sterol-containing bilayer. The thinning of the bilayer and the presence of such islands also support this interpretation. Moreover, the absolute value of the scattering length density is lowered

which can be explained by either a less dense packing of the tail or the presence of AmB which has a positive scattering length density.

The thinning of the bilayer corresponds to a channel which is one AmB thick, as proposed by Van Hoogevest and De Kruijff [98]. This result is contradictory with the membrane thickening found by Foglia & al. [130] on the basis of neutron diffraction from stacks of model membranes. To explain this discrepancy, it is worth noting that in this work, the AmB inserts into the membrane from the subphase while AmB was codissolved with lipids in the work carried out by means of neutron diffraction.

4.3.2 Deuterated yeast lipids

Figure 4.9A shows the reflectivity curves from dPL bilayer in D_2O, CM4 and H_2O before and after incubation of AmB. One can observe that after AmB injection, the reflectivity profile presents a fringe around 0.2 $Å^{-1}$ in D_2O. Since the subphase matches the bilayer, the appearance of this fringe can only comes from hydrogenated material, i.e. AmB molecules. The scattering length density profiles obtained from the fits (figure 4.9, B) show, as for the case of the hydrogenated bilayer, the presence of a thick and diluted layer (47 Å thick and 0.91 of solvent fraction) that is resistant to the several washings used to change contrasts. The structural parameters of the lipid bilayer itself does not change after the interaction with AmB.

In the case of the dPL+S bilayer, the change in reflectivity curves after the interaction with AmB is showed in figure 4.9 (C). The scattering length density profile indicates that there is once again a very diluted layer (37 Å thick, solvent fraction of 0.93). The scattering length density of the tail region decreases significantly to a value of $6.16 \pm 0.02\ 10^{-6}$ $Å^{-2}$.

Therefore, in addition to the AmB islands on the top of the bilayer as described above for the three other systems, the main difference is the lowered scattering length density of the chain region (figure 4.9, D). As for the hPL+S bilayer, this effect might be due to a less dense chain packing or the scattering contribution from AmB molecules. Since it has been shown that AmB tends to contract the chains and leads to a denser chain pack-

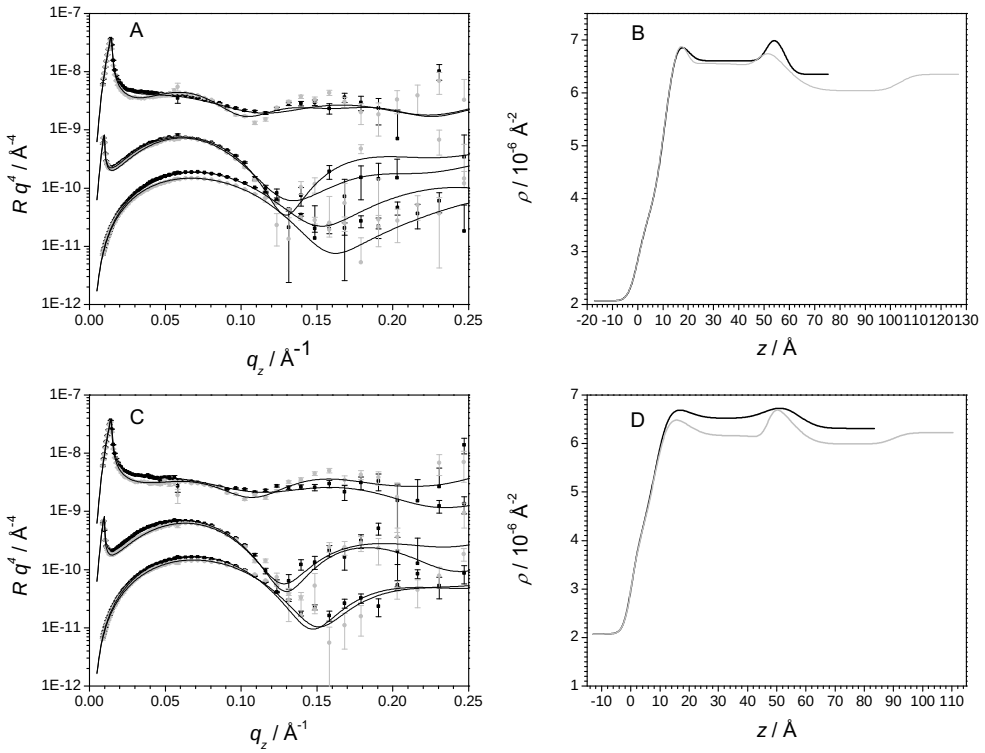

Figure 4.9: Left: Reflectivity curves and corresponding fits from (A) dPL and (C) dPL+S bilayer deposited on a silicon substrate in D_2O, CM4, and H_2O before (black) and after (grey) the incubation of AmB. The curves in CM4 and H_2O are shifted by a factor of 10 and 100 for clarity. Right: Scattering Length Density profiles obtained from the fits of the (B) dPL and (D) dPLS bilayers in D_2O before (black) and after (grey) the incubation of AmB. $z = 0$ at the Si-SiO_2 interface.

ing, the second explanation is more plausible. However, no significant change in headgroup and tail thickness is observed here. The absence of thinning effect could be due to the different fatty acid composition, the deuterated versions being composed of mainly C18:1. The fatty acid composition seems to be an important parameter for the action of AmB, which was already described previously by Cohen [105, 106] who stated that the presence of ergosterol can modulate the amount of channels depending on the fatty acyl composition.

4.4 Conclusions

Amphotericin B is a drug used against fungal infection. It is admitted that its way of action comes from its ability to bind preferentially to ergosterol over cholesterol. However, in the aggregated state which occurs at higher concentration, AmB is also able to interact with cholesterol-containing membranes [111].

This work presents for the first time the structural investigation of AmB incubation with yeast natural lipids. The structure of the planar bilayers before incubation depends on the absence or presence of sterols and the fatty acyl composition. In all bilayers, in presence and absence of sterols, the incubation of AmB results in the apparition of a thick and diluted layer between the subphase and the lipid bilayer. Since the bilayer contains a relatively high fraction of negatively charged lipids, one could assume that AmB is bound to the bilayers by means of electrostatic and Van deer Waals interactions and hydrogen bonds. This additional layer remains there even after abundant rinsing.

In the absence of sterol, AmB is bound only to the outer headgroup region and cannot insert into the hydrophobic part of the membrane. The bilayers containing sterols exhibit different behavior when interacting with AmB. The hydrogenated PL+S get thinner and the thickness of the chain region corresponding to one AmB molecule suggests that it is inserted perpendicularly to the bilayer plane. The incubation of AmB in the deuterated PL+S bilayer presents only a change in chain scattering length density but not in thickness. Since the main variation between hydrogenated

and deuterated PL+S bilayers is the fatty acid composition, it means that the fatty acyl composition of the bilayer is important for the change of structure induced by AmB.

Chapter 5

Interaction of chloroplast main glycerolipids with synthetic intermediates

5.1 Introduction

Plant and algal cells are characterized by the presence of a chloroplast, a specific organelle specialized in the collection and conversion of solar energy into chemical energy, at the basis of the complete nutritional chain. The chloroplast (figure 5.1) is delimited by an envelope made of two membranes: the outer envelope membrane (me) and the inner envelope membrane (mi) and contains a third photosynthetic membrane, in which photosystems are inserted, also called the thylakoids. In one squared meter of leaves, the total surface of photosynthetic membrane is estimate to be around 2.5 ha ($\sim$3 times the surface of a football ground). Chloroplast membranes represent therefore the most abundant biological membrane system on Earth.

Photosynthetic membranes differ from all other cellular membranes by their very low amount of phospholipids (no phosphatidylethanolamine and a low proportion of phosphatidylcholine), an extremely high content of a unique class of galactolipids, i.e. mono- and di-galactosyldiacylglycerol (MGDG, DGDG). Choloroplast membranes also contain small proportions

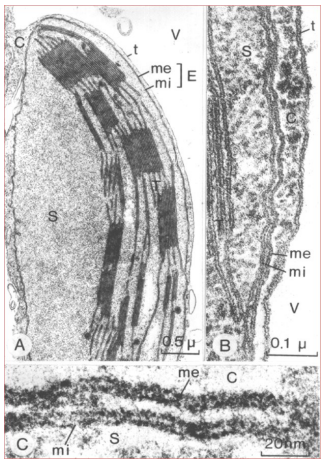

Figure 5.1: Electron micrograph of a chloroplast from spinach. Membranes, mostly containing galactolipids, are shown: me, outer envelope membrane, mi, inner envelope membrane [131].

of phosphatidylglycerol (PG) and sulfoquinovosyldiacylglycerol (SQDG). Their chemical structures are shown in figure 5.2. The main fatty acids are C18:3/C16:3 and C18:3/C18:3 in MGDG and only C18:3/C18:3 in DGDG. The main fatty acids in PG are C16:1 (in trans) /C18:3 and in SQDG are C16:0/C18:3.

These galactolipids are detected in all photosynthetic membranes from cyanobacteria to plant and algae, and thylakoids contain up to 80% of MGDG and DGDG [132]: they constitute therefore the most profuse lipid class on earth [133]. MGDG and DGDG were shown to be critical for the structure and functioning of photosystems and thus for photosynthesis [134]. The biosynthesis of galactolipids occurs in the chloroplast envelope, by a series of 5 enzyme activities (figure 5.3). Enzymes 1 and 2 - called fatty acid acyl transferase 1 and 2 or ATS 1 and 2- esterify two fatty acids (FA1 and FA2) on glycerol-3-phosphate, producing phosphatidic acid (PA). The enzyme 3, a phosphatidic acid phosphorylase or PAP, synthesizes diacylglycerol (DAG).

The enzymes 4, MGDG synthases, synthesizes MGDG from DAG. Different MGDG synthases exist in the chloroplast envelope. MGD1 synthesizes MGDG in the inner envelope membrane [135] while, in conditions of

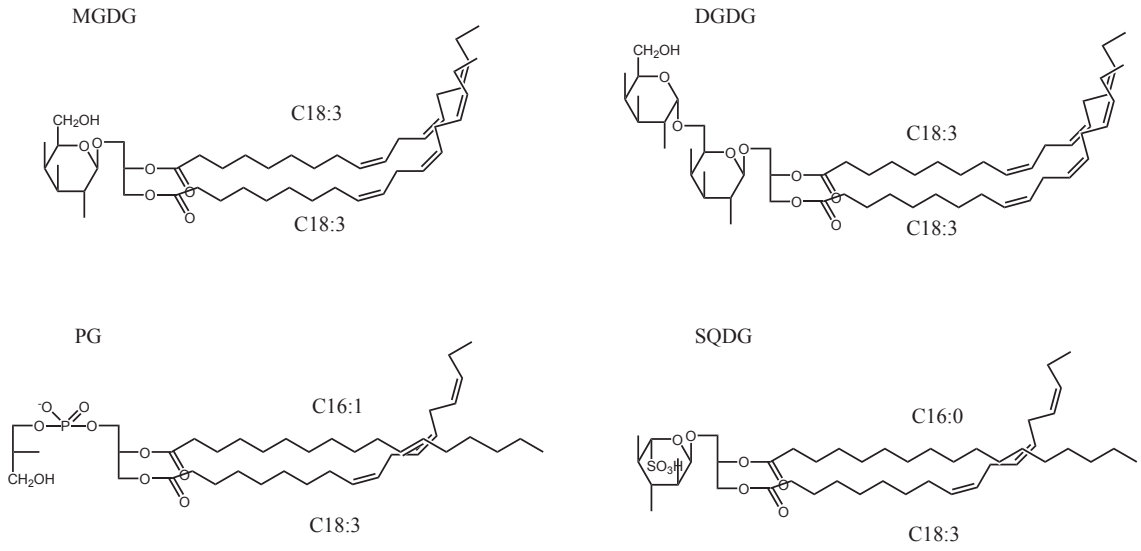

Figure 5.2: Structure of the four glycerolipids constituting the chloroplast membrane. MGDG : mono-galactosyldiacylglycerol, DGDG : di-galactosyldiacylglycerol, PG : phosphatidylglycerol, SQDG: sulfoquinovosyldiacylglycerol

phosphate deprivation, MGD2 and MGD3 synthesize MGDG from DAG in the outer envelope membrane [136]. MGD2 and MGD3 are not expressed in normal conditions.

The topology of this pathway raises critical, and still unresolved questions. Enzymes 1, 2 and 3 are on the inner monolayer of the iem. Enzymes 4 include MGD1 which is on the outer monolayer of the inner envelope membrane and also MGD2 and MGD3 which are located on the outer envelope membrane. Enzymes 5 lie in the outer envelope membrane as well.

In addition, PA is an essential activator of MGD1 and DAG is an inhibitor of enzyme 3 (dashed arrows in figure 5.3). To operate, we must hypothesize that DAG and PA could relocate from the inner monolayer to the outer monolayer of the inner envelope membrane. Reverse relocations should also occur to allow for the incorporation of PA and DAG shown to be transported via chloroplast envelope transporters, and feed other pathways (PA for the CDP-DAG pathway and DAG for the Kennedy pathway for the syntheses of all major membrane glycerolipids).

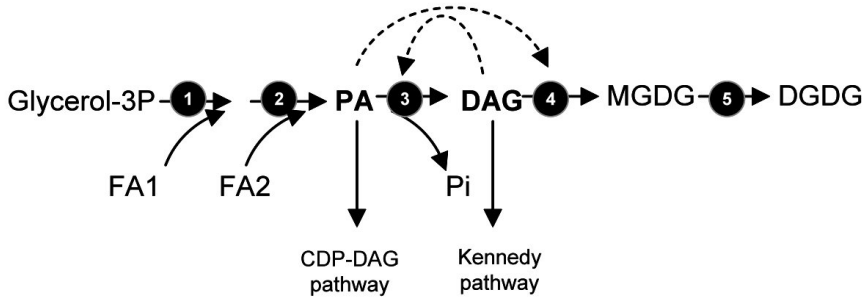

Figure 5.3: Scheme of the synthesis pathway of MGDG and DGDG. Enzyme 1: fatty acid acyl transferases 1, enzyme 2: fatty acid acyl transferases 2, enzyme 3: phosphatidic acid phosphorylases, enzymes 4: MGDG synthases, enzymes 5: DGDG synthases.

Thus, PA and DAG are essential intermediates for the synthesis of chloroplast galactolipids in a pathway which topology requires a specific dynamics of these lipids so they can reach binding and catalytic sites of enzymes. PA and DAG are also intermediates for the syntheses of all other glycerolipids and very well known signal molecules [132].

This system cannot be fully comprehended without understanding how DAG and PA insert in membranes of natural composition (here the chloroplast envelope), addressing the possibility that they could invert their polar head orientation in this bilayer, possibly lying in a flat orientation in the core of the bilayer, as recently shown for cholesterol [137].

This latter hypothesis is essential to confirm in the case of DAG. Finally, the pH being a key factor for PA charges, it is essential to investigate the insertion, orientation and dynamics of PA at various pH of physiological relevance, in particular in the context of the chloroplast where the pH is finely tuned according to the compartment that monolayers face, and to night and day physiological pH. Altogether, the obtained information would provide a piece of knowledge currently lacking to understand one of the most intriguing and important membrane biogenetic processes in nature.

The structure of plant membranes and the location of DAG and PA within them are investigated in this chapter. Lipid components were ex-

tracted from the chloroplast of plants according to a procedure already described [132].

The lipid bilayers were deposited on silicon and sapphire by using the Langmuir-Blodgett and Langmuir-Schaefer (LB-LS) techniques [45]. Two mixtures, close to the natural composition of the photosynthetic membranes, were used.

The effect of DAG on symmetrical bilayer composed of chloroplast lipids was investigated at different concentrations.

The flip-flop of PA in plant membranes from the inner to the outer leaflet was studied at pH = 8 (for the same stroma during the day) and pH = 4 (thylakoids lumen that is acidic because of the proton gradient created by the photosystems).

5.2 Structure of plant lipids mixtures

Before investigating the influence of DAG and the PA flip-flop in plant lipid bilayers, it was necessary to first characterize the structure of the plant membrane. Two different lipid composition were used: a ternary mixture composed of MGDG : DGDG : PG (64:28:8 mol/mol/mol) and a quaternary mixture composed of MGDG : DGDG : PG : SQDG (55:27:9:9, mol/mol/mol/mol). All the bilayers were deposited by LB-LS methods.

5.2.1 Ternary mixture

C18:3 is the main fatty acid in the natural MGDG and DGDG extracts (table 5.1). In terms of amount, C16:3 is the second fatty acid in MGDG and the third in DGDG after C16:0. This very high unsaturation degree is typical of plant lipids. One can notice that the fatty acid composition of PG is different: the amount of C18:3 fatty acid drops to 44%. PG presents 36% of C16:1 (in trans conformation) and 13% of C16:0.

The ternary mixture composed of MGDG : DGDG : PG (64:28:8) was deposited onto a silicon substrate. The pressure - area isotherm shows that the mean molecular area of the ternary mixture of the plant lipid at 37 mN/m is about 120 $Å^2$ (figure 5.4). This large area compared to the area

Table 5.1: Relative fatty acid composition of MGDG, DGDG, PG in the ternay mixture as well as d-DAG and d-PA.

	MGDG	DGDG	PG	d-DAG	d-PA
Molar ratio	64	28	8		
C16:0	1	9	13	9	5
C16:1	0	0	36	3	4
C16:2	0	0	0	1	0
C16:3	17	2	0	3	1
C18:0	1	5	5	3	3
C18:1	0	2	0	57	67
C18:2	2	2	2	20	18
C18:3	79	80	44	3	2

per DPPC molecule at a similar surface pressure can be explained by the presence of highly unsaturated chains increasing the steric repulsion and decreasing the free volume left for the tail. Previous studies reported the compression behaviour of plant lipid monolayers [138, 139] but the area per lipid was not that high at a surface pressure of 30 mN/m. However, the MGDG and DGDG lipids used in these studies contained higher fractions of saturated or mono-unsaturated fatty acid.

After the deposition of a ternary mix bilayer onto a silicon substrate, the reflectivity was measured in H_2O, D_2O and CM4 (contrast matched to $4*10^{-6}$Å^{-2}). Two different models are used to fit the reflectivity curves; using either one or three distinct optical layers (figure 5.5). The one layer model consists of a lipid bilayer depicted as one layer containing inner and outer headgroups and tail regions. In addition to this layer, the system also includes one water layer between the lipid bilayer and the substrate. The three layer model is the same as that used in the other chapters, i.e. the lipid bilayer is divided in three distincts regions corresponding the inner headgroups, the tails and the outer headgroups regions.

The reflectivity data are fitted according to these two models as shown in figure 5.6. The scattering length density curves present a difference in the hydrophobic core region: there is a minimum in the three layers

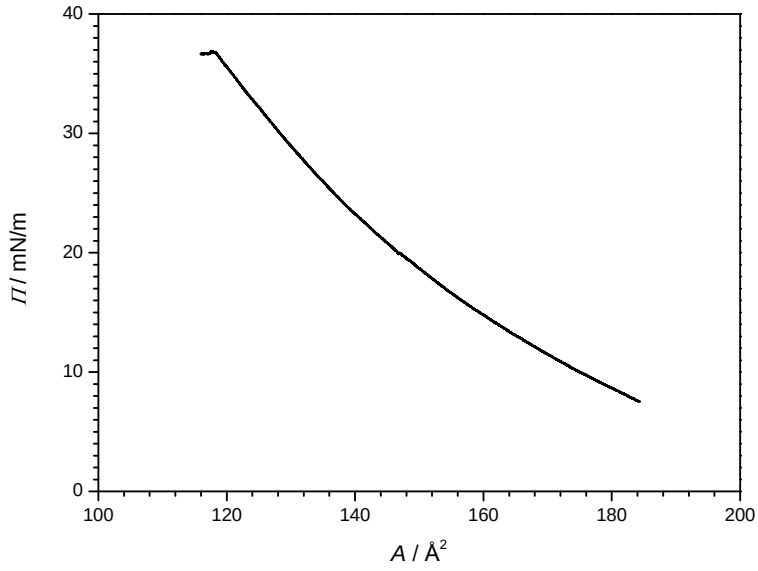

Figure 5.4: Surface pressure - area isotherm of a monolayer composed of a ternary mixed plant lipids.

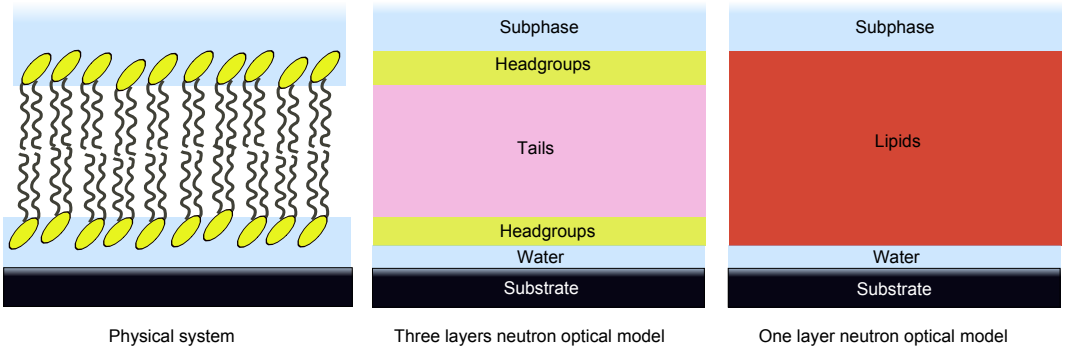

Figure 5.5: Schemes of the models used to fit the data. Left: physical system of a lipid bilayer deposited onto a substrate. Middle: Neutron optical model to represent the lipid bilayer in three separated layers corresponding to the outer and inner headgroups and tails regions. This model is called the three layers model. Right: Neutron optical model to represent the lipid bilayer as one layer, called the one layer model.

model at a distance of around 30 Å from the surface whereas the scattering length density value is constant in the one layer model. χ^2 value which describes the difference between the fits and the experimental data points is 4.2 in the case of the one layer model and 3.8 in the case of the three layers model. However, the errors associated with the parameters obtained from the three layers model are too large to reasonably quantify the bilayer structural properties. These large errors come from the fact that too many parameters are either correlated or anti-correlated.

Interestingly, the overall thickness of the bilayer is 38 Å (table 5.2) and does not change when obtained from the two different models. This thickness has also been found by neutron diffraction (manuscript in preparation). The layer contains 43 % of water but it does not directly reflect the coverage of the bilayer since it includes also the amount of water bound to the hydrophilic headgroups. In any case, the coverage is not high enough to have a strong contribution of the scattering of the bilayer which would allow fitting the data with the three layers model. This relatively bad coverage might come from electrostatic repulsion between the silicon oxide and PG which are both negatively charged.

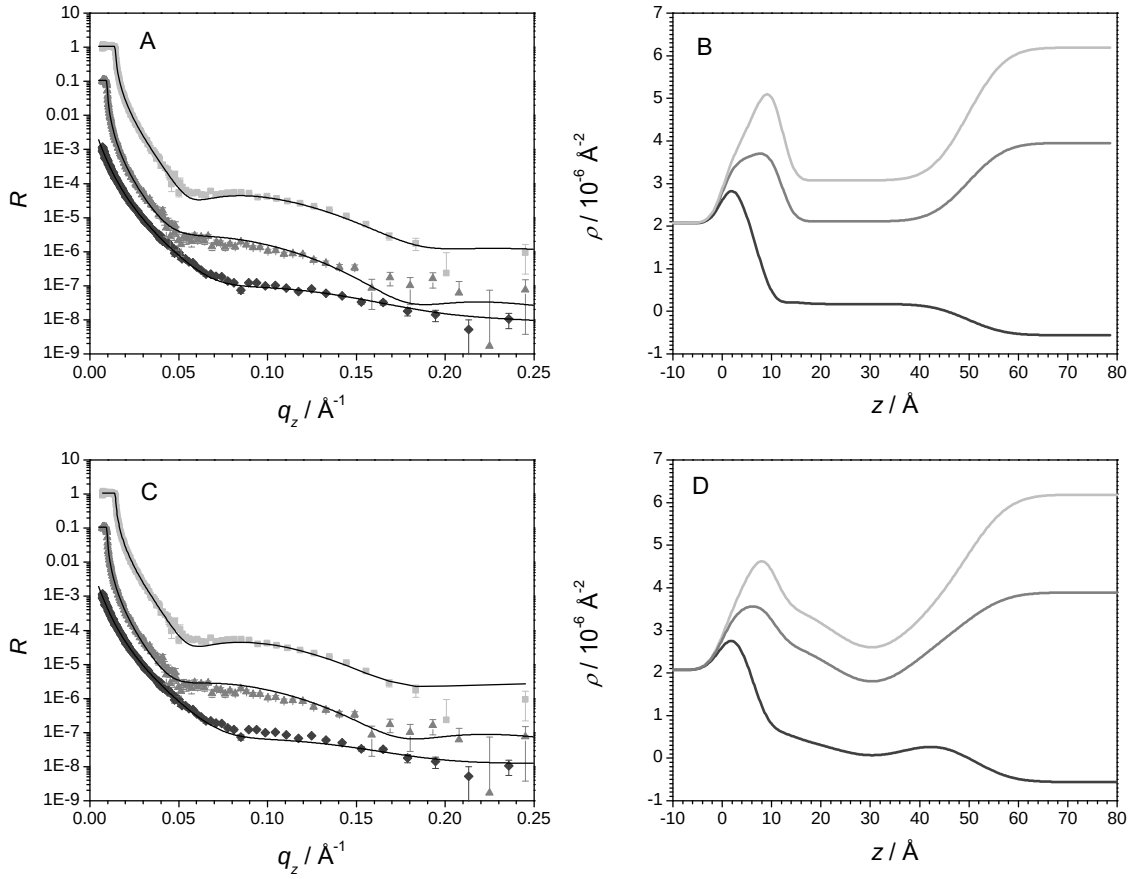

Figure 5.6: Neutron reflectivity curves from a ternary plant mixture deposited on a silicon substrate in D_2O (light grey square), CM4 (grey triangle) and H_2O (dark grey diamond) and the fits corresponding to the (A) one layer model and (C) three layers model. Scattering length density profiles obtained from the fits from the (B) one layer model and (D) three layers model. For clarity, experimental data and fits for CM4 and H_2O measurements are divided by 10 and 100, respectively. $z = 0$ at the Si-SiO_2 interface.

Table 5.2: Parameters describing the ternary mixture bilayer obtained from the fits using the one layer and the three layers models. t = thickness (Å), ρ = scattering length density (10^{-6}Å^{-2}), ϕ = solvent fraction (in percent), σ = roughness (Å). * the scattering length density vary according to the subphase contrast. It is 1.32 10^{-6}Å^{-2} in H_2O, 1.96 10^{-6}Å^{-2} in CM4 and 1.87 10^{-6}Å^{-2} in D_2O.

One layer model

	t	ρ	ϕ	σ
Water layer	5 ± 1	-	100	2 ± 2
Lipid layer	38 ± 1	0.72 ± 0.02	43 ± 1	6 ± 1

Three layers model

	t	ρ	ϕ	σ
Water layer	3	-	100	3
Inner headgroups layer	13	*	42	8
Tails layer	12	-0.04	32	7
Outer headgroups layer	13	*	42	6

5.2.2 Quaternary mixture

Since the bilayer was not well deposited on the silicon substrate, it was decided to use sapphire as substrate. Sapphire presents two advantages: it is positively charged, which should help the deposition of negatively charged lipids and has a scattering length density of 5.7*10^{-6} Å^{-2}, contrasting greatly with the hydrogenated bilayer.

The fatty acid composition of MGDG, DGDG and PG in the quaternary mixture are roughly the same as in the ternary mixture and SQDG contains C16:0 and C18:3 fatty acids in equal proportions (table 5.3).

Interestingly, the surface pressure - area isotherm of the quaternary lipids mixture monolayer (figure 5.7) shows that the lateral surface pressure is 37 mN/m when the mean molecular area is 85 Å^2. This means that the quaternary lipid mixture is able to be more closely packed than the ternary one. This behaviour can be explained by the decrease of the relative amount of unsaturated fatty acids and the increase of saturated fatty acids induced by the presence of SQDG and also by the changes in

Table 5.3: Relative fatty acid composition of lipids in the quaternary mixture as well as in d-DAG and d-PA.

	MGDG	DGDG	PG	SQDG	d-DAG	d-PA
Molar ratio	55	27	9	9		
C16:0	1	7	12	41	7	4
C16:1	0	0	40	1	2	1
C16:2	0	0	0	0	0	0
C16:3	14	5	0	1	0	0
C18:0	0	0	1	1	8	3
C18:1	0	1	1	1	64	72
C18:2	2	2	4	7	17	18
C18:3	81	84	42	48	2	2

intermolecular hydrogen bonds from headgroups.

The reflectivity from the quaternary lipid mixture on sapphire was measured in three different contrasts. The chosen solvent subphases were different from those previously used in order to adapt to the different contrasts given by the sapphire substrate. It was decided to use D_2O, H_2O, a mixture of 75 v% of D_2O and 25 v% of H_2O (called C75%) and a mixture of equally mixed volumes of D_2O and H_2O (called C50%).

The effect of the bilayer on the reflectivity curves is evident when compared to the reflectivity from a bare sapphire in D_2O (see figure 5.8). The scattering length density of sapphire is so close to that of D_2O that, at $q_z \geq 0.02$ Å^{-1} for bare substrate, the reflectivity drops to values lower than 10^{-6} which cannot be dissociated from the background. On the contrary, when the lipid bilayer is deposited on the substrate, the reflectivity profile decreases more gradually to reach the background at a q_z value of 0.20 Å^{-1}. This arises from the difference of scattering length density between the hydrogenated layer and the subphase, which is high enough to observe such a different reflectivity signal.

Once again, it is possible to fit the reflectivity data with two models: one layer model and three layers model (figure 5.9) which lead to the same χ^2 value of 7. The lipid bilayer thickness is 38 Å obtained from the fits cor-

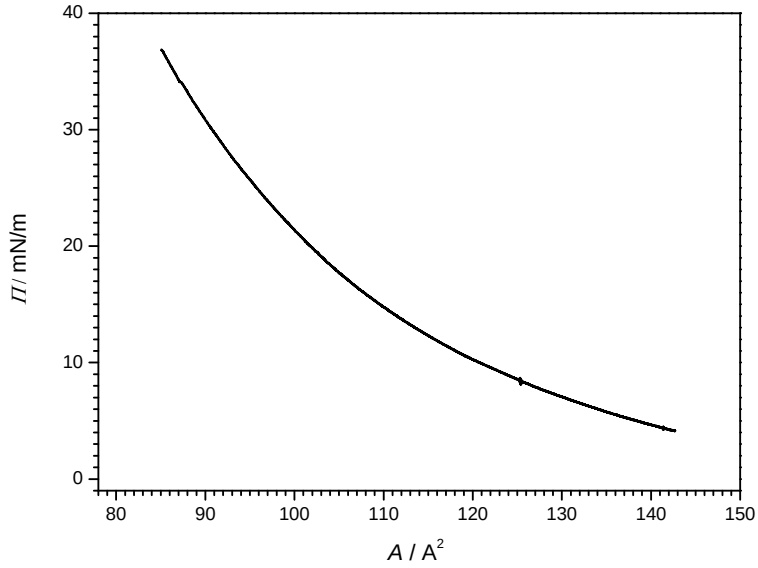

Figure 5.7: Surface pressure - area isotherm of a monolayer composed of a quaternary mixed plant lipids.

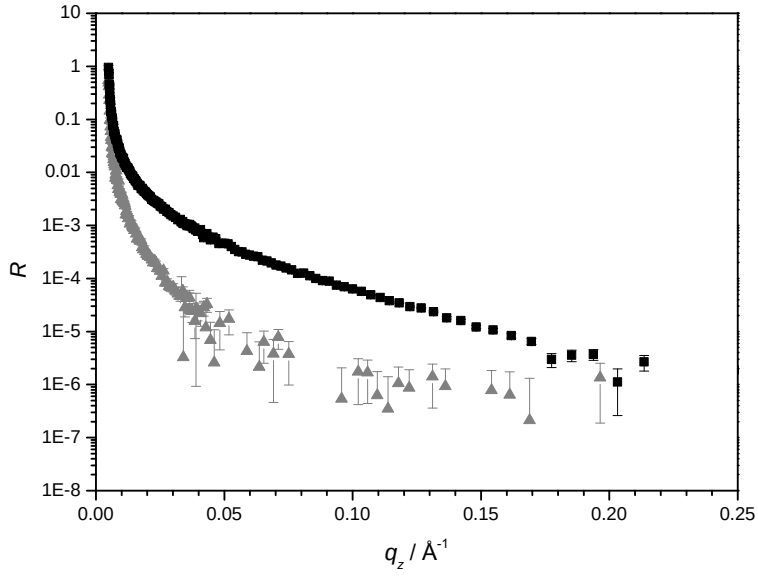

Figure 5.8: Neutron reflectivity curves from a quaternary plant mixture deposited on a sapphire substrate (black square) and from a bare sapphire substrate (grey triangle) in D_2O.

Table 5.4: Parameters describing the quaternary mixture bilayer obtained from the fits using the one layer and the three layers models. t = thickness (Å), ρ = scattering length density (10^{-6}Å^{-2}), ϕ = solvent fraction (in percent), σ = roughness (Å). * the scattering length density vary according to the subphase contrast. It is 1.8 10^{-6}Å^{-2} in H_2O, 2.70 10^{-6}Å^{-2} in C75% and 3 10^{-6}Å^{-2} in D_2O.

One layer model

	t	ρ	ϕ	σ
Water layer	9 ± 1	-	100	3 ± 3
Lipid layer	28 ± 1	0.70 ± 0.03	28 ± 3	7 ± 1

Three layers model

	t	ρ	ϕ	σ
Water layer	5	-	100	5
Inner headgroups layer	11	*	54	5
Tails layer	16	-0.12	22	5
Outer headgroups layer	11	*	54	5

responding to the three layers model while it is 28 Å from the one layer model. The former value is in agreement with what has been found by X-ray diffraction from stacks of plant bilayers [140]. However, the lipid bilayer thickness obtained from the one layer model is smaller than what have been measured by neutron diffraction (manuscript in preparation). This discrepency might comes from the effect of sapphire substrate which is positively charged. One can notice the large roughness from the one layer model (see table 5.4). This roughness can come from the presence of C16:0 enriched SQDG which leads to an inhomogeneous fatty acid composition or from the polar headgroups heterogeneity.

5.3 Influence of diacylglycerol on structure of plant bilayers

The effect of diacylglycerol on ternary and quaternary plant membranes was investigated by neutron reflectometry. Monolayers containing plant

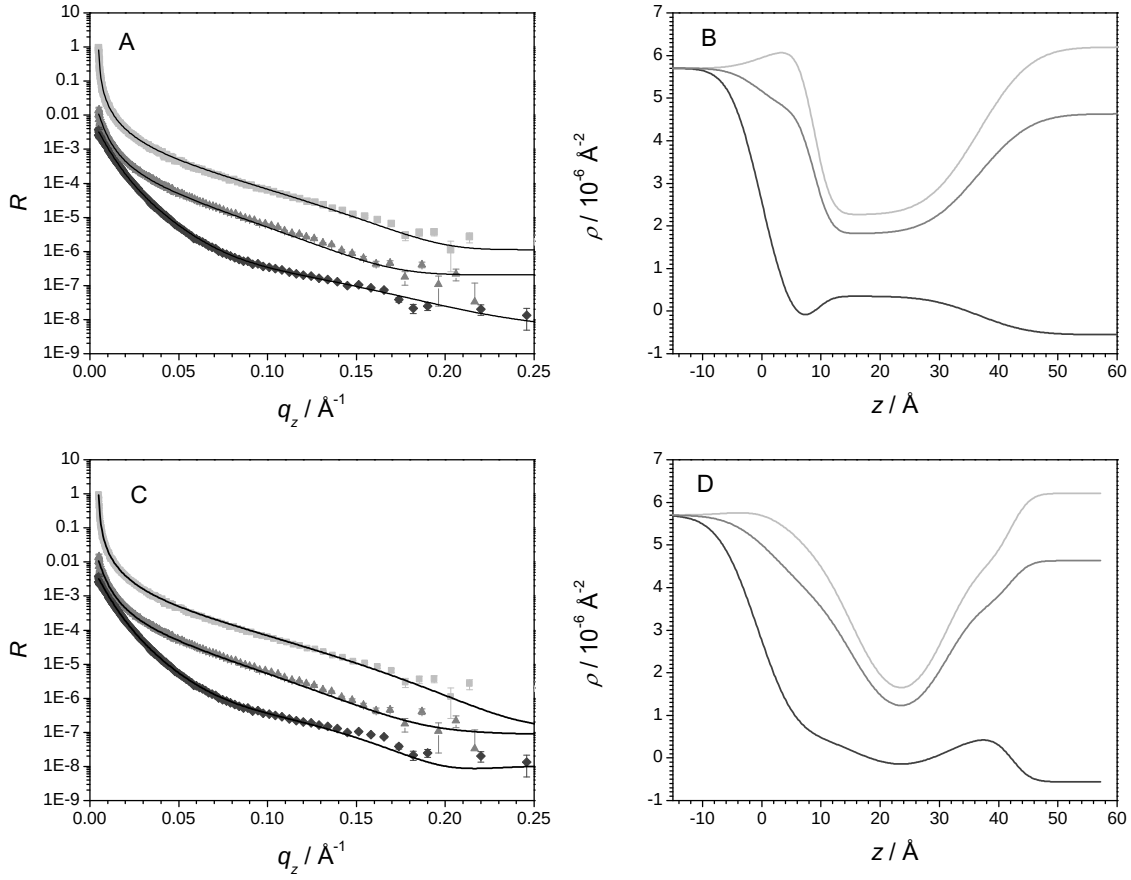

Figure 5.9: Neutron reflectivity curves from a quaternary plant mixture deposited on a silicon substrate in D_2O (light grey square), C75 (grey triangle) and H_2O (dark grey diamond) and the fits corresponding to the (A) one layer model and (C) three layers model. Scattering length density profiles obtained from the fits from the (B) one layer model and (D) three layers model. For clarity, experimental data and fits for C75 and H_2O measurements are divided by 10 and 100, respectively. $z = 0$ at the sapphire-water interface.

Table 5.5: Parameters describing the ternary mixture bilayer containing 5% DAG obtained by fitting with the one layer model. t = thickness (Å), ρ = scattering length density (10^{-6}Å^{-2}), ϕ = solvent fraction (in percent), σ = roughness (Å).

	t	ρ	ϕ	σ
Water layer	15 ± 1	-	100	3 ± 2
Lipid layer	34 ± 1	0.39 ± 0.01	16 ± 2	5 ± 1

lipids at different perdeuterated DAG concentrations (5 and 10 mol% with respect to the total lipid concentration) were spread at the air-water interface in order to be deposited onto silicon or sapphire substrates by LB - LS techniques.

5.3.1 Influence of DAG on ternary lipid mixture

The ternary mixture bilayer was deposited onto a silicon substrate and contained 5% of deuterated DAG in both leaflets. In order to compare the bilayer structure to that of DAG-free ternary mixture, it was deposited onto a silicon substrate. The presence of 5% DAG drastically modifies the surface pressure - area isotherm of the ternary mixture monolayer (figure 5.10). The main effect is the enhanced mean molecular area at which the monolayer is deposited on the substrate. The effect could be due to the presence of DAG intercalating between the tails belonging to plant lipids. It has been already shown that DAG, as branched analogs of phospholipids [141, 142], increases the spacing between phospholipid headgroups [143, 144].

The reflectivity from the DAG-containing bilayer was measured in D_2O, CM4 and H_2O (figure 5.11). The first striking difference with the pure ternary mixture is the water layer thickness between the lipid layer and the substrate which increases up to 15 Å (table 5.5). Another difference is the decreased thickness of the bilayer: 34 Å in presence versus 38 Å in absence of 5% DAG. Finally, the scattering length density is lowered; this is unexpected since the DAG molecules inserted within the bilayer are deuterated.

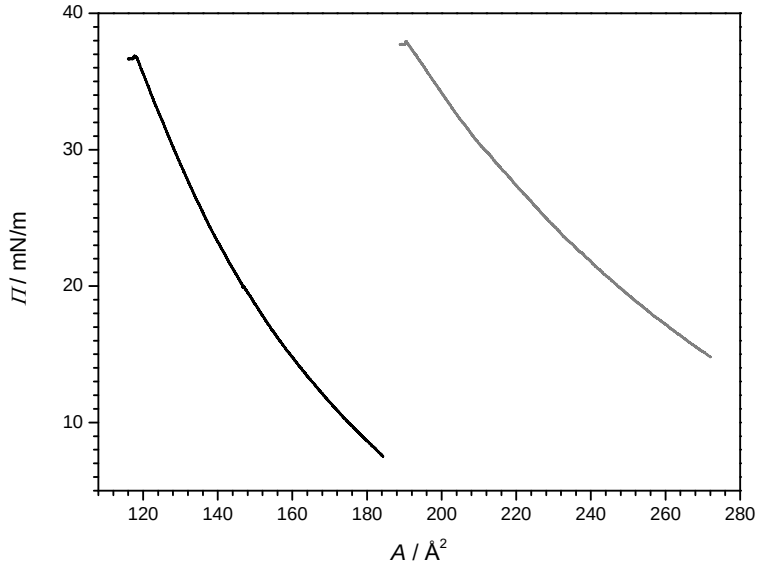

Figure 5.10: Surface pressure - area isotherm of a monolayer composed of a ternary mixed plant lipids in absence (black) and in presence (grey) of DAG.

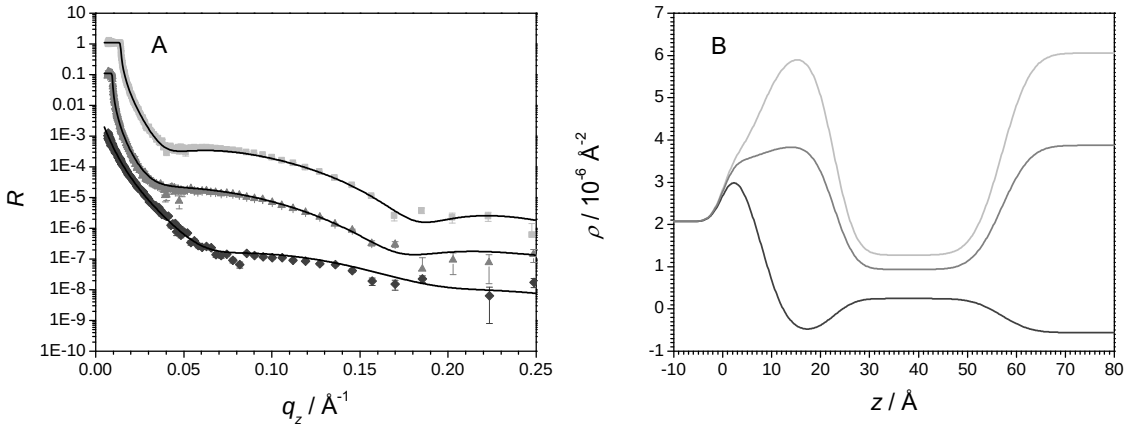

Figure 5.11: Left: neutron reflectivity curves from a ternary plant mixture containing 5% DAG deposited on a silicon substrate in D_2O (light grey square), CM4 (grey triangle) and H_2O (dark grey diamond) and the corresponding fits. Right: scattering length density profiles obtained from the fits. For clarity, experimental data and fits for CM4 and H_2O measurements are divided by 10 and 100, respectively. $z = 0$ at the Si-SiO_2 interface.

The increased spacing induced by the presence of DAG parallel to the lipid chains could explain the structural parameters observed by neutron reflectivity. Since the area per headgroup gets larger, the headgroups are less compressed and could be flattened at the hydrophobic - hydrophilic interface. This would then result to a decrease of the bilayer thickness. Moreover, the negative charges carried by PG molecules become more exposed and the electrostatic repulsion between the lipid bilayer and the partially negative substrate becomes stronger and leads to a thicker water layer. The most surprising result is the decreased scattering length density although deuterated material was added to the lipid bilayer. Since the model includes both headgroups and tail regions in one layer, the modified packing of each part can contribute to the scattering length density change.

5.3.2 Influence of DAG on quaternary lipid mixture

The influence of DAG on lipid bilayers containing the quaternary lipid mixture deposited on sapphire substrates was also investigated. The DAG concentrations used in this work were 5 and 10 mol%. The surface pressure area isotherm shows that, as in the case of the ternary mixture but in a lesser extent, the presence of DAG tends to increase the mean molecular area for a given surface pressure, meaning that DAG once again acts as a spacer (fig. 5.12). One can note that the effect of DAG on the area per headgroup at high surface pressure is much less pronounced in the quaternary mixture than in the case of the ternary mixture.

The reflectivity from the 5% and 10% DAG-containing quaternary mixtures were measured in three different contrasts. The reflectivity from the three lipid bilayers (0, 5 and 10% DAG) in D_2O does not present particularly different features (figure 5.13 A). However, the scattering length density profiles show that the 10% DAG-containing lipid bilayer is thinner than the two others. By looking more carefully in the values of the fitted parameters, we can see that this difference in thickness mainly comes from the water layer between the substrate and the lipid bilayer (table 5.6). The water layer thickness decreases when more DAG is added in the bi-

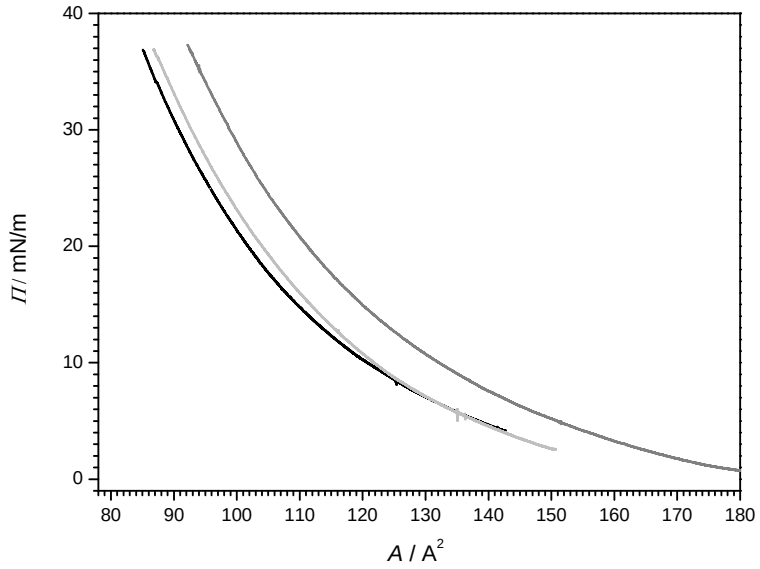

Figure 5.12: Surface pressure - area isotherm of a monolayer composed of a quaternary mixed plant lipids in absence (black) and in presence of 5% (light grey) and 10 % (grey) DAG.

layer. This result is consistent with what has been described in the case of the ternary bilayer; the electrostatic interaction between the positively charged sapphire substrate and negatively charged lipid is favourable. Since DAG molecules intercalate between the tails, this results in an enhanced area per headgroup which makes the charges more accessible and increases the electrostatic attraction with the substrate.

Surprisingly, the scattering length density values of the lipid layer as a function of the relative amount of perdeuterated DAG are not monotonic. Since the thickness values of the water and lipid layers are identical in the 0 and 5% DAG-containing lipid bilayer, one can hypothesize that the headgroups conformation is kept the same in both systems. When 10 % of DAG are added to the bilayer, the differences observed from the surface pressure - area isotherm and from the parameters obtained from the fits indicate that a change of conformation happened. The drop in scattering length density of the lipid layer can come from the change of conformation of the bilayer.

However, according to the parameters listed in the table 5.6, the lipid

layer itself does not seem being affected by the presence of DAG. This surprising result is also visible from the surface pressure - area isotherm (figure 5.12) because the presence of DAG influences much less the isotherm than that of the ternary mixture.

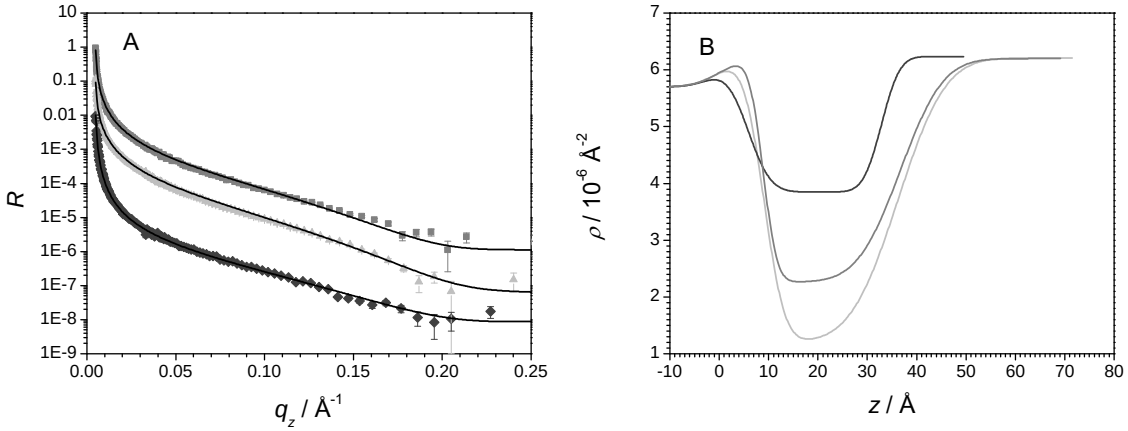

Figure 5.13: A: neutron reflectivity curves from a quaternary plant mixture deposited on a sapphire substrate in D_2O in absence (grey square) and in presence of 5% (light grey triangle) and 10% (dark grey diamond) of DAG and the corresponding fits. For clarity, experimental data and fits for 5% and 10% DAG-containing bilayers are divided by 10 and 100, respectively. B: scattering length density profiles obtained from the fits from the quaternary mixture in absence (grey) and in presence of 5% (light grey) and 10 % (dark gray) of DAG. $z = 0$ at the sapphire-water interface.

Table 5.6: Parameters describing the quaternary mixture bilayer in absence and in presence of 5% and 10% of DAG obtained by fitting the data with the one layer model. t = thickness (Å), ρ = scattering length density (10^{-6}Å^{-2}), ϕ = solvent fraction (in percent), σ = roughness (Å).

0% DAG

	t	ρ	ϕ	σ
Water layer	9 ± 1	-	100	3 ± 3
Lipid layer	28 ± 1	0.70 ± 0.03	28 ± 3	7 ± 1

5% DAG

	t	ρ	ϕ	σ
Water Layer	10 ± 1	-	100	3 ± 2
Lipid Layer	27 ± 1	1.08 ± 0.01	< 5	7 ± 1

10% DAG

	t	ρ	ϕ	σ
Water Layer	6 ± 1	-	100	4 ± 2
Lipid Layer	27 ± 2	0.51 ± 0.04	58 ± 3	7 ± 1

5.4 Phosphatidic acid flip-flop across plant bilayers

The flip-flop mechanism of phosphatidic acid (PA) from the inner leaflet to the outer leaflet was investigated by neutron reflectometry. The bilayers were prepared asymmetrically by the LB - LS techniques, where one leaflet contained perdeuterated PA in addition to the plant lipids.

5.4.1 Ternary mixture

The reflectivity from an asymmetrical bilayer made of ternary lipid mixture plus 10% of deuterated PA in the outer leaflet deposited on silicon in H_2O was measured at time = 0; 3; 6 and 9 hours after the deposition (figure 5.14). The reflectivity curves measured after six hours are identical. The reflectivity was eventually measured in D_2O and CM4 after the fourth kinetic measurement in order to a have a full characterization of

the lipid bilayer in the final state. Fitting the final reflectivity curves revealed that the lipid bilayer was actually completely desorbed from the substrate. Therefore, the change of reflectivity curves as a function of time was related the desorption of the bilayer and the contribution of the structural change induced by PA flip-flop is too small to be observed.

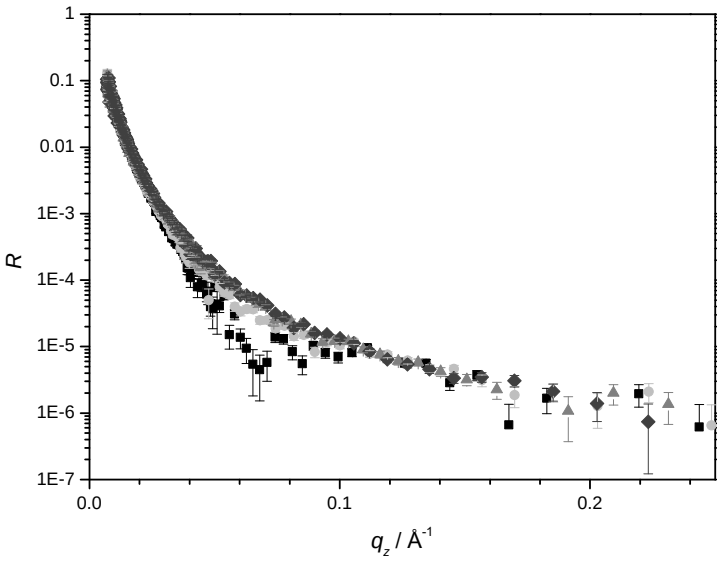

Figure 5.14: Neutron reflectivity curves from a ternary plant mixture deposited on a sapphire substrate in H_2O at time = 0 (black square), t = 3 hours (light grey circle), t = 6 hours (grey triangle), t = 9 hours (dark grey diamond).

5.4.2 Quaternary mixture

Since the bilayer desorption could happen because of the repulsive electrostatic interaction between the negatively charged headgroups and the negatively charged substrate, the quaternary mixture was deposited on positively charged sapphire substrate to avoid such phenomenon. As explained in the introduction, the PA flip-flop from the inner to the outer monolayer was investigated at different pH (4 and 8) to mimic conditions in different compartments of the plant cell. The pH was adjusted both in all the solutions in contact with the bilayers during the measurements

and in the Langmuir trough during preparation. Therefore, the bilayers always experienced the same pH during deposition and measurements.

The lipid bilayer was prepared at pH 4 and several kinetics measurements were carried out in D_2O (figure 5.15 left). The four first kinetics measurements (i.e. from 40 minutes to 3 hours 30 minutes) were done at the first angle only in order to investigate the evolution of the reflectivity at short time scale. The fifth reflectivity measurement was done over the whole q_z-range, then again the fourth following measurements were done at the first angle only. Eventually the very last measurement was also carried out over the whole q_z-range. The arrow shows the evolution of the reflectivity curves and the solid line is the reflectivity arising from a bare sapphire substrate in D_2O. The evolution of the reflectivity data can be fitted by increasing the water content in the lipid layer, which means that the lipid bilayer also gradually desorbs from the substrate in function of time. The same feature is observed at pH = 8 (figure 5.15 right), the reflectivity curves are slowly shifted toward lower intensity values. It is worth noting that the shift occurs at larger time scales at pH 8 than at pH 4. This is probably due to the deprotonation of PA in alkaline medium that by increasing the proportion of negatively charged lipids within the bilayer leads to a stronger attraction between the substrate and the bilayer and slows down the desorption.

5.5 Discussion and conclusions

The structural parameters, such as thickness and roughness, of ternary and quaternary lipid mixtures deposited onto a substrate to form bilayers were obtained. Unlike the models used in the previous chapters, a three layers model (that is a model where the headgroups and chain regions can be distinguished) let too many parameters free leading to large parameter uncertainties. In the case of the ternary mixture, using a three layers model or a one layer model give the same lipid layer thickness of 38 Å. This thickness is consistent with the thickness of plant membrane stacks determined by diffraction [140, 145]. The water layer between the lipid layer and the substrate is 5 ± 1 Å, which corresponds to a layer as thick as

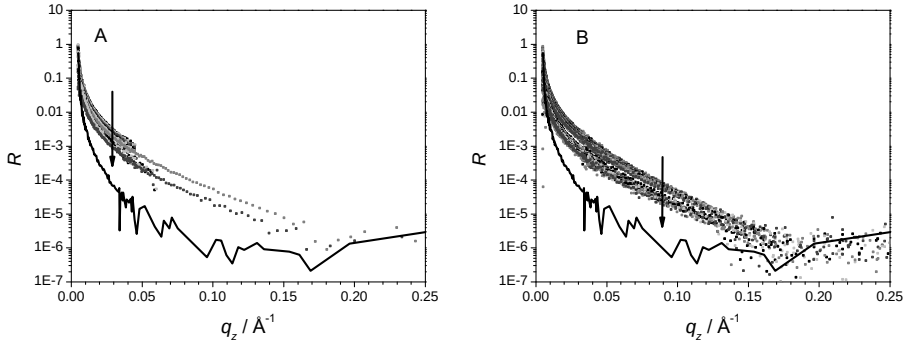

Figure 5.15: Left: Neutron reflectivity curves from a quaternary plant mixture containing 10% of d-PA in the inner leaflet deposited on a sapphire substrate in D_2O at (left) pH = 4 and (right) pH = 8. The scattered points represents the different curves which were measured at different times from (left) 40 minutes to 25 hours and (right) from 2 hours to 45 hours. The arrow shows the evolution of the reflectivity in function of time. The line correspond to the reflectivity arising from a bare sapphire in D_2O.

two water molecules.

For the quaternary mixture, the two models do not result in the same lipid layer thickness. Using the one layer model gives a lipid layer thickness of 28 Å which is 10 Å lower than that found with X-ray diffraction on membrane stack. However, it is worth stressing that the water layer thickness is of 9 Å, which is larger than the water layer associated to the ternary mixture. It is possible that this water layer is not made only of bulk water but also includes the water shell bound to the headgroups. Therefore the boundary between inner headgroups and water layer could not be clearly defined. Moreover, this small thickness can also come from a substrate effect. The negatively charged lipid bilayer was deposited on positively charged sapphire. Therefore the bilayer might become thinner because of the favourable electrostatic interactions which are not present in system composed of stacks of membranes.

It has been shown that the structure of the lipid bilayer is highly dependent on the relative proportion of MGDG and DGDG. Increasing the proportion of the former gives an inverse hexagonal phase while the latter

tend to form a lamellar phase [145, 146]. This is due to the shape of the different glycerolipids. The shape is considered as cylindrical and favours the bilayer structure if the cross section of the headgroup is similar to the cross section of the tail [147] which is the case of DGDG. When the cross section of the headgroup is smaller than the tail cross section, as it is for MGDG, the lipid has the shape of a cone and the formation of inverse hexagonal phase is favoured. In solution, the ternary mixture forms inverse hexagonal phase and the quaternary mixture forms lamellar phase (manuscript in preparation).

One has to highlight the pretty low lipid coverage onto the substrate, lower than 80 %. This low lipid coverage can be due to the difficulty to deposit a lipid bilayer in fluid phase by means of LB - LS techniques. In the case of model membranes, lipid deposited in the gel phase give stable and higher coverage layers than lipids in the fluid phase. Since the lipids used in this work possess a high unsaturation degree (see tables 5.1 and 5.3), it is reasonable to assume that they were in fluid phase while being deposited.

It is known that DAG induces the formation of hexagonal phases when mixed with DMPC, depending on the temperature and DAG concentration [148, 149]. De Boeck and Zidovetski have studied the interaction of DAG with DPPC bilayers by means of ^{2}H and ^{31}P NMR [150]. They observed that saturated DAG can induce lateral phase separation that was not observed with unsaturated DAG. However, unsaturated DAG imposes a restriction in the fluctuation of the DPPC tails due to the smaller volume of DAG headgroups which forces a closer contact between side chains. Moreover, unsaturated DAG can induce the formation of non lamellar phases when being present at concentrations $\geq$ 25 mol%. Due to their natural tendencies to form non lamellar phase, the ternary and quaternary mixtures are likely to be close to the hexagonal phase transition even at 5 % of DAG concentration.

The presence of d-DAG in the ternary or quaternary mixture monolayers impacts the surface pressure - area isotherm as it increases the area per lipids. In this perspective, the tails belonging to DAG are probably parallel to the ones belonging to the plant lipids. If DAG was lying on the top

of the lipid monolayer in the air phase, such a difference in the area per lipids would not be expected.

From the structural point of view, the presence of 5% DAG in the ternary mixture makes the plant membrane slightly thinner, the thickness being 34 Å in presence of DAG instead of 38 Å in absence of DAG. This finding is in agreement with the fact that DAG molecules lie parallel to the plant lipid tails, leading to an increase of the area per lipid and a reduction of the thickness to keep the volume constant. On the contrary, if DAG was located deeply in the core of the bilayer the thickness would increase.

The presence of 5 mol% and 10 mol% DAG in the quaternary mixtures does not impact the thickness of the lipid bilayer. This result is also reflected by the smaller mean molecular area measured with the Langmuir trough in presence of DAG. By adding 10 mol% of DAG, the area per lipid at 37 mN/m increases of 5 $Å^2$ only (figure 5.12). Interestingly, the water layer thickness decreases when DAG concentration increases. This finding supports the hypothesis that DAG molecules influence the conformation of the lipid headgroups and make the negative charges more accessible. The very large amount of water in the 10 mol% DAG-containing bilayer shows the poor lipid coverage onto the substrate. This low efficiency in lipid coverage can be explained by the formation of non lamellar phases induced by the presence of DAG.

The figure 5.16 depicts the effect of the presence of DAG on ternary and quaternary mixtures systems. When DAG is added to the ternary bilayer, the negative charges carried by the polar headgroups become more accessible, creating a repulsive electrostatic interactions between the headgroups and the negatively charged susbtrate. On the other hand, the quaternary mixture was deposited on sapphire, a positively charged substrate. Therefore, the presence of DAG has the opposite effect, because the charges accessibility creates favourable electrostatic interactions, decreasing the water layer thickness.

The initial goal was to find if DAG can lie in the hydrophobic core in the plane of the bilayer in order to be available to the enzyme 4, as shown in figure 5.3. From our results, it seems that DAG rather lies upward with its chains parallel to the plant lipid tails. Indirect observation,

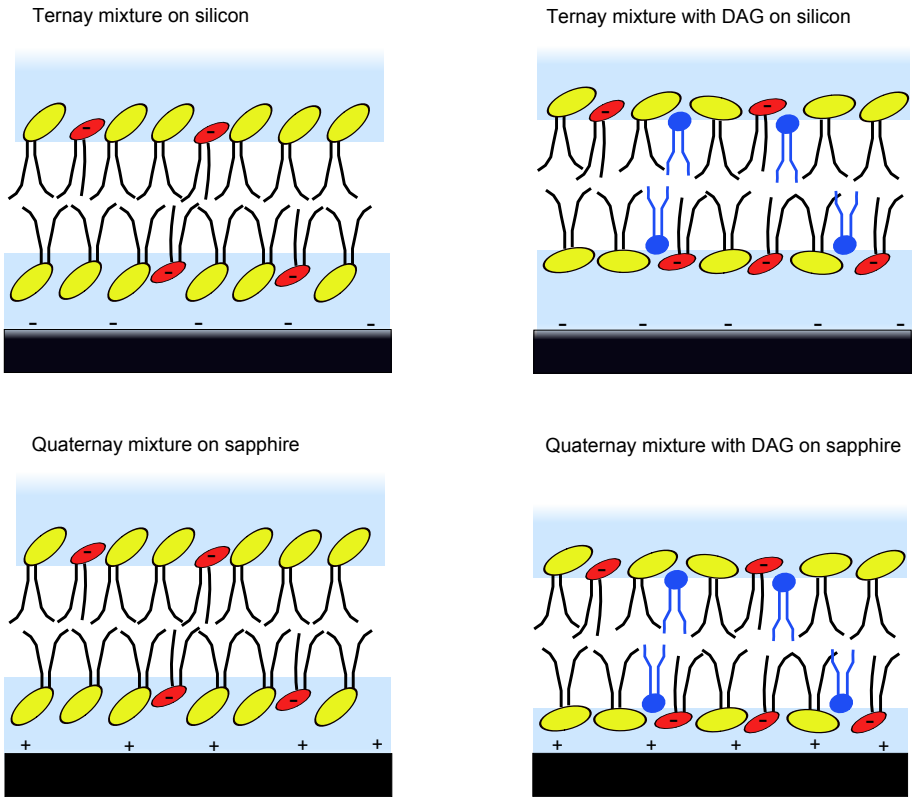

Figure 5.16: Schematic representation of a plant lipid bilayer containing neutral (yellow) and negatively charged (red) lipids in absence (left) and in presence (right) of DAG (in blue) onto negatively or positively charged substrates. When DAG is present within the bilayer, the area per head-group is bigger, which leads to a decrease in bilayer thickness and to more exposed charged lipids due to electrostatic repulsion to the surface that causes an increase the water layer sandwiched between the lipid bilayer and the substrate. The opposite effect is seen for the quaternary mixture because the bilayer was deposited on a positively charged sapphire.

such as water layer thickness, shows that it influences rather the conformation of the headgroups and, by extension, the charges carried by them. DAG molecules are probably not fixed in this conformation; it has been shown by means of NMR that the DAG transbilayer movement has a rate of 60 s^{-1} ($t_{1/2}$ = 10 ms) which means that the phenomenon is orders of magnitude faster than that of phospholipids [151]. Other values taken from other studies lie in the range from a few seconds [152] to one minute [153]. Since the typical measurement time for neutron reflectivity to cover a q_z range from 0 to 0.25 $Å^{-1}$ in Time of Flight mode in one contrast is about one hour, it was not possible to "catch" DAG in a specific conformation and the scattering length density profiles derived from the fits reflect rather the averaged state of the bilayer in time-scales of the order of the hour.

The study of the flip-flop of PA across the bilayer is challenging because we observe that the bilayer is not stable and slowly desorbs from the substrate. On silicon, the bilayer was prepared by incorporating PA in the outer leaflet. Since PA has a cone shape similar to MGDG, it tends to favour the formation of vesicle and, consequently, the desorption of the planar bilayer from the substrate.

On sapphire, the bilayers were prepared by incorporating PA in the inner leaflet in order to prevent the desorption. The rate of desorption can be modulated by the pH of the subphase. Decreasing the pH of the subphase brings more charge which can partially neutralize the phosphate group. Therefore, the attractive electrostatic interaction is weaker at pH = 4 than at pH = 8 which explains why the bilayer desorbs faster. A symmetric membrane containing 5% of PA in both leaflet was prepared but was not stable onto a sapphire substrate; the bilayer contained about 70 % of water (not shown here). This destabilization effect does not happen in quaternary mixture containing 5% of DAG. This effect can come from the addition of charge carried by PA. Besides, the cone shapes of DAG and PA may also not be exactly similar which would explain the destabilization effect observed in the PA-containing membrane and not in the DAG-containing membrane.

Chapter 6

Interaction of resveratrol with model membrane

6.1 Introduction

Consumption of saturated fat, cholesterol, total fat and caloric intake is correlated to a high rate of coronary disease [154]. In France, however, mortality from heart coronary disease is much lower than the one in other western countries although the caloric fat intake is equivalent [155]. This discrepancy is known as the French Paradox. It was postulated to be due to frequent but low-to-moderate consumption of red wine, accomplished by a diet with minor use of mammal fat or meat but of olive oil and fish instead, and frequent rations of fresh fruit, especially grapes, or tomatoes.

The beneficial effects of food antioxidants for health stabilization and even for healing are very diverse. Polyphenols are the natural antibiotics of plants [156–161]; they are automatically taken up by plant based food [162–165], though to different extent depending on the details of the diet. Among the natural polyphenolic antioxidants, the red wine ingredient resveratrol [166–168] is already widely discussed in medicine and food industry for its beneficial health effects [169, 170]. Its positive effect for the cardiovascular system was first evidence [171–175]. Medical research resulted in about 2000 scientific publications during the last 5 years on the medical impact of resveratrol, and trans-resveratrol can be readily bought

as food suppliant or pharmaceutical [176].

Reports on the positive impact of resveratrol cover many subject matters: skin damage after excessive sun exposure is reduced [177, 178], the general anti-inflammatory defense in humans is enhanced [179–182]. Resveratrol has a regulating effect on adipositas [183, 184]. Most prominent are results on its suppressing anti-carcinogenic effect [185–190], which gives a chemo-protective role [188, 189] to the daily diet and makes it an additional tool in post-operative treatment. Resveratrol is a important topic in the discussion of prevention [191–194] and even partial reversal of neurodegenerative diseases [194–196]. Still, there are only few basic biophysical studies [197–204] that might give access to working mechanisms and to a deeper understanding on the details of the action of this molecule [192, 202, 203].

Resveratrol (res; 3,4',5-trihydroxystilbene, see figure 6.1) is naturally synthesized as a trans-stilbene by several species of plants. It has antioxidant properties and is considered as a natural antibacterial protective. Trans-resveratrol is a slightly fluorescent [205] quite small (M_W = 229 g/mol), weakly amphiphilic molecule. The resonant cis-form can be boosted by UV light absorption but the trans-form is the low energy stable state [206, 207]. The extent of membrane activity possibly varies among trans- and cis-resveratrol. A hint about differential recognition of the two isomers can be extracted from the results of a molecular dynamics simulation that explored the specific binding of the molecule to the human estrogen receptor-alpha [208]. Specific binding has been reported for some systems [177, 198, 209–211] but the molecular structure is most suggestive of unspecific interaction properties with regards to biomembranes.

The specific interaction of resveratrol with lipid bilayers interfaces might be important for its bioactivity. The few existing biophysical studies so far are contradictory about the way resveratrol induces structural changes in the membrane [169, 174] as well as about its mechanism of action as an antioxidant. Indeed, its antioxidant properties could result from its ability to scavenge radicals [212, 213] or be indirect by rendering the oxidized membrane fluid [202, 214]. So far only few experimental studies on the interaction of polyphenols with pure lipid membranes have been con-

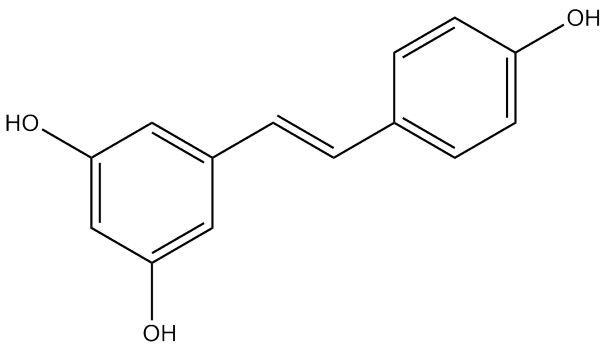

Figure 6.1: Chemical structure of resveratrol.

ducted [201–204]. The location of the molecule res within the membrane is still controversial [201–204]. Most probably, the molecule sits at the interface between the lipid headgroup interface and the chains (at the glycerol level), and there it might have an impact on the interfacial structure and stability as well as on chain conformation and bilayer fluidity.

This chapter deals with the effect that resveratrol has on host model membranes of di-palmitoyl-phosphatidylcholine (DPPC). Neutron reflectometry was used to investigate the structure of supported lipid layers that were equilibrated after addition of the guest molecule.

6.2 Effect of resveratrol on the surface pressure profile of a monolayer

The effect of resveratrol incorporated in DPPC layer was first investigated by compression isotherms (see figure 6.2). Under lateral compression of the monolayer, DPPC molecules are in the so-called liquid expanded phase up to a molecular area of 60 $Å^2$ and a surface pressure of 9.5 mN/m. Then the molecules enter a coexistence of liquid condensed liquid-expanded phases, which results in a plateau on the isotherm. From a molecular area of 47 $Å^2$, molecules are in the liquid condensed phase, which can be detected by a much steeper slope on the isotherm. When resveratrol is inserted in the monolayer before compression, it has two effects on the plateau of the isotherm. As first effect, it induces a broader plateau. The

second effect is the lowered surface pressure of this plateau. These effects suggest that resveratrol tends to favour the condensed phase. However this technique does not allow to estimate where resveratrol could be localized in the lipid monolayer.

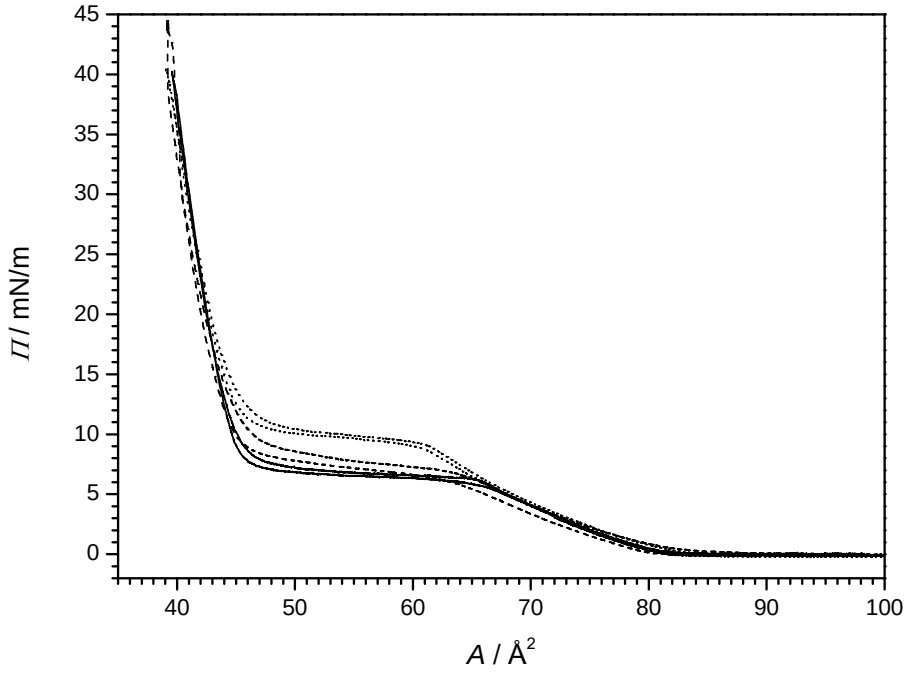

Figure 6.2: Surface pressure - area isotherms of DPPC monolayers, containing 0 mol % (dotted line), 2.5 mol % (dashed line) and 5 mol % (solid line) of resveratrol at room temperature. Films were not compressed to collapse; compression and expansion isotherms are shown.

6.3 Resveratrol incubation in DPPC bilayers

6.3.1 Characterization of d62- and d13-DPPC bilayers by neutron reflectivity

After the deposition of the bilayers by the Langmuir Blodgett and Langmuir Schaefer methods (see chapter 2), the sample cell was heated up to 62

°C in order to render the bilayers in the biologically relevant fluid phase - the gel to fluid phase transition of a DPPC bilayer occuring at 41.5°C [11].

d13- and d62-DPPC bilayers were characterized in H_2O, D_2O and a mixture of light and heavy water such that the scattering length density of the subphase matches that of silicon (denoted as CMSi) in the case of d13-DPPC or a value of 4 10^{-6} Å^{-2} (denoted as CM4) in the case of d62-DPPC (see figure 6.3). The same model which consist of a symmetrical bilayer on the top of a water layer upon the silicon substrate was applied to fit simultaneously the three reflectivity curves.

The scattering length density reference values for all the materials used in this chapter are listed in table 6.1 and the parameters obtained from the fits are listed in table 6.2. The parameters describing the silicon substrate as well as the silicon oxide layers were determined previously by neutron reflectivity on bare substrates before the bilayer deposition; therefore they were fixed during the fitting procedure.

The headgroup thickness is the same as the one of a DPPC bilayer in gel phase [122]. In both bilayers, the water fraction in the headgroup region is between 15 and 30 % higher than in the tail region; this additional water content corresponds to the hydration shell surrounding the hydrophilic headgroup. Since the tails are highly hydrophobic, the content of water within the tail region is related to an incomplete lipid bilayer coverage.

The tail region of d13-DPPC and d62-DPPC are 31 $\pm$ 1 Å and 28 $\pm$ 1 Å thick, respectively. This difference is compensated by a small difference of the headgroup thickness (8 Å for d13-DPPC and 9 Å for d62-DPPC) so that the total bilayer thickness of the bilayer is the same in both samples. It is worth noting that the scattering length density of the tail region of d62-DPPC bilayer is lower than the nominal value. The lowered scattering length density of the tail region as well as the lowered tail thickness can be explained by a partial mixing between the headgroup and the tail regions [122].

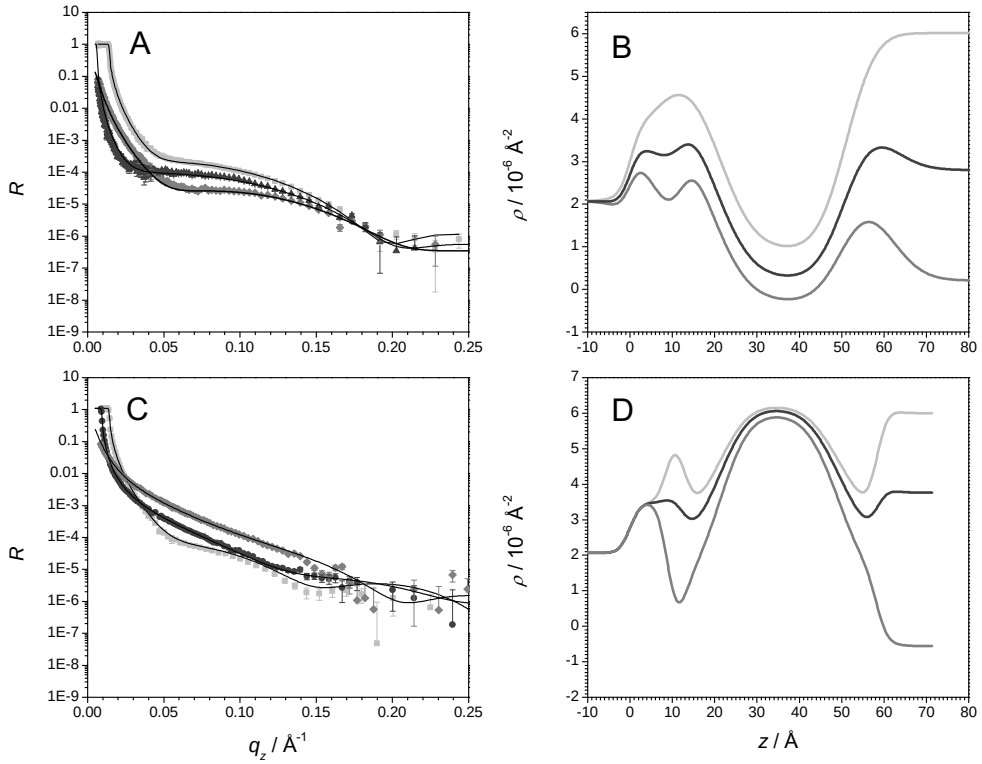

Figure 6.3: Left: neutron reflectivity curves from d13- (A) and d62- (C) DPPC bilayers in D_2O (light grey square), CM4 (dark grey circle), CMSi (dark grey triangle) and H_2O (grey diamond) and their corresponding fits (solid line). Right: scattering length density profiles of d13- (B) and d62- (D) DPPC bilayers in D_2O (light grey), CMSi and CM4 (dark grey) and H_2O (grey). $z = 0$ at the Si-SiO_2 interface.

Table 6.1: Theoretical values of the molecular volume V_m (Å^3) and scattering length density ρ (in 10^{-6}Å^{-2}) of the materials used in this work [215–217].

Material	V_m	ρ
Si	20	2.07
SiO_2	47	3.47
d-heads: $C_{10}D_{13}H_5O_8PN$	326	5.99
h-heads: $C_{10}H_{18}O_8PN$	326	1.84
h-tails: $C_{15}H_{62}$	890	-0.36
d-tails: $C_{15}D_{62}$	890	6.89
H_2O	30	-0.56
D_2O	30	6.35
resveratrol: $C_{14}H_{12}O_3$	268	2.44
d7-cholesterol: $C_{27}H_{39}OD_7$	630	1.37

6.3.2 DMSO control

The solubility of resveratrol is very low in water. Consequently, it was dissolved in an aqueous solvent mixture containing 25 % (v/v) of dimethyl sulfoxide (DMSO). To be sure to distinguish the effect of resveratrol on the bilayer from the effect of the aqueous DMSO solution, a control measurement was done by measuring the reflectivity of a d62-DPPC bilayer having been in contact with a solution containing water and DMSO (75% and -25% in volume, respectively). After having thoroughly flushed with pure water, the measurements were done in D_2O and H_2O.

Figure 6.4 shows that the reflectivity curves reveal a very slight modification after the injection of DMSO. The curves are slightly shifted towards lower values for the samples in contact with DMSO. The analysis indicated an increase of water content in the layer describing the chain region upon the addition of the DMSO-water solution. It has been shown that DMSO can induce pore formation through DPPC bilayer or makes the membrane more fluid [218]. Therefore the effect could correspond to the increase of water content within the chain. No change in the other parameters was observed.

Table 6.2: Parameters obtained from the fits of the neutron reflectivity profiles of the d13- and d62-DPPC bilayers. SiO_2 parameters were fixed after they were measured on the bare substrate. t = thickness (Å); ρ = scattering length density (10^{-6} Å^{-2}); ϕ = solvent fraction (expressed in %); σ = roughness (Å).

	d62-DPPC			
	t	ρ	ϕ	σ
Si	-	2.07	-	2
SiO_2	9	3.47	-	2
Water	3 ± 2	-	100	3 ± 2
Headgroup	9 ± 2	1.84	30 ± 16	4 ± 1
Tail	28 ± 1	6.2 ± 0.23	14 ± 2	6 ± 1
Headgroup	9 ± 2	1.84	30 ± 16	<5
	d13-DPPC			
Si	-	2.07	-	2
SiO_2	9	3.47	-	7
Water	3 ± 2	-	100	3 ± 2
Headgroup	8 ± 1	5.99	50 ± 10	7 ± 1
Tail	31 ± 1	-0.40 ± 0.10	22 ± 10	5 ± 1
Headgroup	8 ± 1	5.99	50 ± 10	7 ± 1

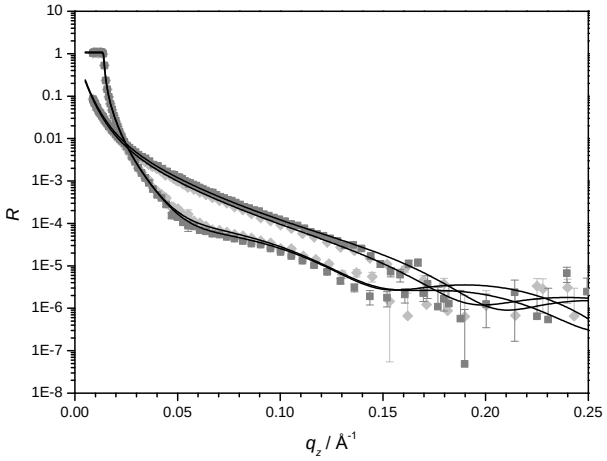

Figure 6.4: Neutron reflectivity curves of a d62-DPPC bilayer before (grey square) and after (light grey) the injection of a H_2O - DMSO (3:1 v/v) mixture in the sample cell. $z = 0$ at the Si-SiO_2 interface.

6.3.3 Resveratrol incorporation from the subphase

After the DMSO control experiment, a resveratrol solution in DMSO-water (2.5 mg mL^{-1}) was injected in the sample cell such that the bilayer could spontaneously take up resveratrol from the subphase. The injection of resveratrol solution was followed by an incubation time of about one hour to let resveratrol molecules interact with the lipid bilayers. Afterwards, the system was thoroughly rinsed and reflectivity curves were measured in three contrasts. The reflectivity was measured for both systems in three different contrasts: H_2O, D_2O and CMSi for d13-DPPC or CM4 for d62-DPPC bilayers. The change in reflectivity curves is shown in figure 6.5. For the case of the d62-DPPC bilayer, the curves in D_2O show that after the resveratrol incubation the reflectivity in the q_z range between 0.04 and 0.10 Å^{-1} increases. In the case of d13-DPPC, the reflectivity decreases at q_z value higher than 0.11 Å^{-1}.

The application of layer models based on symmetric membranes did not yield a consistent model for the two bilayers. As a second approach, no symmetry constraints were imposed on the fitting model used for the inner and the outer headgroup layers, regarding layer thicknesses, scat-

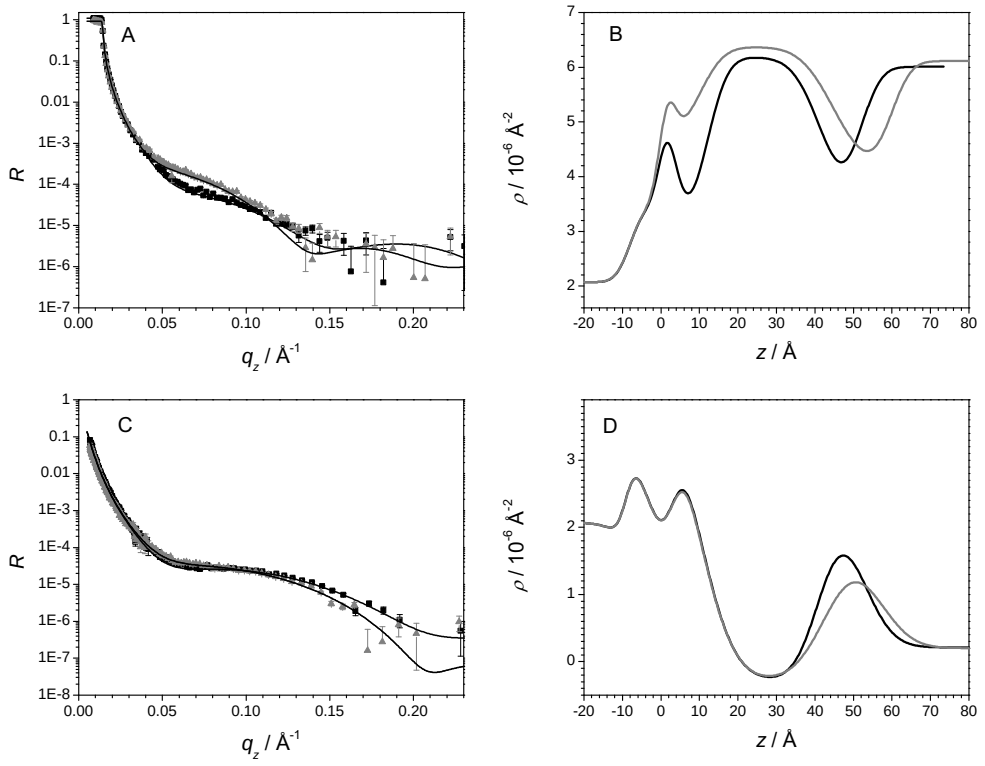

Figure 6.5: Neutron reflectivity curves from a d62-DPPC bilayer in D_2O (A) and d13-DPPC bilayer in H_2O (C) before (black square) and after (grey triangle) the injection of resveratrol in the experimental cell. Right: scattering length density profiles obtained from the fits of the d62-DPPC bilayer in D_2O (B) and d13-DPPC bilayer in H_2O (D) before (dark grey) and after (light grey) resveratrol incubation. $z = 0$ at the Si-SiO_2 interface.

tering length densities or solvent volume fractions. However, letting too many parameters fluctuate did not allow us to find a consistent model for both bilayers. Therefore, the parameters describing the inner headgroup region were fixed. In both types of bilayers (d13- and d62-DPPC), an increase of the thickness of the outer headgroup layer, accompanied by a change of scattering length density (see table 6.3), yielded a better description of the measured reflectivity curves. Moreover, the experiments with the deuterated headgroup lipids, d13-DPPC, exhibited high contrast between headgroup and hydrogenated resveratrol.

Table 6.3: Chains and outer headgroup thickness and scattering length density values before and after the incorporation of resveratrol. t =thickness (Å); ρ=scattering length density (10^{-6} Å^{-2}); ϕ=solvent fraction (expressed in percent); σ=roughness (Å).

	before resveratrol incubation			after resveratrol incubation		
d13-DPPC	t	ρ	σ	t	ρ	σ
chains	31 ± 1	-0.40 $\pm$ 0.10	5 ± 1	33 ± 1	-0.40 $\pm$ 0.04	7 ± 1
outer headgroups	8 ± 2	5.99	7 ± 1	11 ± 2	5.18 $\pm$ 0.83	7 ± 1
d62-DPPC	t	ρ	σ	t	ρ	σ
chains	28 ± 1	6.20 $\pm$ 0.23	6 ± 1	35 ± 1	6.50 $\pm$ 0.06	7 ± 2
outer headgroups	9 ± 2	1.84	4 ± 1	15 ± 2	1.96 $\pm$ 0.56	4 ± 2

The tilt angle, η, of the headgroups with respect to the bilayer normal can be estimated from the geometric properties of the headgroup and tail slabs with the relation

$$\eta = acot\left(\frac{t_h}{a}\right) = acot\left(\frac{t_h}{\sqrt{\frac{2v_t}{t_t(1-\phi_W)}}}\right) \tag{6.1}$$

where we assume that the phospholipid is contained in a cuboid of total volume $V = (t_h + t_t/2) * a^2$ where t_h is the headgroup thickness (Å), t_t is the thickness of the tail box and a is the side of the square basis of the cuboid, which represents also the area occupied by one DPPC molecule (see figure 6.6).

The area occupied by a DPPC molecule is calculated from the molecular volume of two tails v_t (Å^3), the thickness of the tail box t_t (Å) and the volume fraction of the solvent in the tail box, ϕ_W. The tilt angle for d13-DPPC headgroups is 45.5° and becomes 35.7° after the insertion of resveratrol. In the case of d62-DPPC, the initial tilt angle is 43.8°and becomes 31.9° after resveratrol incubation. In both cases, there is a tilt angle decrease of $\sim 10°$ in the presence of resveratrol.

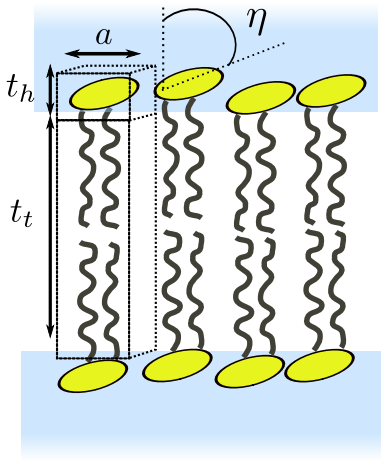

Figure 6.6: Scheme of a DPPC bilayer deposited onto a substrate and the dimensions of the cuboid containing one DPPC molecule.

6.3.4 Resveratrol as initial component of membrane composition

The structural properties of co-deposited DPPC and resveratrol bilayers were also investigated. Three different types of fluid bilayers (T = 62° C) were deposited by the vesicle fusion method [117, 118, 219]. Two bilayers contained d62-DPPC with 2.5 and 5 % of resveratrol (mol/mol), respectively while the third one was composed of only d62-DPPC for comparison. The reflectivity curves of pure and 2.5% resveratrol-containing d62-DPPC are very similar while the reflectivity curve of 5% resveratrol-containing d62-DPPC is different from that from the pure lipids. The reflectivity curves and scattering length density profiles of the d62-DPPC bilayer in absence and presence of 5% resveratrol are shown in figure 6.7 and the parameters obtained from the fits are listed in table 6.4.

Unlike the situation where resveratrol was taken up in the bilayer from the subphase, it was possible in this case to use a model depicting a symmetric bilayer to fit the data. The headgroup of the DPPC bilayer containing 5% resveratrol has the same thickness as in the resveratrol-free DPPC bilayer. The scattering length density of the headgroup is slightly different but the parameter uncertainty is too large to make the differ-

ence significant. In the tail region, the scattering length density of the resveratrol-containing bilayer is lower than a resveratrol-free bilayer. It is worth pointing out at the increased roughness in every interface in the resveratrol-containing bilayer.

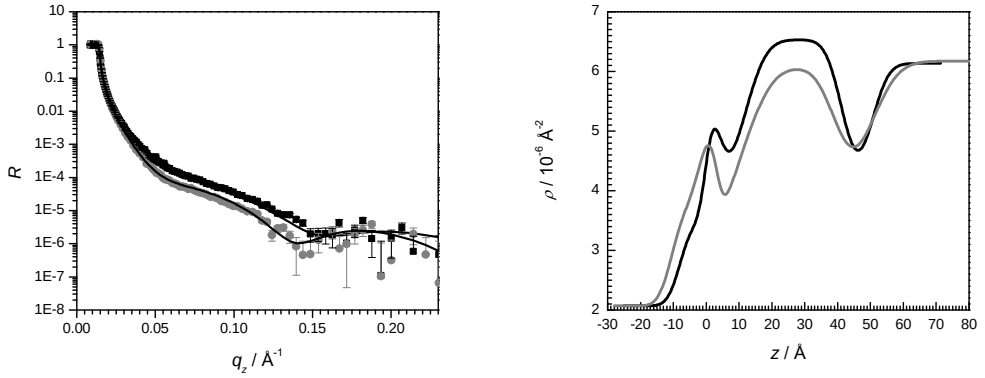

Figure 6.7: Left: neutron reflectivity curves from a d62-DPPC bilayer in absence (black square) and in presence of 5% of resveratrol (grey triangle) in D_2O and their corresponding fits. Right: scattering length density profiles obtained from the fits in absence (dark grey) and in presence of 5% resveratrol(light grey). z = 0 is located at the SiO_2 - water interface.

Table 6.4: Structural parameters obtained by fitting the neutron reflectivity from DPPC bilayers containing 0 and 5 % of resveratrol. t = thickness (Å); ρ = scattering length density (10^{-6} Å^{-2}); σ = roughness (Å).

t	0% resveratrol	5% resveratrol
inner headgroup	9 ± 3	9 ± 3
chain	30 ± 1	28 ± 2
outer headgroup	9 ± 3	9 ± 3
ρ		
inner headgroup	1.84	2.00 ± 0.95
chain	6.65 ± 0.18	6.05 ± 0.19
outer headgroup	1.84	2.00 ± 0.95
σ		
headgroup/chain	5 ± 1	7 ± 1
chain/headgroup	4 ± 1	5 ± 2
headgroup/water	4 ± 3	7 ± 2

6.4 Resveratrol incubation in cholesterol-containing d13-DPPC bilayer

6.4.1 Effect of cholesterol on lipid bilayers

Cholesterol is a major component in the animal membrane. Its chemical structure contain a hydrophilic hydroxyl group and hydrophobic ring (see structure in figure 6.8). It is admitted that cholesterol modifies the phase transition and can act as a "thermal buffer". At a certain concentration in animal membranes, it makes the membrane less fluid at 37 °C. However, it keeps the membrane in a fluid state below the phase transition temperature.

Since resveratrol can also modify the phase transition and the packing of the bilayer, it is interesting to investigate the interaction of resveratrol with cholesterol-containing DPPC bilayer. It is admitted that cholesterol is located upright in a lipid bilayer so that the hydroxyl group can form hydrogen bonds with the phospholipids carboxyl group [220]. However,

there are studies which show that cholesterol can lie in a perpendicular orientation in the interior of the lipid bilayer at higher unsaturation degree [221]. The chosen system for this study consists of a head deuterated d13-DPPC bilayer containing d7-cholesterol 6:1 (DPPC mol/ cholesterol mol).

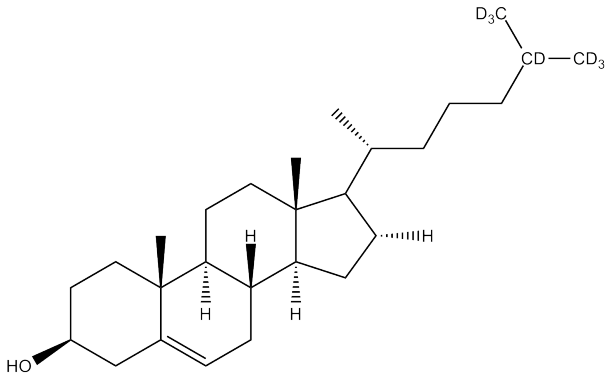

Figure 6.8: Chemical structure of d7-cholesterol used in this work.

6.4.2 Characterization of cholesterol-containing d13-DPPC bilayers

The bilayer was deposited by means of LB-LS techniques. The compression isotherm shows that the cholesterol, at this concentration, contributes to the disappearance of the plateau corresponding to the liquid ordered - liquid-expended phases coexistence (figure 6.9).

The Langmuir Blodgett and Langmuir Schaefer deposition was done after the characterization of the bare substrate. Reflectivity from the bilayer was then measured at 62 °C in three different contrasts: H_2O, CMSi, and D_2O (figure 6.10). The table 6.5 shows the parameters obtained from the fits. One can see that the presence of cholesterol does not have an influence on the headgroup thickness nor the headgroups and tails scattering length densities. The main difference comes from the hydrophobic core thickness which is 2 Å greater than that of the pure d13-DPPC bilayer.

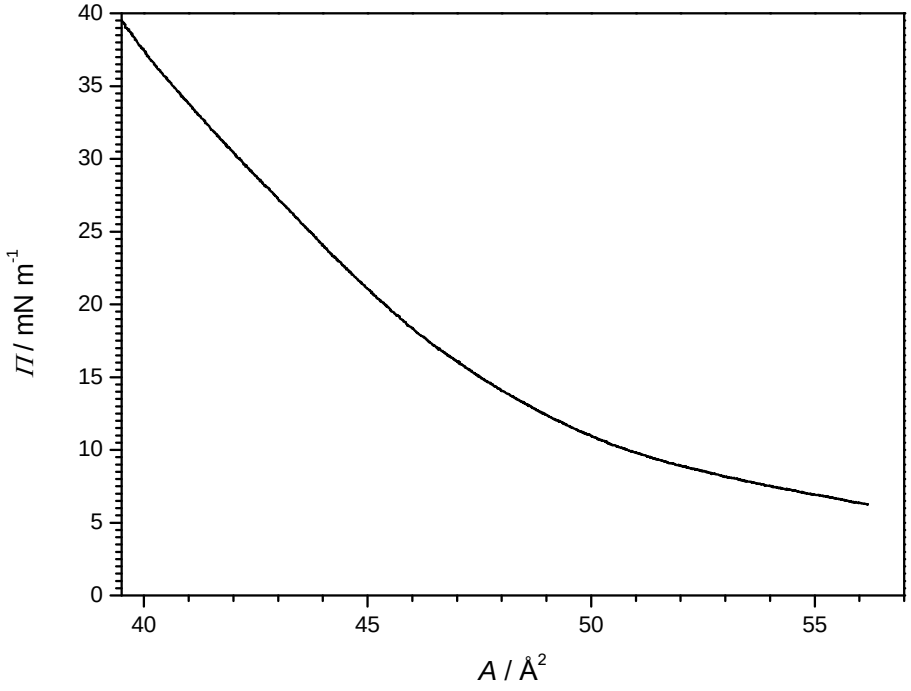

Figure 6.9: Surface pressure - Area isotherm of a cholesterol-containing DPPC monolayer. The molar fraction of cholesterol is 0.14.

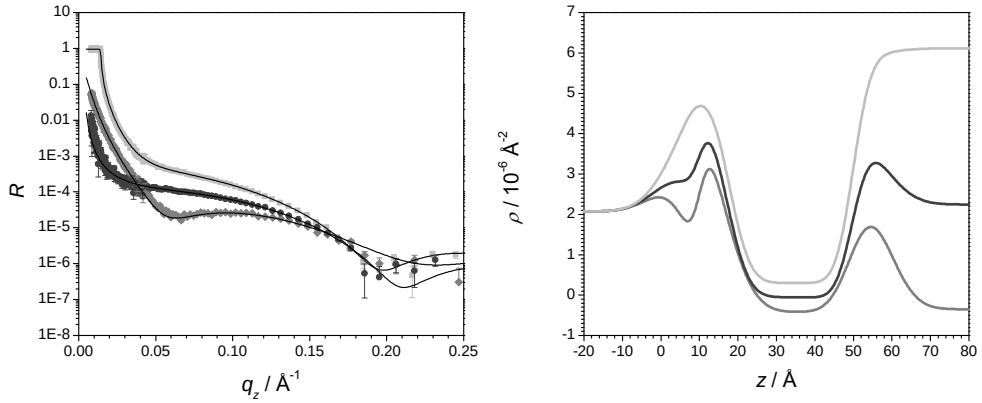

Figure 6.10: Left: neutron reflectivity curves of a d7-cholesterol-containing d13-DPPC bilayer (6:1 mol/mol) in D_2O (light grey square), CMSi (dark grey circle) and H_2O (grey diamond). Right: scattering length density profile obtained from the fits of the d7-cholesterol-containing d13-DPPC bilayer (6:1 mol/mol) in D_2O (light grey), CMSi (dark grey) and H_2O (grey). z = 0 is located at the Si-SiO_2 interface.

Table 6.5: Parameters obtained from the fits of a cholesterol-containing d13-DPPC bilayer before and after the incorporation of resveratrol. t=thickness (Å); ρ=scattering length density (10^{-6} Å^{-2}); σ=roughness (Å).

	before resveratrol incubation			after resveratrol incubation		
	t	ρ	σ	t	ρ	σ
inner headgroups	8 ± 2	6.17 ± 1.70	6 ± 1	8	6.17	6
chains	33 ± 2	-0.43 ± 0.11	5 ± 1	31 ± 1	-0.34 ± 0.06	7 ± 1
outer headgroups	8 ± 2	6.17 ± 1.70	6 ± 1	11 ± 2	5.67 ± 1.74	4 ± 2

6.4.3 Resveratrol incubation in cholesterol-containing d13-DPPC bilayers

After the resveratrol injection and abundant rinsing, reflectivity profiles were measured in D_2O and H_2O. Figure 6.11 shows that, after the incubation of resveratrol, the curves were different after the first local minimum which is located at $q_z = 0.05$ Å^{-1}. The strategy used to fit the cholesterol-free bilayer after the incubation of resveratrol was also adopted here. As in the case of the d13-DPPC bilayer, the headgroup thickness increases to 11 Å. The scattering length density region of the headgroup also changes but the parameter uncertainty is too large since the measurements were done in only two contrasts. In the presence of cholesterol, unlike the pure DPPC bilayers, the effect of resveratrol results slightly thinning of the tail region from 33 Å to 31 Å. The scattering length density of the hydrophobic core is slightly higher after resveratrol interaction. Another interesting feature is the enhanced roughness at the tail - outer headgroup interface.

6.5 Discussion

Resveratrol is known for its antioxidant properties which have been proven by studies made *in vivo* as well as *in vitro* [214]. It is admitted that the location of resveratrol within the membrane is responsible for the antioxidant activity, probably by scavenging free radicals or by modifying their propagation across the bilayer [202]. Therefore, it is crucial to know precisely

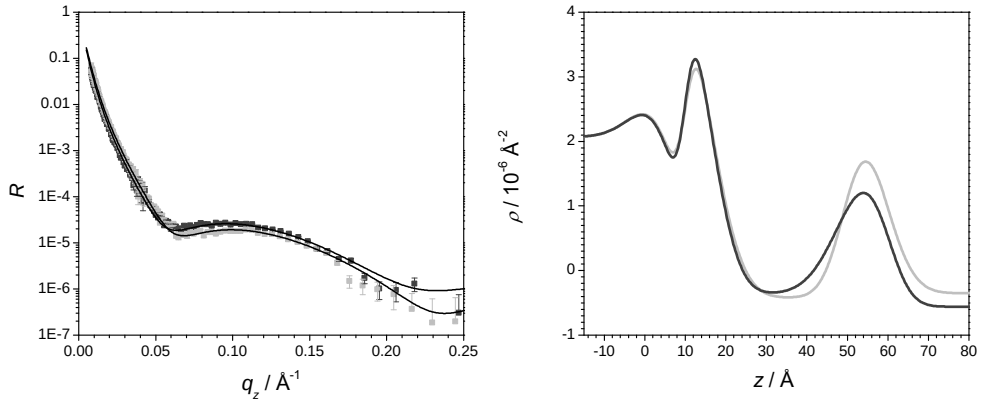

Figure 6.11: Left: Neutron reflectivity curves of a d7-cholesterol-containing d13-DPPC bilayer (6:1 mol/mol) in H_2O before (dark grey square) and after (light grey square) the incubation of resveratrol and their corresponding fits. Right: scattering length density profile obtained from the fits of the d7-cholesterol-containing d13-DPPC bilayer (6:1 mol/mol) in H_2O before (dark grey square) and after (light grey square) the incubation of resveratrol. z = 0 is located at the Si-SiO_2 interface.

where resveratrol sits in the membrane in order to explain such beneficial effect.

There are currently contradictory studies about the location of resveratrol within membrane model lipid bilayer. By using EPR and fluorescence probes located in different regions of the bilayers, Brittes & al. [202] and Fabris & al [214] have measured the activity of these probes in the absence and in presence of resveratrol. They observed that the probes responding to the presence of resveratrol were located at the C6, C9 carbons in the fatty acid regions and at the headgroup region, and concluded that resveratrol is located at the tail-headgroup interface. This was confirmed by similar studies by Wesełoska & al [222]. They investigated resveratrol effects by means of EPR, fluorescence spectroscopy and observed that resveratrol has a stronger influence on EPR probe located at the headgroup region than on the probes located in the tail regions; they concluded that resveratrol is located mainly in the headgroup region even though they do not exclude that some resveratrol could insert more deeply in the tail region .

The insertion of resveratrol in mixture of DOPC and DOPG monolayers at the air-water interface was also investigated by X-ray reflectivity [201]. They demonstrated that there is a slow kinetics of interaction with the monolayer (more than one hour) which resulted to a modification of the chain packing.

In the present study, two methods were combined in order to detect the effects of resveratrol incorporated on into DPPC host layers, both mono- and bilayers. Data analysis led to establishing a joint model for the location and the possible mechanism of action of resveratrol in the host membrane.

A first hint towards the determination of the location of resveratrol in a host layer of DPPC was given from the behaviour of the compression isotherm that shows a condensing impact of resveratrol on a monolayer, as described above (figure 6.2).

Further details on the structural changes caused by the incorporation of resveratrol, this time into host bilayers, were directly determined by neutron reflectometry by using two different procedures.

The first approach consisted in investigating the structural parameters of a bilayer before and after the interaction of resveratrol from the subphase. This approach mimics the biologically relevant mechanism of interaction since resveratrol is brought from an extracellular environment to the cell and, if partitioned from the water into the membrane, may accumulate there to big amounts.

When resveratrol interacted with a planar DPPC bilayer from the subphase, the effect mainly occurred on the outer headgroup region leading to an increase of thickness and change of scattering length density. The modification of the value of the scattering length density within the headgroup region (as shown in table 6.3, $5.99 \leftrightarrow 5.18$) is directly related to the presence of resveratrol. This is, especially evident in the case of the deuterated headgroups since the contrast is very high. At the same time the thickness of the headgroup region, in the slab model, extends in the z-direction by 50% (see Table 6.3). This drastic observation extension is only possible if the headgroup dipoles are turned from a more flat into a more upright orientation, changing their tilt angle with respect to the plane bilayer normal.

Resveratrol, when incorporated into the bilayer, thus forces the headgroup to adopt a different configuration because there is no free volume at the headgroup-tails interface (see figure 6.12). It has to be stressed however that the concentration of resveratrol (2.5 mg/mL or 11 mM) in the subphase is by far above the resveratrol concentration observed in vivo (20 nM-2μ M) [223].

It was possible to calculate the average headgroup tilt angle. The value comes from a slab thickness that includes the glycerol backbone, therefore the apparent length of the dipole, and hence the angle η attributed to the P-N -dipole axis, is overestimated. The insertion of resveratrol yields a decrease of the average headgroup tilt angle by 10°, from $\sim$ 45° to $\sim$ 35°. The value for the projected area/ headgroup is reduced at the same time (see sketch in figure 6.12). As a consequence, the chain packing is enhanced and leads to an extension within the chain region. This is in agreement with the findings from the monolayer compression isotherms and confirms that the presence of resveratrol induces a more condensed phase.

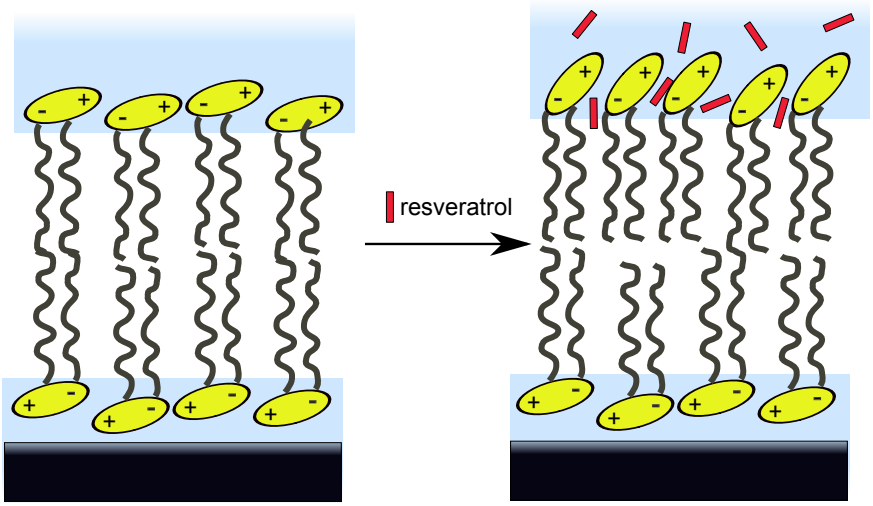

Figure 6.12: Schematic representation of localization of resveratrol insertion in the membrane when adsorbed from the subphase. The headgroup dipole created by the phosphate and choline charges is reoriented because of the volume insertion occupied by of the resveratrol.

In the second approach, resveratrol was co-dissolved with lipids (5/95, mol/mol) before being deposited onto the substrate. The values of the scattering length densities in all three regions, as determined from the data analysis, indicate the presence of resveratrol to almost equal extent in both sides of the bilayer at the interface between headgroups and tail regions. The modification of the headgroup tilt angle is insufficient to significantly change the layer thickness, unlike the case of the first approach. This results mostly in a change of the roughness. The roughness of the interface between the inner headgroup region and silicon was constrained by the silicon surface. Thus, the impact of resveratrol appears as an increased roughness at the interface between the inner headgroups and tail regions. The roughness of the interface between the outer headgroup and tail regions is not significantly increased, reflecting the freedom of hydrocarbon chains to adopt their conformation. The presence of some resveratrol within the outer headgroup layer results in the increased roughness of the headgroup-water interface.

Since the headgroup thickness is not affected by the presence of resveratrol when coddissolved with lipid, one can assume that resveratrol does not impact the conformation of the headgroup. The main difference being the enhanced roughness between the regions of the bilayer: resveratrol is likely located deeper towards the chain region, i.e. at the hydrophobic - hydrophilic interface as shown in figure 6.13. The roughness at the inner headgroup - water interface does not increase whereas that at the inner headgroup - tail interface increases because the modelled inner headgroup includes resveratrol which is located only towards the inside of the bilayer.

The effect of resveratrol on the structure of cholesterol-containing DPPC bilayer when adsorbed from the subphase was also investigated. Interestingly, the outer headgroup region is extended as well but the tail region got thinner. By looking at the scattering length density profiles of the lipid bilayer before and after the resveratrol incubation (figure 6.11), the overall thickness is not higher but even slightly lower when resveratrol is present in the bilayer. The scattering length density profiles show that the main effect induced by the presence of resveratrol arises at the tail - outer headgroup region. This difference compared to the cholesterol-free lipid

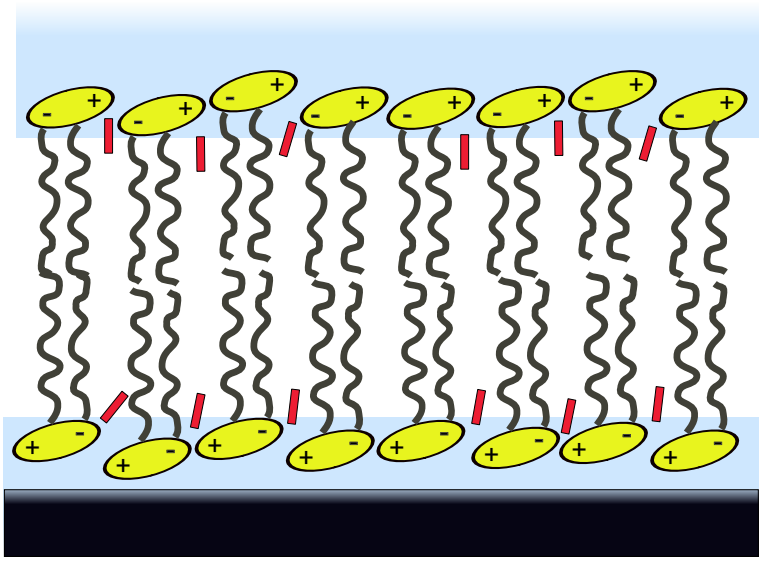

Figure 6.13: Schematic representation of localization of resveratrol in the membrane when co-dissolved with DPPC. Unlike the situation where it is adsobred from the subphase, resveratrol is located at the boundary between the tail and headgroup regions.

bilayer can have two explanations. This first one is an immediate effect of the cholesterol which could have favorable interactions with resveratrol. The second explanation is that cholesterol induces a re arrangement of the DPPC packing which might facilitate the insertion of resveratrol.

6.6 Conclusions

The investigation of the anti-oxidant molecule resveratrol interaction with DPPC mono- and bi-layers was carried out by Langmuir compression isotherms and neutron reflectivity. It is important to know the location of the resveratrol in order to explain its anti-oxidant properties. All results indicate that resveratrol is located at the interface between the headgroup and tail regions with effects depending on the volume fraction. When present in large quantities it induces an ordering of the lipid chains and a lowering of the tilt angle of the headgroups. The location at the hydrophilic-hydrophobic interface within the lipid bilayer can explain its

anti-oxidant properties since the active hydroxyl group of resveratrol is placed at the same level of the fatty acid unsaturated bonds from where the radicals can be formed [214].

Chapter 7

Conclusions and future perspectives

By the optimisation of complex planar bilayer systems exploiting deuterium labelling techniques, the interactions of lipid bilayers with biorelevant molecules can be probed in details using neutron reflectometry.

In the first chapter, we used the yeast *Pichia pastoris* as engine to produce fully deuterated lipids which are not commercially available. *Pichia pastoris* was chosen because it synthesizes the same phospholipids as those found in human cells (mainly PC and PE) and is able to grow in a fully deuterated environment. The analysis showed that this yeast species is able to produce the same type of phospholipids in hydrogenated and deuterated media. However, cells grown in deuterated medium synthesize mainly C18:1 fatty acids whereas the fatty acid composition from yeast cells grown in hydrogenated medium is more complex. The growth culture temperature was lowered in order to verify whether it was possible to modulate the amount of polyunsaturated fatty acid produced by yeast. It turns out that lowering the growth temperature to 18 °C helped to increase the number of unsaturated bonds in deuterated fatty acids but this was not enough to reach the level of hydrogenated lipids. Preliminary analysis of the sphingolipid content was also performed and revealed the presence of unidentified sphingolipids (probably inositolphosphoceramide) and ce-

ramides in much smaller quantities compared to glycerophospholipids. Mass spectrometry analysis (performed by collaborators therefore not described in this thesis) showed that the deuterated environment does not affect the ergosterol synthesis and leads to perdeuterated ergosterol.

A protocol was established in this thesis to separate and recover PC and PE from other phospholipids. As future perspective, purification from the PC or PE fractions to molecular species still needs to be performed. This can be achieved by using reverse phase HPLC, separating PC or PE batches to molecular species as a function of the tail hydrophobicity. By purifying such molecular species, it will be possible in the future to investigate model membranes made of compounds which are more biologically relevant than the ones currently used but not yet accessible.

In the second chapter, we used the *Pichia pastoris* lipid extracts to reconstitute different membranes onto silicon substrates. The reconstituted membranes structures and their interaction with the antifungal amphotericin B (AmB) were characterized by neutron reflectometry. We used polar lipid fractions (containing mainly phospholipids and glycolipids) from the hydrogenated and deuterated batches in presence and absence of ergosterol. It turns out that the lipid composition affects the thickness of the tails region and the roughness values at the headgroup - tail interfaces. The main fatty acid being C18:1 in deuterated extracts, the bilayer presents a tail thickness is the same as that of the hydrophobic core of synthetic DOPC membranes (31 Å). The presence of ergosterol in the deuterated membrane does not increase the tail thickness but increases the roughness at the headgroup - tail interface, meaning that ergosterol is probably located upright parallel to the tails. The thickness of the hydrogenated bilayer is lower because of the higher number of fatty acid unsaturations but the bilayer presents an enhanced roughness at the chains - outer headgroups boundary. The presence of ergosterol results in the increase of the bilayer thickness. This might mean that ergosterol is located deeply within the chain, as it has been observed for cholesterol in model membranes composed of polyunsaturated fatty acid.

After having characterized the structural properties such as thickness,

scattering length density and roughness of the different reconstituted yeast lipid bilayers, we investigated the effect of a small anti-fungal antibiotic molecule, amphotericin B (AmB) on the lipid bilayers structure. This molecule was chosen because it is known that it interacts more with ergosterol containing membranes than with cholesterol containing ones. The lack of a complete understanding of its mechanisms of action impedes nowadays the formulation of less toxic derivatives. For membranes composed of polar lipids only, AmB accumulates on the top of lipid bilayers resulting in a thick and diluted layer in the scattering length density profile. This shows that, despite the difference in fatty acyl composition, AmB does not insert in lipid bilayer because the structural parameters of the bilayer are unchanged.

However, when sterols are present in the membranes, the interaction with AmB leads to changes in structural parameters of the lipid bilayers in addition to the formation of the thick and diluted layer on top of it. In the case of the hydrogenated membrane, the chain region becomes thinner when AmB interacts with the bilayer. This new thickness (25 Å) corresponds roughly to the length one AmB molecule, suggesting that it spans the entire membrane in a conformation upright. In the deuterated membrane, the isotopic contrast between hydrogenated AmB and deuterated lipids allowed measuring a change in scattering length density of the chain region, meaning that AmB inserts in the hydrophobic core. However, the thickness value of the chain region stays constant upon the AmB insertion. Therefore, the fatty acyl composition plays an important role on the conformation of the membrane for the interaction and incubation of AmB in presence of sterol while this behaviour was not observed in absence of sterol.

All yeast membranes in this work were reconstituted from homogenate batches, i.e. from a total lipid extraction. In the future, a very interesting perspective would be to study the influence of AmB on membranes which are extracted from selected organelles. Indeed, AmB might interact differently with the plasma membrane, with the mitochondrial membrane or with the nuclear membrane since the relative amounts of phospholipids and sterols are different. In a more general way, reconstituting

selected membrane extracted from different parts of the cell to study their responses to drugs would be a huge breakthrough in the use of scattering technique for membrane research.

In the third chapter, we studied the structure and localization of synthetic intermediates in chloroplast membranes. Two chloroplast membranes were reconstituted on sapphire and silicon substrates. The membrane reconstituted on silicon was a ternary mixture composed of MGDG, DGDG and PG and the one on sapphire was a quaternary mixture composed of MGDG, DGDG, PG and SQDG. The overall thickness of the bilayer made from the ternary mixture is 38 Å, while the thickness of the one made from the quaternary mixture is 28 Å. The difference could come from the difference in composition and / or a substrate effect.

In membranes composed by ternary and quaternary mixtures, the presence of the intermediate for the synthesis of the lipids , diacylglycerol (DAG), involves an increase in the area per lipid measured by the Langmuir trough. Moreover, neutron reflectivity measurements show that the thickness values of both bilayers decrease. This suggests that DAG is located upright next to the lipid chains and it results in headgroups flattening. Moreover, the water layer thickness located between the lipids and the substrate increases when the substrate is negatively charged and decreases when the substrate is positively charged. This suggests that the change of headgroup conformation makes the charges carried by lipids more accessible.

Finally, asymmetric membranes containing the other intermediate, phosphatidic acid (PA), in one leaflet were prepared, both for ternary and quaternary mixtures, in order to study the PA flip flop at different pH. However, the PA containing lipid bilayers are not stable and what is observed is the progressive bilayer desorption from the substrate. It was observed that bilayers are retained for a longer period on sapphire due to favourable electrostatic interactions. This result is interesting in itself because it shows that PA-containing chloroplast membrane can not be kept flat.

In the last chapter, we have investigated the interaction of a polyphe-

nol, called resveratrol, with model membranes composed of DPPC and mixtures of DPPC and cholesterol. This drug has been found to be responsible of the "French paradox", i.e. the inverse correlation between red wine consumption and coronary hearth disease. Few investigations have been carried out on the precise localization of resveratrol in model membranes.

For DPPC bilayers, we found out that resveratrol, when adsorbed from the subphase, induces a reorganization of the polar headgroups resulting in an increased headgroup thickness. However, when resveratrol is dissolved with DPPC before being deposited on the substrate, it affects mostly the tail - headgroup interface without changing the headgroups conformation.

In presence of cholesterol, resveratrol adsorbed from the subphase also increases the outer headgroup region thickness. Unlike in the case of pure DPPC bilayers, the interaction of resveratrol with cholesterol containing DPPC bilayer leads to a thinning of the hydrophic core. Therefore, the overall bilayer thickness is lowered after resveratrol interaction. The difference compared to the cholesterol-free bilayers is not clear. It could come from specific interactions between cholesterol and resveratrol or by the difference in lipid packing in the model membrane due to the presence of cholesterol.

As a perspective, the interaction of resveratrol with bilayers composed of different lipid species could be used. Indeed, using DPPC was convenient because we can have the tail-deuterated and head-deuterated versions, which increased the quality of the analysis. However, the bilayer enters the fluid phase only at temperature higher than the physiological one ($T_m = 41.5$°C). It is possible to use partially deuterated POPC, with one chain fully deuterated and the other chain fully hydrogenated. The problem is that the contrast is smaller in this system. Another perspective, related to the work carried out in the previous chapters, would be to use natural PC extracted and purified from yeast since they are unsaturated and fully deuterated.

As general conclusion, we have shown that by applying neutron reflectivity and the contrast variation technique, the structural properties of

lipid bilayers and their interactions with drugs can be obtained. Using lipids extracted from living organisms makes such structural studies more biologically relevant since the reconstituted lipid bilayers have the same chemical composition as natural membranes. The work presented here is an additional step towards the elaboration of membrane systems for biophysical studies which mimic the conditions encountered in nature.

Bibliography

[1] Bretscher, M. S. *Scientific American* **1985**, *253*, 100–08.

[2] Akoh, C. C.; Min, D. B. *Food lipids: chemistry, nutrition, and biotechnology*; CRC Press, 2008.

[3] Lipowsky, R.; Sackmann, E. *Structure and Dynamics of Membranes: I. From Cells to Vesicles/II. Generic and Specific Interactions*; 1995; Vol. 1.

[4] Kathiresan, S.; Melander, O.; Guiducci, C.; Surti, A.; Burtt, N. P.; Rieder, M. J.; Cooper, G. M.; Roos, C.; Voight, B. F.; Havulinna, A. S. *Nature genetics* **2008**, *40*, 189–197.

[5] Ridker, P. M.; Rifai, N.; Rose, L.; Buring, J. E.; Cook, N. R. *New England Journal of Medicine* **2002**, *347*, 1557–1565.

[6] Edidin, M. *Annual review of biophysics and biomolecular structure* **2003**, *32*, 257–283.

[7] Brown, D.; London, E. *Annual review of cell and developmental biology* **1998**, *14*, 111–136.

[8] Jacobson, K.; Mouritsen, O. G.; Anderson, R. G. *Nature cell biology* **2007**, *9*, 7–14.

[9] Guidotti, G. *Annual review of biochemistry* **1972**, *41*, 731–752.

[10] Raffaele, M. Self-assembly of lyotropic liquid crystals: from fundamentals to applications. 2011.

[11] Cevc, G. *Phospholipidis handbook*; CRC Press, 1993.

[12] Davies, M.; Schuster, H.; Brauner, J.; Mendelsohn, R. *Biochemistry* **1990**, *29*, 4368–4373.

[13] Badia, A.; Cuccia, L.; Demers, L.; Morin, F.; Lennox, R. B. *Journal of the American Chemical Society* **1997**, *119*, 2682–2692.

[14] Gerelli, Y.; Porcar, L.; Fragneto, G. *Langmuir* **2012**, *28*, 15922–15928.

[15] Vacklin, H. P.; Tiberg, F.; Fragneto, G.; Thomas, R. *Biochemistry* **2005**, *44*, 2811–2821.

[16] Chenal, A.; Prongidi-Fix, L.; Perier, A.; Aisenbrey, C.; Vernier, G.; Lambotte, S.; Fragneto, G.; Bechinger, B.; Gillet, D.; Forge, V.; Ferrand, M. *Journal of molecular biology* **2009**, *391*, 872–883.

[17] Morse, R.; Ma, L. D.; Magin, R. L.; Dunn, F. *Chemistry and physics of lipids* **1999**, *103*, 1–10.

[18] Watson, J. D.; Crick, F. H. *Nature* **1953**, *171*, 737–738.

[19] Dickerson, R.; Kendrew, J. t.; Strandberg, B. *Acta Crystallographica* **1961**, *14*, 1188–1195.

[20] Jacrot, B. *Reports on progress in physics* **1976**, *39*, 911.

[21] Schelten, J.; Schlecht, P.; Schmatz, W.; Mayer, A. *Journal of Biological Chemistry* **1972**, *247*, 5436–5441.

[22] Stuhrmann, H.; Fuess, H. *Acta Crystallographica Section A: Crystal Physics, Diffraction, Theoretical and General Crystallography* **1976**, *32*, 67–74.

[23] Marguerie, G.; Stuhrmann, H. *Journal of molecular biology* **1976**, *102*, 143–156.

[24] Yong, W.; Lomakin, A.; Kirkitadze, M. D.; Teplow, D. B.; Chen, S.-H.; Benedek, G. B. *Proceedings of the National Academy of Sciences* **2002**, *99*, 150–154.

[25] Zaccai, G. *Science* **2000**, *288*, 1604–1607.

[26] Doster, W.; Cusack, S.; Petry, W. *Nature* **1989**, *337*, 754–756.

[27] Diehl, M.; Doster, W.; Petry, W.; Schober, H. *Biophysical journal* **1997**, *73*, 2726–2732.

[28] Smith, J. *Q. Rev. Biophys* **1991**, *24*, 227–291.

[29] Engelman, D. M.; Moore, P. B.; Schoenborn, B. P. *Proceedings of the National Academy of Sciences* **1975**, *72*, 3888–3892.

[30] Koch, M.; Stuhrmann, H. *Methods in enzymology* **1979**, *59*, 670–706.

[31] Timmins, P.; Witz, J. *Virology* **1982**, *119*, 42–50.

[32] Schoenborn, B. P. *Biochimica et Biophysica Acta (BBA)-Reviews on Biomembranes* **1976**, *457*, 41–55.

[33] Kirschner, D.; Caspar, D. *Annals of the New York Academy of Sciences* **1972**, *195*, 309–320.

[34] Kirschner, D. *Spectroscopy in Biology and Chemistry* **1974**, 203–233.

[35] Caspar, D. *Journal of Applied Crystallography* **1974**, *7*, 180–180.

[36] Zaccai, G.; Blasie, J.; Schoenborn, B. *Proceedings of the National Academy of Sciences* **1975**, *72*, 376–380.

[37] Yeager, M. J. Neutron diffraction analysis of the structure of retinal photoreceptor membranes and rhodopsin. 1976.

[38] Chabre, M.; Saibil, H.; Worcester, D. Neutron diffraction studies of oriented retinal rods. 1976.

[39] Stoeckenius, W.; Kunau, W. H. *The Journal of cell biology* **1968**, *38*, 337–357.

[40] Blaurock, A. *Journal of molecular biology* **1975**, *93*, 139–158.

[41] Henderson, R. *Journal of molecular biology* **1975**, *93*, 123–138.

[42] Henderson, R.; Unwin, P. N. T. *Nature* **1975**, *257*, 28–32.

[43] Zaccai, G.; Gilmore, D. J. *Journal of Molecular Biology* **1979**, *132*, 181–191.

[44] Wacklin, H. P. *Current Opinion in Colloid & Interface Science* **2010**, *15*, 445–454.

[45] Tamm, L. K.; McConnell, H. M. *Biophysical Journal* **1985**, *47*, 105–113.

[46] Bayerl, T. M.; Bloom, M. *Biophysical journal* **1990**, *58*, 357–362.

[47] Tiberg, F.; Harwigsson, I.; Malmsten, M. *European Biophysics Journal* **2000**, *29*, 196–203.

[48] Wacklin, H. P.; Tiberg, F.; Fragneto, G.; Thomas, R. K. *Biochimica et Biophysica Acta (BBA)-Biomembranes* **2007**, *1768*, 1036–1049.

[49] Callow, P.; Fragneto, G.; Cubitt, R.; Barlow, D.; Lawrence, M. *Langmuir* **2008**, *25*, 4181–4189.

[50] Daillant, J.; Gibaud, A. *X-ray and neutron reflectivity: principles and applications*; Springer, 2009; Vol. 770.

[51] Squires, G. L. *Introduction to the theory of thermal neutron scattering*; Cambridge University Press, 1978.

[52] Higgins, J. S.; Benoît, H. *Polymers and neutron scattering*; Clarendon Press Oxford, 1994.

[53] Fragneto-Cusani, G. *Journal of Physics: Condensed Matter* **2001**, *13*, 4973.

[54] Nelson, A. *Journal of Applied Crystallography* **2006**, *39*, 273–276.

[55] Vig, J. R. *Journal of Vacuum Science & Technology A: Vacuum, Surfaces, and Films* **1985**, *3*, 1027–1034.

[56] Langmuir, I. *Journal of the American Chemical Society* **1917**, *39*, 1848–1906.

[57] Fitter, T. K. J., Jèorg; Gutberlet *Neutron Scattering in Biology: Techniques and Applications*; Biological and Medical Physics, Biomedical Engineering; Springer, 2006.

[58] Krueger, S. *Current Opinion in Colloid & Interface Science* **2001**, *6*, 111–117.

[59] Daillant, J.; Bellet-Amalric, E.; Braslau, A.; Charitat, T.; Fragneto, G.; Graner, F.; Mora, S.; Rieutord, F.; Stidder, B. *Proceedings of the National Academy of Sciences of the United States of America* **2005**, *102*, 11639–11644.

[60] Gordeliy, V. I.; Chernov, N. I. *Acta Crystallographica Section D* **1997**, *53*, 377–384.

[61] Nagle, J. F.; Tristram-Nagle, S. *Biochimica et Biophysica Acta (BBA) - Reviews on Biomembranes* **2000**, *1469*, 159–195.

[62] Gawrisch, K.; Gaede, H.; Mihailescu, M.; White, S. *European Biophysics Journal* **2007**, *36*, 281–291.

[63] Macauley-Patrick, S.; Fazenda, M. L.; McNeil, B.; Harvey, L. M. *Yeast* **2005**, *22*, 249–270.

[64] Damasceno, L.; Huang, C.-J.; Batt, C. *Applied Microbiology and Biotechnology* **2012**, *93*, 31–39.

[65] Smyth, T. J.; Perfumo, A.; Marchant, R.; Banat, I. M.; Chen, M.; Thomas, R. K.; Penfold, J.; Stevenson, P. S.; Parry, N. J. *Appl Microbiol Biotechnol* **2010**, *87*, 1347–54.

[66] Massou, S.; Augé, S.; Tropis, M.; Lindley, N. D.; Milon, A. *J. Chim. Phys.* **1998**, *95*, 406–411.

[67] Morgan, W. D.; Kragt, A.; Feeney, J. *J Biomol NMR* **2000**, *17*, 337–47.

[68] Massou, S.; Puech, V.; Talmont, F.; Demange, P.; Lindley, N. D.; Tropis, M.; Milon, A. *J Biomol NMR* **1999**, *14*, 231–9.

[69] Sakaki, T.; Zäringer, U.; Warnecke, D. C.; Fahl, A.; Knogge, W.; Heinz, E. *Yeast* **2001**, *18*, 679–695.

[70] Wriessnegger, T.; Gübitz, G.; Leitner, E.; Ingolic, E.; Cregg, J.; de la Cruz, B. J.; Daum, G. *Biochimica et Biophysica Acta (BBA)-Molecular and Cell Biology of Lipids* **2007**, *1771*, 455–461.

[71] Wriessnegger, T.; Leitner, E.; Belegratis, M.; Ingolic, E.; Daum, G. *Biochimica et Biophysica Acta (BBA)-Molecular and Cell Biology of Lipids* **2009**, *1791*, 166–172.

[72] Martin, C. E.; Oh, C.-S.; Kandasamy, P.; Chellapa, R.; Vemula, M. *Biochemical Society Transactions* **2002**, *30*, 1080–1082.

[73] Martin, C. E.; Oh, C.-S.; Jiang, Y. *Biochimica et Biophysica Acta (BBA) - Molecular and Cell Biology of Lipids* **2007**, *1771*, 271–285.

[74] Henry, S. A.; Kohlwein, S. D.; Carman, G. M. *Genetics* **2012**, *190*, 317–349.

[75] Folch, J.; Lees, M.; Stanley, G. H. S. *Journal of Biological Chemistry* **1957**, *226*, 497–509.

[76] Hamilton, J. G.; Comai, K. *Journal of Lipid Research* **1984**, *25*, 1142–8.

[77] Martin, C. E.; Siegel, D.; Aaronson, L. R. *Biochimica et Biophysica Acta (BBA) - Lipids and Lipid Metabolism* **1981**, *665*, 399–407.

[78] Ternes, P.; Wobbe, T.; Schwarz, M.; Albrecht, S.; Feussner, K.; Riezman, I.; Cregg, J. M.; Heinz, E.; Riezman, H.; Feussner, I.; Warnecke, D. *Journal of Biological Chemistry* **2011**, *286*, 11401–11414.

[79] Dickson, R. C.; Lester, R. L. *Biochimica et Biophysica Acta (BBA) - General Subjects* **1999**, *1426*, 347 – 357.

[80] Bossie, M. A.; Martin, C. E. *Journal of Bacteriology* **1989**, *171*, 6409–6413.

[81] Pugh, E. L.; Kates, M. *Biochimica et Biophysica Acta (BBA) - Lipids and Lipid Metabolism* **1975**, *380*, 442–453.

[82] De Smet, C. H.; Vittone, E.; Scherer, M.; Houweling, M.; Liebisch, G.; Brouwers, J. F.; de Kroon, A. I. P. M. *Molecular Biology of the Cell* **2012**, *23*, 1146–1156.

[83] Buist, P. H.; Behrouzian, B. *Journal of the American Chemical Society* **1996**, *118*, 6295–6296.

[84] Buist, P. H. *Natural Product Reports* **2004**, *21*, 249–262.

[85] Kennedy, E. P. *Journal of the American Chemical Society* **1953**, *75*, 249–250, doi: 10.1021/ja01097a522.

[86] Boumann, H. A.; Damen, M. J. A.; Versluis, C.; Heck, A. J. R.; de Kruijff, B.; de Kroon, A. I. P. M. *Biochemistry* **2003**, *42*, 3054–3059.

[87] Patton-Vogt, J. L.; Griac, P.; Sreenivas, A.; Bruno, V.; Dowd, S.; Swede, M. J.; Henry, S. A. *Journal of Biological Chemistry* **1997**, *272*, 20873–20883.

[88] Kajikawa, M.; Yamato, K. T.; Kohzu, Y.; Nojiri, M.; Sakuradani, E.; Shimizu, S.; Sakai, Y.; Fukuzawa, H.; Ohyama,; Kanji, *Plant Molecular Biology* **2004**, *54*, 335–352.

[89] Kajikawa, M.; Yamato, K. T.; Kohzu, Y.; Shoji, S.-i.; Matsui, K.; Tanaka, Y.; Sakai, Y.; Fukuzawa, H. *Plant and Cell Physiology* **2006**, *47*, 64–73.

[90] Hamilton-Miller, J. *Bacteriological reviews* **1973**, *37*, 166.

[91] Donovick, R.; Gold, W.; Pagano, J.; Stout, H. *Antibiotics annual* **1955**, *3*, 579.

[92] Ganis, P.; Avitabile, G.; Mechlinski, W.; Schaffner, C. P. *Journal of the American Chemical Society* **1971**, *93*, 4560–4564.

[93] Hartsel, S.; Bolard, J. *Trends in Pharmacological Sciences* **1996**, *17*, 445 – 449.

[94] Gallis, H. A.; Drew, R. H.; Pickard, W. W. *Review of Infectious Diseases* **1990**, *12*, 308–329.

[95] Walsh, T.; Viviani, M.-A.; Arathoon, E.; Chiou, C.; Ghannoum, M.; Groll, A.; Odds, F. *Medical Mycology* **2000**, *38*, 335–347.

[96] Finkelstein, A.; Holz, R. *Membranes* **1973**, *2*, 377.

[97] De Kruijff, B.; Demel, R. *Biochimica et Biophysica Acta (BBA)-Biomembranes* **1974**, *339*, 57–70.

[98] Van Hoogevest, P.; De Kruijff, B. *Biochimica et Biophysica Acta (BBA)-Biomembranes* **1978**, *511*, 397–407.

[99] Finkelstein, A. *Water movement through lipid bilayers, pores, and plasma membranes: theory and reality*; Wiley New York, 1987; Vol. 4.

[100] Bolard, J.; Legrand, P.; Heitz, F.; Cybulska, B. *Biochemistry* **1991**, *30*, 5707–5715.

[101] Chen, W. C.; Chou, D.-L.; Feingold, D. S. *Antimicrobial Agents and Chemotherapy* **1978**, *13*, 914–917.

[102] Brajtburg, J.; Elberg, S.; Medoff, J.; Kobayashi, G. S.; Schlessinger, D.; Medoff, G. *Antimicrobial Agents and Chemotherapy* **1984**, *26*, 892–897.

[103] Sokol-Anderson, M.; Sligh, J. E.; Elberg, S.; Brajtburg, J.; Kobayashi, G. S.; Medoff, G. *Antimicrobial Agents and Chemotherapy* **1988**, *32*, 702–705.

[104] Beggs, W. H. *Antimicrobial Agents and Chemotherapy* **1994**, *38*, 363–364.

[105] Cohen, B. *International Journal of Pharmaceutics* **1998**, *162*, 95 – 106.

[106] Cohen, B. *The Journal of Membrane Biology* **2010**, *238*, 1–20.

[107] V Cotero, B.; Rebolledo-Antúnez, S.; Ortega-Blake, I. *Biochimica et Biophysica Acta (BBA) - Biomembranes* **1998**, *1375*, 43 – 51.

[108] Wolf, B. D.; Hartsel, S. C. *Biochimica et Biophysica Acta (BBA) - Biomembranes* **1995**, *1238*, 156 – 162.

[109] Fournier, I.; Barwicz, J.; Tancrède, P. *Biochimica et Biophysica Acta (BBA) - Biomembranes* **1998**, *1373*, 76 – 86.

[110] Ruckwardt, T.; Scott, A.; Scott, J.; Mikulecky, P.; Hartsel, S. C. *Biochimica et Biophysica Acta (BBA) - Biomembranes* **1998**, *1372*, 283 – 288.

[111] Huang, W.; Zhang, Z.; Han, X.; Tang, J.; Wang, J.; Dong, S.; Wang, E. *Biophysical Journal* **2002**, *83*, 3245 – 3255.

[112] Barwicz, J.; Tancrède, P. *Chemistry and physics of lipids* **1997**, *85*, 145–155.

[113] Hereć, M.; Islamov, A.; Kuklin, A.; Gagoś, M.; Gruszecki, W. I. *Chemistry and Physics of Lipids* **2007**, *147*, 78 – 86.

[114] Gabrielska, J.; Gagoś, M.; Gubernator, J.; Gruszecki, W. I. *FEBS letters* **2006**, *580*, 2677–2685.

[115] Milhaud, J.; Ponsinet, V.; Takashi, M.; Michels, B. *Biochimica et Biophysica Acta (BBA) - Biomembranes* **2002**, *1558*, 95 – 108.

[116] Foglia, F.; Drake, A.; Terry, A.; Rogers, S.; Lawrence, M.; Barlow, D. *Biochimica et Biophysica Acta (BBA)-Biomembranes* **2011**, *1808*, 1574–1580.

[117] Keller, C.; Glasmästar, K.; Zhdanov, V.; Kasemo, B. *Physical Review Letters* **2000**, *84*, 5443–5446.

[118] Wacklin, H. P. *Langmuir* **2011**, *27*, 7698–7707.

[119] Reviakine, I.; Brisson, A. *Langmuir* **2000**, *16*, 1806–1815.

[120] Reimhult, E.; Höök, F.; Kasemo, B. *Langmuir* **2003**, *19*, 1681–1691.

[121] Richter, R.; Mukhopadhyay, A.; Brisson, A. *Biophysical journal* **2003**, *85*, 3035–3047.

[122] Fragneto, G.; Graner, F.; Charitat, T.; Dubos, P.; Bellet-Amalric, E. *Langmuir* **2000**, *16*, 4581–4588.

[123] Kuhl, T. L.; Majewski, J.; Wong, J. Y.; Steinberg, S.; Leckband, D. E.; Israelachvili, J. N.; Smith, G. S. *Biophysical journal* **1998**, *75*, 2352–2362.

[124] Sugiura, Y. *Biochimica et Biophysica Acta (BBA)-Biomembranes* **1981**, *641*, 148–159.

[125] Klacsová, M.; Westh, P.; Balgavỳ, P. *Chemistry and physics of lipids* **2010**, *163*, 498–505.

[126] Cournia, Z.; Ullmann, G. M.; Smith, J. C. *The Journal of Physical Chemistry B* **2007**, *111*, 1786–1801.

[127] Hull, S.; Woolfson, M. *Acta Crystallographica Section B: Structural Crystallography and Crystal Chemistry* **1976**, *32*, 2370–2373.

[128] Gagos, M.; Gabrielska, J.; Dalla Serra, M.; Gruszecki, W. I. *Molecular membrane biology* **2005**, *22*, 433–442.

[129] Millié, P.; Langlet, J.; Berges, J.; Caillet, J.; Demaret, J.-P. *The Journal of Physical Chemistry B* **1999**, *103*, 10883–10891.

[130] Foglia, F.; Lawrence, M. J.; Demė, B.; Fragneto, G.; Barlow, D. *Scientific reports* **2012**, *2*.

[131] Carde, J.; Joyard, J.; Douce, R. *Biol Cell* **1982**, *44*, 315–324.

[132] Jouhet, J.; Maréchal, E.; Block, M. A. *Progress in lipid research* **2007**, *46*, 37–55.

[133] Gounaris, K.; Sen, A.; Brain, A. P.; Quinn, P. J.; Patrick Williams, W. *Biochimica et Biophysica Acta (BBA)-Biomembranes* **1983**, *728*, 129–139.

[134] Loll, B.; Kern, J.; Saenger, W.; Zouni, A.; Biesiadka, J. *Nature* **2005**, *438*, 1040–1044.

[135] Xu, C.; Fan, J.; Froehlich, J. E.; Awai, K.; Benning, C. *The Plant Cell Online* **2005**, *17*, 3094–3110.

[136] Kobayashi, K.; Awai, K.; Nakamura, M.; Nagatani, A.; Masuda, T.; Ohta, H. *The Plant Journal* **2009**, *57*, 322–331.

[137] Kucerka, N.; Marquardt, D.; Harroun, T. A.; Nieh, M.-P.; Wassall, S. R.; de Jong, D. H.; Schäfer, L. V.; Marrink, S. J.; Katsaras, J. *Biochemistry* **2010**, *49*, 7485–7493.

[138] Bottier, C.; Géan, J.; Artzner, F.; Desbat, B.; Pezolet, M.; Renault, A.; Marion, D.; Vié, V. *Biochimica et Biophysica Acta (BBA) - Biomembranes* **2007**, *1768*, 1526–1540.

[139] Filek, M.; Gzyl, B.; Laggner, P.; Kriechbaum, M. *Journal of plant physiology* **2005**, *162*, 245–252.

[140] Rivas, E.; Luzzati, V. *Journal of Molecular Biology* **1969**, *41*, 261–275.

[141] Epand, R.; Leon, B.; Menger, F.; Kuo, J. *Bioscience reports* **1991**, *11*, 59–64.

[142] Gómez-Fernández, J. C.; Corbalán-García, S. *Chemistry and physics of lipids* **2007**, *148*, 1–25.

[143] Das, S.; Rand, R. *Biochemistry* **1986**, *25*, 2882–2889.

[144] Goldberg, E. M.; Lester, D. S.; Borchardt, D. B.; Zidovetzki, R. *Biophysical journal* **1994**, *66*, 382–393.

[145] Graham Shipley, G.; Green, J. P.; Nichols, B. W. *Biochimica et Biophysica Acta (BBA)-Biomembranes* **1973**, *311*, 531–544.

[146] Brentel, I.; Selstam, E.; Lindblom, G. *Biochimica et Biophysica Acta (BBA)-Biomembranes* **1985**, *812*, 816–826.

[147] van den Brink-van der Laan, E.; Killian, J. A.; de Kruijff, B. *Biochimica et Biophysica Acta (BBA) - Biomembranes* **2004**, *1666*, 275–288.

[148] Goñi, F. M.; Alonso, A. *Progress in lipid research* **1999**, *38*, 1–48.

[149] Szule, J. A.; Fuller, N. L.; Peter Rand, R. *Biophysical journal* **2002**, *83*, 977–984.

[150] De Boeck, H.; Zidovetzki, R. *Biochemistry* **1989**, *28*, 7439–7446.

[151] Hamilton, J. A.; Bhamidipati, S.; Kodali, D.; Small, D. *Journal of Biological Chemistry* **1991**, *266*, 1177–1186.

[152] Ganong, B. R.; Bell, R. M. *Biochemistry* **1984**, *23*, 4977–4983.

[153] Allan, D.; Thomas, P.; Michell, R. H. **1978**,

[154] Leger, A. S.; Cochrane, A.; Moore, F. *The Lancet* **1979**, *313*, 1017–1020.

[155] Renaud, S. d.; de Lorgeril, M. *The Lancet* **1992**, *339*, 1523–1526.

[156] Pourcel, L.; Routaboul, J. M.; Cheynier, V.; Lepiniec, L.; Debeaujon, I. *Trends in Plant Science* **2007**, *12*, 29–36.

[157] Taguri, T.; Tanaka, T.; Kouno, I. *Biological & Pharmaceutical Bulletin* **2006**, *29*, 2226–2235.

[158] Ho, C. Y.; Lin, Y. T.; Labbe, R. G.; Shetty, K. *Journal of Food Biochemistry* **2006**, *30*, 21–34.

[159] Harrison, H. F.; Peterson, J. K.; Snook, M. E. *Allelopathy Journal* **2006**, *17*, 81–87.

[160] Chatterjee, A.; Bagchi, D.; Yasmin, T.; Stohs, S. J. *Molecular and Cellular Biochemistry* **2005**, *270*, 125–130.

[161] Filip, V.; Plockova, M.; Smidrkal, J.; Spickova, Z.; Melzoch, K.; Schmidt, S. *Food Chemistry* **2003**, *83*, 585–593.

[162] Slanina, J.; Taborska, E. *Chemicke Listy* **2004**, *98*, 239–245.

[163] King, R. E.; Bomser, J. A.; Min, D. B. *Comprehensive Reviews in Food Science and Food Safety* **2006**, *5*, 65–70.

[164] Kolouchova, I.; Melzoch, K.; Smidrkal, J.; Filip, V. *Chemicke Listy* **2005**, *99*, 492–495.

[165] Wenzel, E.; Somoza, V. *Molecular Nutrition & Food Research* **2005**, *49*, 472–481.

[166] Naugler, C.; McCallum, J. L.; Klassen, G.; Strommer, J. *American Journal of Enology and Viticulture* **2007**, *58*, 117–119.

[167] Simopoulos, A. P. *European Journal of Cancer Prevention* **2004**, *13*, 219–230.

[168] Jaenicke, L. *Chemie in Unserer Zeit* **2007**, *41*, 9–9.

[169] Cassidy, A.; Hanley, B.; Lamuela-Raventos, R. M. *Journal of the Science of Food and Agriculture* **2000**, *80*, 1044–1062.

[170] Holme, A. L.; Pervaiz, S. *Journal of Bioenergetics and Biomembranes* **2007**, *39*, 59–63.

[171] Ungvari, Z.; Orosz, Z.; Rivera, A.; Labinskyy, N.; Xiangmin, Z.; Csiszar, A. *Faseb Journal* **2007**, *21*, A444–A444.

[172] Jin, H.; Jeong, J.; Kim, H.; Jin, J.; Jun, Y.; Par, M.; Kim, S.; Choi, J.; Lee, W. *Journal of Bone and Mineral Research* **2006**, *21*, S153–S153.

[173] Dudley, J. I.; Das, D. K. *Faseb Journal* **2007**, *21*, A62–A62.

[174] Maranon, J. A.; Lasa, A.; Sancho, S. B.; Txurruka, I.; Caballero, E.; Baquedano, M. P. P.; Galan-Estella, F. *Pharmaceutical Biology* **2012**, *50*, 598–598.

[175] Wu, J. M.; Hsieh, T. C. In *Resveratrol and Health*; Vang, O., Das, D. K., Eds.; Annals of the New York Academy of Sciences; Wiley-Blackwell: Malden, 2011; Vol. 1215; pp 16–21.

[176] Hung, C. F.; Chen, J. K.; Liao, M. H.; Lo, H. M.; Fang, J. Y. *Journal of Nanoscience and Nanotechnology* **2006**, *6*, 2950–2958.

[177] N'Soukpoe-Kossi, C. N.; St-Louis, C.; Beauregard, M.; Subirade, M.; Carpentier, R.; Hotchandani, S.; Tajmir-Riahi, H. A. *Journal of Biomolecular Structure & Dynamics* **2006**, *24*, 277–283.

[178] Kupisiewicz, K.; Boissy, P.; Soe, K.; Abdallah, B.; KasseM, M.; Plesner, T.; Delaisse, J. *Calcified Tissue International* **2007**, *80*, S65–S65.

[179] Elmali, N.; Baysal, O.; Harma, A.; Esenkaya, I.; Mizrak, B. *Inflammation* **2007**, *30*, 1–6.

[180] Esposito, K.; Giugliano, D. *European Heart Journal* **2006**, *27*, 15–20.

[181] Giugliano, D.; Ceriello, A.; Esposito, K. *Journal of the American College of Cardiology* **2006**, *48*, 677–685.

[182] Murias, M.; Handler, N.; Erker, T.; Zielinska-Przyjemska, M. *Drug Metabolism Reviews* **2006**, *38*, 130–130.

[183] Rayalam, S.; Yang, J. Y.; Della-Fera, M. A.; Park, H. J.; Ambati, S.; Baile, C. A. *Faseb Journal* **2007**, *21*, A365–A365.

[184] Fischer-Posovszky, P.; Kukulus, V.; Killian, A.; Debatin, K. M.; Wabitsch, M. *International Journal of Obesity* **2007**, *31*, S53–S53.

[185] Cardile, V.; Chillemi, R.; Lombardo, L.; Sciuto, S.; Spatafora, C.; Tringali, C. *Zeitschrift Fur Naturforschung C-a Journal of Biosciences* **2007**, *62*, 189–195.

[186] Golkar, L.; Ding, X. Z.; Ujiki, M. B.; Salabat, M. R.; Kelly, D. L.; Scholtens, D.; Fought, A. J.; Bentrem, D. J.; Talamonti, M. S.; Bell, R. H.; Adrian, T. E. *Journal of Surgical Research* **2007**, *138*, 163–169.

[187] Bhardwaj, A.; Sethi, G.; Vadhan-Raj, S.; Bueso-Ramos, C.; Takada, Y.; Gaur, U.; Nair, A. S.; Shishodia, S.; Aggarwal, B. B. *Blood* **2007**, *109*, 2293–2302.

[188] Dashwood, R. H. *Journal of Nutrition* **2007**, *137*, 267S–269S.

[189] Latruffe, N.; Delmas, D.; Colin, D.; Lancon, A.; Jannin, B.; Dutartre, P. *Agro Food Industry Hi-Tech* **2006**, *17*, 18–21.

[190] Barstad, B.; Sorensen, T. I. A.; Tjonneland, A.; Johansen, D.; Becker, U.; Andersen, I. B.; Gronbaek, M. *European Journal of Cancer Prevention* **2005**, *14*, 239–243.

[191] Dasgupta, B.; Milbrandt, J. *Proceedings of the National Academy of Sciences of the United States of America* **2007**, *104*, 7217–7222.

[192] Chen, Y.; Tseng, S. H. *In Vivo* **2007**, *21*, 365–370.

[193] Kumar, A.; Kaundal, R. K.; Iyer, S.; Sharma, S. S. *Life Sciences* **2007**, *80*, 1236–1244.

[194] Riviere, C.; Richard, T.; Quentin, L.; Krisa, S.; Merillon, J. M.; Monti, J. P. *Bioorganic & Medicinal Chemistry* **2007**, *15*, 1160–1167.

[195] Ono, K.; Yoshiike, Y.; Takashima, A.; Hasegawa, K.; Naiki, H.; Yamada, M. *Journal of Neurochemistry* **2003**, *87*, 172–181.

[196] Lopez-Miranda, V.; Soto-Montenegro, M. L.; Vera, G.; Herradon, E.; Desco, M.; Abalo, R. *Revista De Neurologia* **2012**, *54*, 349–356.

[197] Tsuchiya, H.; Nagayama, M.; Tanaka, T.; Furusawa, M.; Kashimata, M.; Takeuchi, H. *Biofactors* **2002**, *16*, 45–56.

[198] Jannin, B.; Menzel, M.; Berlot, J. P.; Delmas, D.; Lancon, A.; Latruffe, N. *Biochemical Pharmacology* **2004**, *68*, 1113–1118.

[199] Usha, S.; Johnson, I. M.; Malathi, R. *Molecular and Cellular Biochemistry* **2006**, *284*, 57–64.

[200] Sarpietro, M. G.; Spatafora, C.; Tringali, C.; Micieli, D.; Castelli, F. *Journal of Agricultural and Food Chemistry* **2007**, *55*, 3720–3728.

[201] Evers, F.; Jeworrek, C.; Tiemeyer, S.; Weise, K.; Sellin, D.; Paulus, M.; Struth, B.; Tolan, M.; Winter, R. *Journal of the American Chemical Society* **2009**, *131*, 9516–9521.

[202] Brittes, J.; Lucio, M.; Nunes, C.; Lima, J.; Reis, S. *Chemistry and Physics of Lipids* **2010**, *163*, 747–754.

[203] Olas, B.; Holmsen, H. *Food and Chemical Toxicology* **2012**, *50*, 4028–4034.

[204] Koukoulitsa, C.; Durdagi, S.; Siapi, E.; Villalonga-Barber, C.; Alexi, X.; Steele, B. R.; Micha-Screttas, M.; Alexis, M. N.; Tsantili-Kakoulidou, A.; Mavromoustakos, T. *European Biophysics Journal with Biophysics Letters* **2011**, *40*, 865–875.

[205] Diaz, T. G.; Meras, I. D.; Rodriguez, D. A. *Analytical and Bioanalytical Chemistry* **2007**, *387*, 1999–2007.

[206] Cardot, J. L.; Lammela, W. *Abstracts of Papers of the American Chemical Society* **2006**, *231*.

[207] Prokop, J.; Abrman, P.; Seligson, A. L.; Sovak, M. *Journal of Medicinal Food* **2006**, *9*, 11–14.

[208] Abou-Zeid, L. A.; El-Mowafy, A. M. *Chirality* **2004**, *16*, 190–195.

[209] Hambrock, A.; Franz, C. B. D.; Hiller, S.; Grenz, A.; Ackermann, S.; Schulze, D. U.; Drews, G.; Osswald, H. *Journal of Biological Chemistry* **2007**, *282*, 3347–3356.

[210] Han, Y. S.; Bastianetto, S.; Dumont, Y.; Quirion, R. *Journal of Pharmacology and Experimental Therapeutics* **2006**, *318*, 238–245.

[211] Schneider, Y.; Chabert, P.; Stutzmann, J.; Coelho, D.; Fougerousse, A.; Gosse, F.; Launay, J. F.; Brouillard, R.; Raul, F. *International Journal of Cancer* **2003**, *107*, 189–196.

[212] Camont, L.; Collin, F.; Couturier, M.; Therond, P.; Jore, D.; Gardes-Albert, M.; Bonnefont-Rousselot, D. *Biochimie* **2012**, *94*, 741–747.

[213] Leonard, S. S.; Xia, C.; Jiang, B. H.; Stinefelt, B.; Klandorf, H.; Harris, G. K.; Shi, X. L. *Biochemical and Biophysical Research Communications* **2003**, *309*, 1017–1026.

[214] Fabris, S.; Momo, F.; Ravagnan, G.; Stevanato, R. *Biophysical Chemistry* **2008**, *135*, 76–83.

[215] Armen, R. S.; Uitto, O. D.; Feller Scott, E. *Biophysical journal* **1998**, *75*, 734–744.

[216] Caruso, F.; Tanski, J.; Villegas-Estrada, A.; Rossi, M. *Journal of agricultural and food chemistry* **2004**, *52*, 7279–7285.

[217] Greenwood, A. I.; Tristram-Nagle, S.; Nagle, J. F. *Chemistry and Physics of Lipids* **2006**, *143*, 1 – 10.

[218] Notman, R.; Noro, M.; O'Malley, B.; Anwar, J. *Journal of the American Chemical Society* **2006**, *128*, 13982–13983.

[219] Reviakine, I.; Simon, A.; Brisson, A. *Langmuir* **2000**, *16*, 1473–1477.

[220] Léonard, A.; Escrive, C.; Laguerre, M.; Pebay-Peyroula, E.; Néri, W.; Pott, T.; Katsaras, J.; Dufourc, E. J. *Langmuir* **2001**, *17*, 2019–2030.

[221] Marrink, S. J.; de Vries, A. H.; Harroun, T. A.; Katsaras, J.; Wassall, S. R. *Journal of the American Chemical Society* **2008**, *130*, 10–11.

[222] Wesolowska, O.; Kuzdal, M.; Strancar, J.; Michalak, K. *Biochimica et Biophysica Acta (BBA) - Biomembranes* **2009**, *1788*, 1851–1860.

[223] Gescher, A. J.; Steward, W. P. *Cancer Epidemiology Biomarkers & Prevention* **2003**, *12*, 953–957.